SLAC – 286
UC-34D
(E)

MEASUREMENT OF THE DECAY $\Upsilon(2S) \rightarrow \pi^0\pi^0\Upsilon(1S)$*

David Michael Gelphman

Stanford Linear Accelerator Center
Stanford University
Stanford, California 94305

September 1985

Prepared for the Department of Energy
under contract number DE-AC03-76SF00515

Printed in the United States of America. Available from the National Technical Information Service, U.S. Department of Commerce, 5285 Port Royal Road, Springfield, Virginia 22161. Price: Printed Copy A06, Microfiche A01.

* Ph.D. Dissertation.

ABSTRACT

The hadronic transitions $\Upsilon(2S) \rightarrow \pi^0\pi^0\Upsilon(1S) \rightarrow \gamma\gamma\gamma\gamma l^+l^-$ ($l = \mu$ or e) are investigated using the Crystal Ball detector. The analysis is based on 193 000 $\Upsilon(2S)$ events produced at the DORIS II e^+e^- storage ring from November 1982 to February 1984.

We observe 44 events with a muon pair and 46 events with an electron pair in the final state. The signals in both channels are relatively background free. Assuming lepton universality, we average the results for the two channels and obtain the product branching ratio $B(\Upsilon(2S) \rightarrow \pi^0\pi^0\Upsilon(1S)) \times B_{\ell\ell}(\Upsilon(1S)) = (2.3 \pm 0.3 \pm 0.3) \times 10^{-3}$ where the first error is statistical and the second is systematic. Using the present world average value of $B_{\ell\ell}(\Upsilon(1S))=(2.9 \pm 0.3)\%$ we derive a branching ratio $B(\Upsilon(2S) \rightarrow \pi^0\pi^0\Upsilon(1S))= (8.0 \pm 1.5)\%$ where the statistical and systematic errors have been added in quadrature. This result is compared with previous results for the charged pion transitions $\Upsilon(2S) \rightarrow \pi^+\pi^-\Upsilon(1S)$ and with the expectation from theory.

We have also investigated the invariant mass spectrum $M_{\pi^0\pi^0}$ resulting from these decays and find a peaking toward high masses not accounted for by phase space alone. Fits to the $\pi^0\pi^0$ mass spectrum are in quantitative agreement with previous results for the $\pi^+\pi^-$ transitions.

Angular distributions for the $\pi^0\pi^0$ system and its decay products are presented in reference frames appropriate for analyzing the spin of the $\pi^0\pi^0$ system, even if the initial $\Upsilon(1S)$ and the di–pion system are emitted in a relative S–wave. We find the decay distributions to be consistent with those expected for a spin zero di–pion system emitted in a relative S–wave with the $\Upsilon(1S)$. The results on the angular distributions and the mass spectrum are also compared with the theoretical predictions.

ACKNOWLEDGEMENTS

Many people have contributed greatly to this thesis. The people in the Crystal Ball group, spanning two continents and several countries, made possible this dissertation through their hard work and effort. More locally, the members of the HEPL group: Roland Horisberger, Ian Kirkbride, Roger Lee, Al Osterheld, and John Tompkins provided an enjoyable work environment with plenty of good ideas and good humor over the past 6 years. Most significant in the completion of this work was my advisor Alan Litke, whose many discussions with me resulted in numerous ideas and whose excitement about science always provided a positive push forward.

The support of my family through the years has been essential to the completion of this work. My mother and stepfather, Carole and Bob Spitz, and my grandmother, Rosa Kabaker, always encouraged me to achieve and be successful. By example, my sisters Susan and Janet Gelphman showed me the importance of pursuing one's own ambitions and ideas. My deepest appreciation goes to my father Bernard Gelphman, whose encouraging support during my undergraduate years provided much of the impetus to undertake and complete this dissertation research.

Finally I recognize two very special people who, in their own ways, made enormous contributions to this work. Josephine Zilberkweit's love and friendship made my life in Germany a wonderful experience which still provides happy thoughts and warm feelings. Last to be mentioned, but foremost in my thoughts is Sally Walters, whose support, friendship, love, and understanding made the last years of graduate school survivable and even fun.

Mom, your son is a doctor after all.

Can we actually 'know' the universe? My God, it's hard enough finding your way around Chinatown.

Woody Allen, *Getting Even*

Table of Contents

List of Tables

List of Figures

Chapter 1

Introduction

The discovery[1,2] of the narrow $\Upsilon(1S)$ and $\Upsilon(2S)$ resonances in 1977 indicated the existence of a new fundamental particle in nature, the b or bottom quark. The discovery of these states was followed by the discovery[3–7] of two additional states $\Upsilon(3S)$ and $\Upsilon(4S)$ at higher masses. Figure 1.1 is a plot of the visible cross section for electron–positron annihilation into hadrons as a function of the center–of–mass energy; the data were taken by the CLEO detector operating at the CESR e^+e^- storage ring.[8] This plot shows striking evidence for the existence of these four resonances. The three lower energy resonances have a measured natural width less than that of the CESR center of mass energy resolution of about 4 MeV, while the $\Upsilon(4S)$ has a natural width larger than the machine resolution.

The Υ family of resonances is interpreted as a group of quasi-bound states of a b quark and its antiquark. These $b\bar{b}$ states are analogous to the well studied $c\bar{c}$ states of the charmonium system. The discovery and studies of the J/ψ led to a model[9] which describes these quarkonium states as being composed of a pair of quarks ($q\bar{q}$) bound by the force of the strong interaction. Since the quarks in the heavy $q\bar{q}$ state move slowly, the non-relativistic Schrödinger equation can be used to calculate the energy levels and wave functions of the system. The present theory of strong interactions, Quantum Chromodynamics (QCD), cannot yet derive from first principles a form for the potential which binds the quarks, so models of this potential incorporating the qualitative features of QCD are attempted. One form of

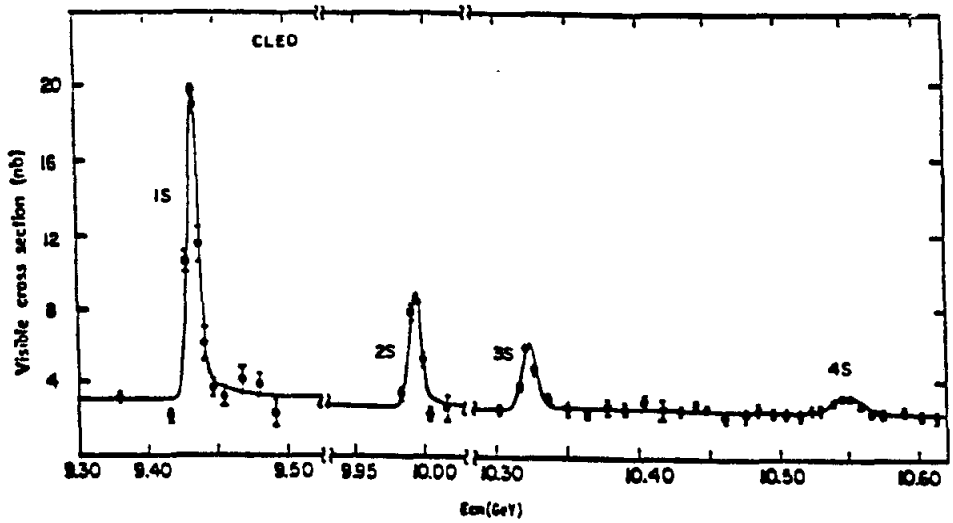

Fig. 1.1 Total visible hadronic cross section as a function of center of mass energy. Data are from the CLEO detector located at the CESR e^+e^-storage ring.

the potential used to describe the forces between the quarks is the so-called Cornell potential:[10]

$$V_0(r) = \frac{-4\alpha_s}{3r} + kr$$

where α_s is the strong coupling constant, r is the radius of the $q\bar{q}$ system and k is a constant. The Coulombic piece $(\frac{1}{r})$ represents one gluon exchange between the quarks and dominates at short distances. At large distances, a term proportional to the separation of the quarks provides confinement. Many other forms of the potential binding the quarks exist in the literature;[11] this form is presented only as an example which gives results typical of those potentials which describe the data.

An important result from this treatment, which has been verified for charmonium and partially for bottomonium, is the prediction of a spectrum of states similar to those of the positronium system but modified because of the differences between the electromagnetic interaction and the strong interaction. Figure 1.2 indicates the

general level spectrum of the Υ system.* Also indicated are some of the hadronic and electromagnetic transitions expected between the different $b\bar{b}$ states.

The existence of both $c\bar{c}$ and $b\bar{b}$ states offers a unique opportunity to test theoretical ideas. The wealth of experimental results for the charmonium system, together with the different theoretical models allow predictions to be made for bottomonium decays and the testing of the theory through experiment. As we will see in the next section, a specific prediction based on scaling laws can be tested by comparing the rates of $\psi' \to \pi\pi\psi$ and $\Upsilon(2S) \to \pi\pi\Upsilon(1S)$.

1.1 Hadronic Transitions between $q\bar{q}$ States

The decay $\Upsilon(2S) \to \pi^+\pi^-\Upsilon(1S)$ was the first observed hadronic transition in the $b\bar{b}$ system.[12,13,14] These low statistics measurements were augmented in 1984 by high statistics inclusive[15,16] and exclusive measurements.[15,16,17] Although many experiments have presented results for $\Upsilon(2S) \to \pi^+\pi^-\Upsilon(1S)$, only one measurement of $\Upsilon(2S) \to \pi^0\pi^0\Upsilon(1S)$ has been performed up to now.[17] A comparison of the charged and neutral $\pi\pi$ transitions is a test of the isospin invariance of this process.

Theory describes the hadronic decay $\Upsilon(2S) \to \pi\pi\Upsilon(1S)$ as a two step process. First the excited quarkonium state radiates gluons as shown in Figure 1.3. The number of gluons must be at least two in order for the $\Upsilon(1S)$ to be a color singlet state. In a second step, the gluons fragment into light hadrons. The details of this process are not understood; however, the properties of the di–pion system are determined by using partial conservation of axial–vector current (PCAC) and current algebra.[18,19]

The gluon emission shown in Figure 1.3 cannot be calculated using perturbative QCD because the energy available to the gluons is small (the $\Upsilon(2S)$,$\Upsilon(1S)$ mass

* There are varying degrees of experimental evidence for states with masses listed in Figure 1.2 and currently no experimental evidence for the other states.

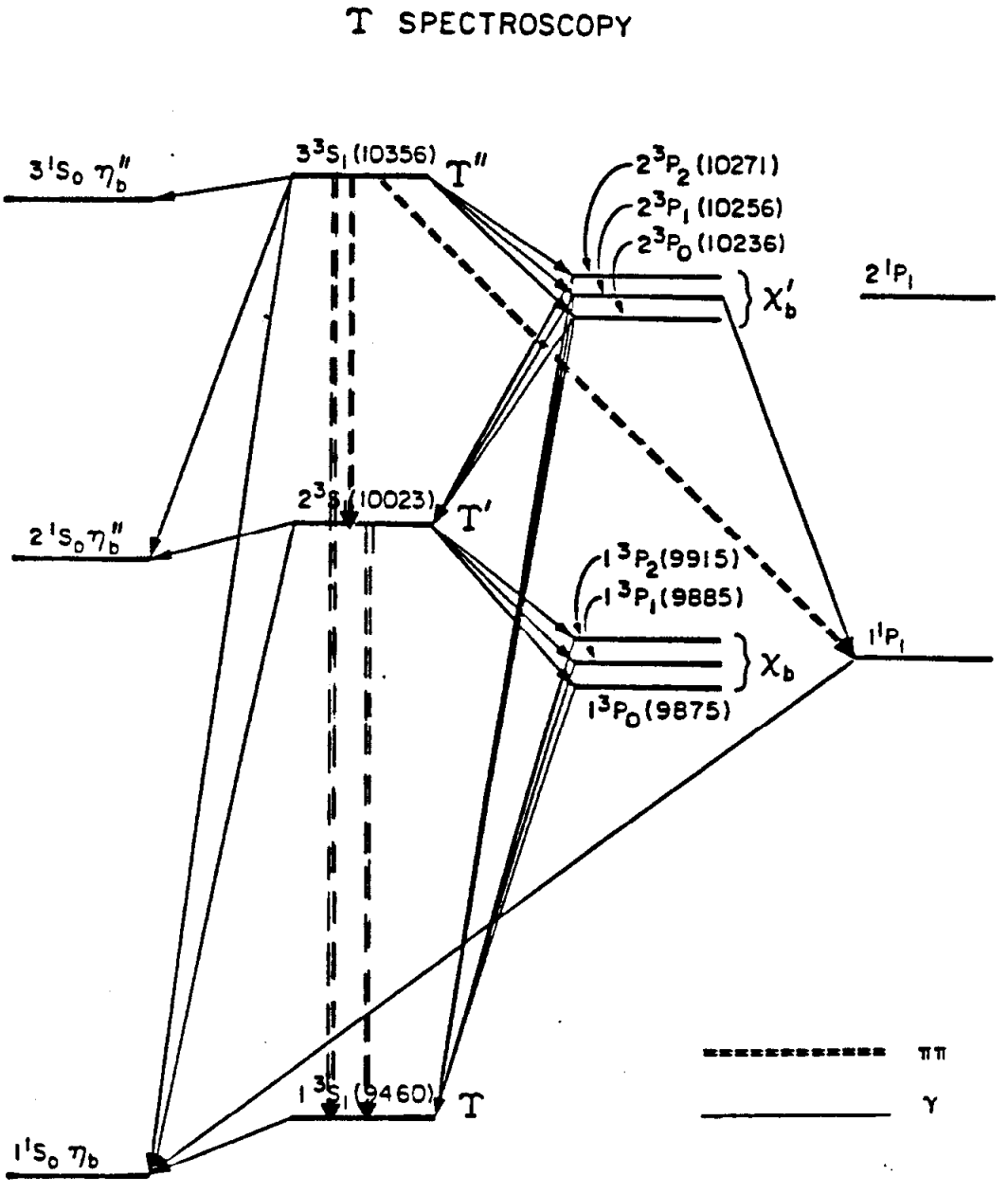

Fig. 1.2 The expected energy level spectrum of $b\bar{b}$ bound states below the $\Upsilon(4S)$. Masses are given for states for which there is some experimental evidence. Also indicated are some of the $\pi\pi$ and γ transitions expected for the $b\bar{b}$ system.

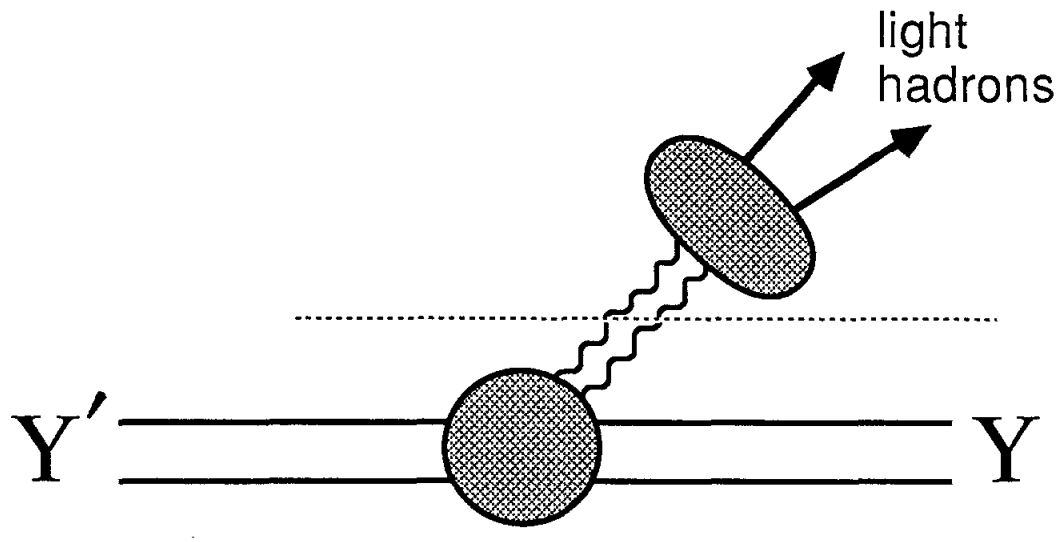

Fig. 1.3 Diagram of the transition $\Upsilon(2S) \rightarrow \pi\pi\Upsilon(1S)$ decay. Here these decays are represented by a two step process: the emission of gluons from heavy quarks (lower half) and the conversion of gluons into light hadrons (upper half).

difference is ~560 MeV). At low Q^2 the strong coupling constant is large and a perturbation series will not converge. Gottfried suggested[20] a multipole expansion analogous to that frequently used in nuclear physics and QED. Since the quarks in the $q\bar{q}$ system are slowly moving and the size of the system is small compared to the wavelength of the gluons, a multipole expansion in the gluonic field can be used.

The assumption that the radiation of the gluons may be described by the multipole expansion provides a scaling law for the rates of these transitions. In order to compare the rates $\psi' \rightarrow \pi\pi\psi$ and $\Upsilon(2S) \rightarrow \pi\pi\Upsilon(1S)$, we note that the $\Upsilon(2S)$,$\Upsilon(1S)$ mass difference is nearly the same as the ψ',ψ mass difference. The theory assumes the splitting to be identical so that the part of the matrix element which depends on the splitting between the energy levels of the two quarkonium states cancels for the two different systems. For gluons, which have spin 1 within the framework of QCD, the lowest order transition is a dipole transition and the multipole expansion

predicts:[19]

$$\frac{\Gamma(\psi' \to \pi\pi\psi)}{\Gamma(\Upsilon(2S) \to \pi\pi\Upsilon(1S))} \simeq \frac{< r^2 >^2_{\psi}}{< r^2 >^2_{\Upsilon}} \simeq 16$$

where r is the radius of the quarkonium system. Here we have used estimates of the size of the $c\bar{c}$ and $b\bar{b}$ system derived from the Cornell potential listed above.[21]

The second part of the theoretical description of these hadronic decays is the fragmentation of the gluons into light hadrons. This is not understood at a fundamental level within the framework of QCD, but Brown and Cahn[18] have shown that PCAC and current algebra can be used to constrain the form of the matrix element. The result is a connection between the angular distributions of the di–pion system (and its decay products) and the mass distribution of the di–pion system. The theory does not make specific predictions for these angular distributions, but does predict that in the absence of any angular correlations, the matrix element is proportional only to $q_{1\mu}q_2^{\mu}$, where q_i^{μ} is the four–momentum of the i^{th} pion. This may be rewritten as:

$$\begin{aligned} q_{1\mu}q_2^{\mu} &\propto (q_1^{\mu} + q_2^{\mu}) \cdot (q_{1\mu} + q_{2\mu}) - q_1^{\mu}q_{1\mu} - q_2^{\mu}q_{2\mu} \\ &\propto M^2_{\pi\pi} - 2m^2_{\pi} \end{aligned}$$

where $M_{\pi\pi}$ is the invariant mass of the di–pion system and m_{π} is the pion mass. The total rate is proportional to the matrix element squared:

$$\frac{d\Gamma}{dM_{\pi\pi}} \propto (\text{phase space}) \cdot (M^2_{\pi\pi} - 2m^2_{\pi})^2$$

We see that in the case where there are no angular correlations, we expect to observe a $\pi\pi$ invariant mass distribution which is more peaked toward high mass than that expected from pure phase space.

This phenomenological approach to the theory resulted from attempts to explain the experimental results obtained in the charmonium system. For $\psi' \to \pi^+\pi^-\psi$ the angular distribution of the $\pi^+\pi^-$ system and its decay products were found to have

isotropic angular distributions.[22] Qualitative measurements of both $\psi' \to \pi^+\pi^-\psi$ and $\psi' \to \pi^0\pi^0\psi$ found the $\pi\pi$ invariant mass to be peaked toward high masses.[22,23]

Experimental results in the $b\bar{b}$ system have indicated similar properties for the decay $\Upsilon(2S) \to \pi^+\pi^-\Upsilon(1S)$. Again the angular distributions of the $\pi^+\pi^-$ system and its decay products were found to be qualitatively consistent with isotropy.[24] Many experiments have observed a peaked invariant mass spectrum[15,16,17] and have obtained a quantitative parameterization of the peaking by fitting the mass distribution to the form: (phase space) $\cdot (M^2_{\pi\pi} - \lambda m^2_\pi)^2$. The result from the CLEO data[16] of $\lambda = 3.2 \pm 0.4$ is 3 standard deviations from the value $\lambda = 2$ expected from the phenomenological theory if the angular distributions of the di–pion system and its decay products are completely isotropic. ARGUS has measured[15] $\lambda = 2.6 \pm 0.5$ for the charged pion transitions; slightly greater than 1 standard deviation from the value $\lambda = 2$. The CUSB data[17] is consistent with the expectation $\lambda = 2$.* The weighted average of these three sets of data disagrees with the expectation $\lambda = 2$ by three standard deviations.

While the available experimental evidence for $\Upsilon(2S) \to \pi\pi\Upsilon(1S)$ shows a peaked mass distribution in qualitative agreement with the theory, measurements of the decay $\Upsilon(3S) \to \pi\pi\Upsilon(1S)$ show a di–pion mass distribution[25,26] which is completely different. Rather than observing a peaked mass distribution, a flat distribution has been seen. No information has been presented in the literature for the angular distributions, nor do results exist for the di–pion mass spectrum resulting from the decays $\Upsilon(3S) \to \pi\pi\Upsilon(2S)$ because of limited statistics.

Only one measurement of $\Upsilon(2S) \to \pi^0\pi^0\Upsilon(1S)$ has been performed up to now.[17] A peaked $\pi^0\pi^0$ mass distribution was observed, but no results were presented which allow a quantitative comparison with the charged pion decays. The

---

* While CUSB did not directly fit λ as discussed above, the result from the parameterization of the mass spectrum they used can be directly interpreted as being consistent with $\lambda = 2$ (see Tables 4.4 and 4.5).

previous measurement for the angular distributions of the $\pi^0\pi^0$ system and its decay products is incomplete. While the angular distributions for the $\pi^0\pi^0$ system were found to be consistent with isotropy, the individual pion angular distributions were analyzed in a frame which does not distinguish between spin states of the $\pi^0\pi^0$ system if the initial decay is isotropic (see Appendix C for details).

The incomplete results for $\Upsilon(2S) \rightarrow \pi^0\pi^0\Upsilon(1S)$ and the unclear interpretation of the comparison between theory and experiment for the $\Upsilon(2S)$ and $\Upsilon(3S)$ decays motivates the study of $\Upsilon(2S) \rightarrow \pi^0\pi^0\Upsilon(1S)$ presented in this thesis. In addition to the decay rate, quantitative results are presented for the $\pi^0\pi^0$ mass spectrum. We also present the angular distributions of the $\pi^0\pi^0$ system and its decay products in reference frames which are appropriate, even if the di–pion system and the $\Upsilon(1S)$ are emitted isotropically.

The results presented in this thesis have been important in the experimental physics program of the Crystal Ball detector at DORIS II. The reaction $\Upsilon(2S) \rightarrow \pi^0\pi^0\Upsilon(1S)$ provided a clean, almost background free exclusive reaction to test the performance of the detector. This data sample allowed improvements to be made in the absolute energy measurements of photons in the 10–450 MeV energy range, as discussed in Appendix A. The question of the energy scale is particularly important for the measurement of the energy levels of the ^3P_J states of bottomonium.[27,28]

1.2 The Crystal Ball at DORIS

The data used in this thesis were collected by the Crystal Ball detector operating at the DORIS II e^+e^- storage ring at the Deutsches Elektronen Synchrotron (DESY) in Hamburg, West Germany (see Chapter 2 for a detailed description of the experimental apparatus). Prior to the data taking at DORIS, the Crystal Ball detector was used to collect data at the SPEAR e^+e^- storage ring at the Stanford Linear Accelerator Center in Stanford, California. At SPEAR, studies were conducted on the charmonium system and the region above charm threshold. Because of the success of the Crystal Ball group at solidifying the experimental picture of

charmonium, the DESY management extended an invitation to undertake a similar program for bottomonium at an upgraded DORIS storage ring. In 1981, the Crystal Ball group and the LENA group joined forces to pursue an experimental physics program at DORIS II.

The detector was removed from the east pit of SPEAR during the Christmas shutdown of 1981. The less delicate components of the detector such as the electronics, computer, and mechanical support structure were sent via cargo ship to Germany. The two hemispheres of hygroscopic NaI(Tℓ) were carefully packaged in special boxes constructed with a styrofoam cushion against shock and which allowed the flow of dry nitrogen to control the humidity. These boxes were trucked to Travis Air Force base near San Francisco, California and flown by a C5–A transport plane to Rhein–Main Air Force base in Frankfurt, West Germany. A caravan of Crystal Ball group members then escorted the truck carrying the hemispheres from Frankfurt to Hamburg where testing and reassembly of the detector commenced. By July of 1982, the detector was installed, fully operational, and ready to take data at DORIS II.

References

1) S. W. Herb et al., *Phys. Rev. Lett.* **39** (1977) 252.

2) W. R. Innes *et al.*, *Phys. Rev. Lett.* **39** (1977) 1240.

3) K. Ueno et al., *Phys. Rev. Lett.* **42** (1979) 486.

4) D. Andrews *et al.*, *Phys. Rev. Lett.* **44** (1980) 1108.

5) T. Böhringer et al., *Phys. Rev. Lett.* **44** (1980) 1111.

6) D. Andrews *et al.*, *Phys. Rev. Lett.* **45** (1980) 219.

7) G. Finocchiaro *et al.*, *Phys. Rev. Lett.* **45** (1980) 222.

8) A. Silverman, Recent Results from CESR, Proc. of the 1981 Int. Symp. on Lepton and Photon Interaction at High Energies, Ed. W. Pfeil (Physikalisches Institut Universität Bonn, Bonn, 1981).

9) T. Appelquist and H. D. Politzer, *Phys. Rev. Lett.* **34** (1975) 43,
A. de Rújula and S. L. Glashow, *Phys. Rev. Lett.* **34** (1975) 46,
C. G. Callan *et al.*, *Phys. Rev. Lett.* **34** (1975) 52.

10) E. Eichten et al., *Phys. Rev. Lett.* **34** (1975) 369.

11) see for example:
C. Quigg and J. L. Rosner, *Phys. Lett.* **71B** (1977) 153,
G. Bhanot and S. Rudaz, *Phys. Lett.* **78B** (1978) 119,
J. L. Richardson, *Phys. Lett.* **82B** (1979) 272,
A. Martin, *Phys Lett.* **93B** (1980) 338.

12) B. Niczyporuk *et al.*, *Phys. Lett.* **100B** (1981) 95.

13) G. Mageras et al., *Phys. Rev. Lett.* **46** (1981) 1115.

14) J. Mueller *et al.*, *Phys. Rev. Lett.* **46** (1981) 1181.

15) H. Albrecht et al., *Phys. Lett.* **134B** (1984) 137.

16) D. Besson *et al.*, *Phys. Rev.* **D30** (1984) 1433.

17) V. Fonseca *et al.*, *Nucl. Phys.* **B242** (1984) 31.

18) L. S. Brown and R. N. Cahn, *Phys. Rev. Lett.* **35** (1975) 1.

19) T. M. Yan, *Phys. Rev.* **D22** (1980) 1652.
Y. P. Kuang and T. M. Yan, *Phys. Rev.* **D24** (1981) 2874.

20) K. Gottfried, *Phys. Rev. Lett.* **40** (1978) 598.

21) E. Eichten *et al.*, *Phys. Rev.* **D21** (1980) 203.

22) G. Abrams, Properties of the New Particles $\psi(3095)$ and $\psi'(3684)$, Proc. of the 1975 Int. Symp. on Lepton and Photon Interaction at High Energies, Ed. W. T. Kirk (Stanford University, Stanford, 1975).

23) M. Oreglia *et al.*, *Phys. Rev. Lett.* **45** (1980) 959.

24) Contributed paper to 1983 Int. Symp. on Lepton and Photon Interaction at High Energies, Cornell University, August 1983.
ARGUS Collaboration, H. Albrecht *et al.*, DESY preprint number ARGUS 83–01.

25) J. Green *et al.*, *Phys. Rev. Lett.* **49** (1982) 617.

26) G. Mageras *et al.*, *Phys. Lett.* **118B** (1982) 453.

27) R. Nernst *et al.*, *Phys. Rev. Lett.* **54** (1985) 2195.

28) W. Walk *et al.*, 'Observation of Two χ_b States in Exclusive Radiative Decays of the $\Upsilon(2S)$', to be submitted for publication in *Physical Review D.*

Chapter 2

Experimental Apparatus

2.1 Doris II

The Doris II e^+e^- storage ring provided the colliding beams necessary for the collection of the data for this thesis. DORIS was originally a double ring storage ring with the two rings crossing at the two detector sites. The maximum center of mass energy in this configuration was 7 GeV. In 1978, the machine was used as a single ring device in order to provide center of mass energies high enough to study the $\Upsilon(1S)$ and $\Upsilon(2S)$ resonances;[1] however, in this mode, the magnets were badly saturated and power consumption was high. In order to remove these difficulties and extend the beam energy so the entire family of Υ resonances could be studied, the machine was rebuilt from November 1981–May 1982. Among the modifications was the removal of one of the original two rings, modification of the dipole magnets, addition of two new RF cavities, and the insertion of two new quadrupole magnets for a mini-β scheme to boost the luminosity.[2] The result of these modifications is DORIS II which has a lower power consumption than the original DORIS and is designed to reach a maximum center of mass energy of 11.2 GeV.

The overall layout of the apparatus necessary to provide the colliding beams is sketched in Figure 2.1. Electrons are produced in Linac I and injected into the DESY synchrotron where they are accelerated up to the beam energy and injected into DORIS II. Positrons are produced in Linac II and injected into PIA, an accumulation

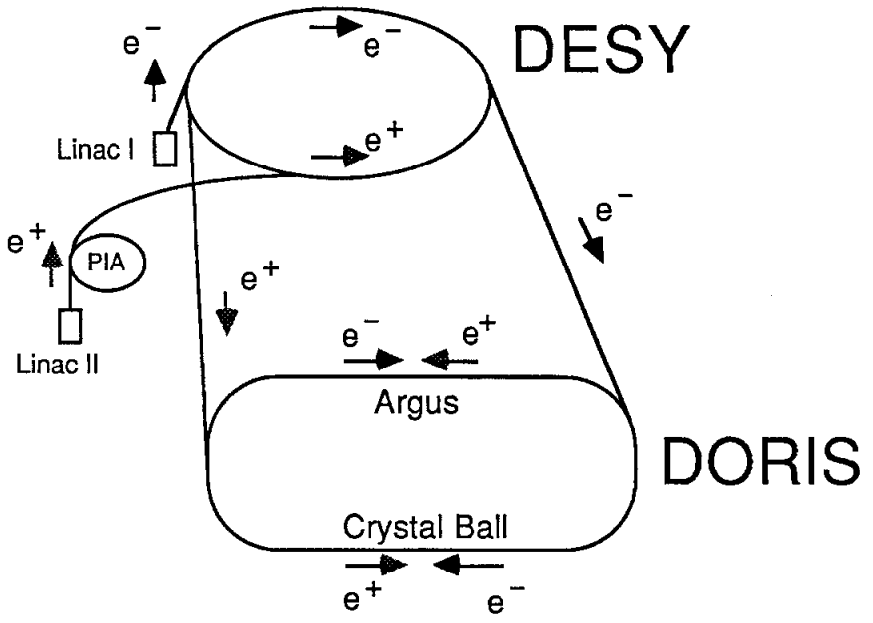

Fig. 2.1 The overall layout of the apparatus necessary for the operation of DORIS II.

ring. Once a sufficient number of positrons are available, they are injected into the DESY synchrotron, accelerated to the beam energy and injected into DORIS II. The electrons and positrons circulate in DORIS in opposite directions and are contained in two separate bunches. Each bunch contains approximately 10^{11} particles with a bunch size of ~1 mm in the plane of the ring, much less than 1 mm in the vertical direction, and a Gaussian longitudinal density distribution with $\sigma_z = 2.5$ cm. The two bunches collide at the two interaction regions: the ARGUS detector is located in the south detector hall and the Crystal Ball detector is located in the north detector hall.

2.2 The Crystal Ball Detector

The Crystal Ball detector is primarily an electromagnetic calorimeter which consists of two major components: two hemispheres of NaI(Tℓ) modules for energy and angular measurements, and tube chambers for charged particle tagging and

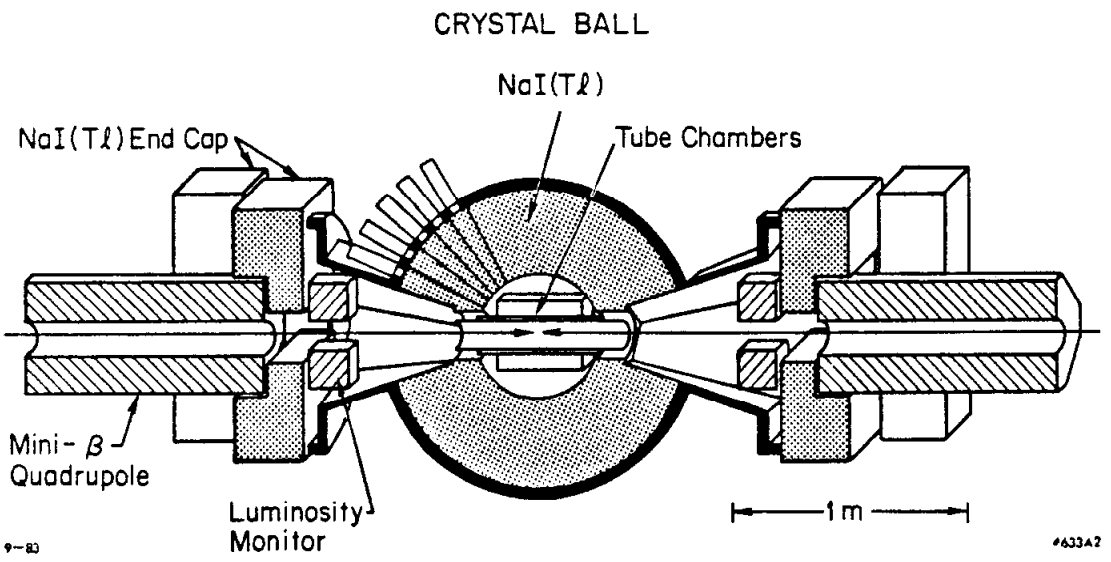

Fig. 2.2 The basic components of the Crystal Ball detector at DORIS II.

directional information. Additional information is provided by NaI(Tℓ) endcaps, a luminosity monitor at small angles to the beamline, and Time of Flight counters.

Figure 2.2 shows the general layout of the detector relative to the beamline. The components pictured in the figure are all located inside of a humidity and temperature controlled dryhouse which is necessary to protect the hygroscopic NaI(Tℓ). Each of the main detector components is described below.

2.2.1 *Main Ball*

The primary component of the Crystal Ball detector is a spherical array of NaI(Tℓ) crystals referred to as the main Ball. The use of sodium iodide provides high detection efficiency and good energy resolution for electromagnetically showering particles. The energy resolution for photons, electrons, and positrons is:

$$\frac{\sigma(E)}{E} = \frac{2.6\%}{E^{\frac{1}{4}}} \qquad \text{(E in GeV)}$$

with an angular resolution of 1-2°, depending on energy. These estimates of the resolution are based on measurements at SPEAR.[3,4]

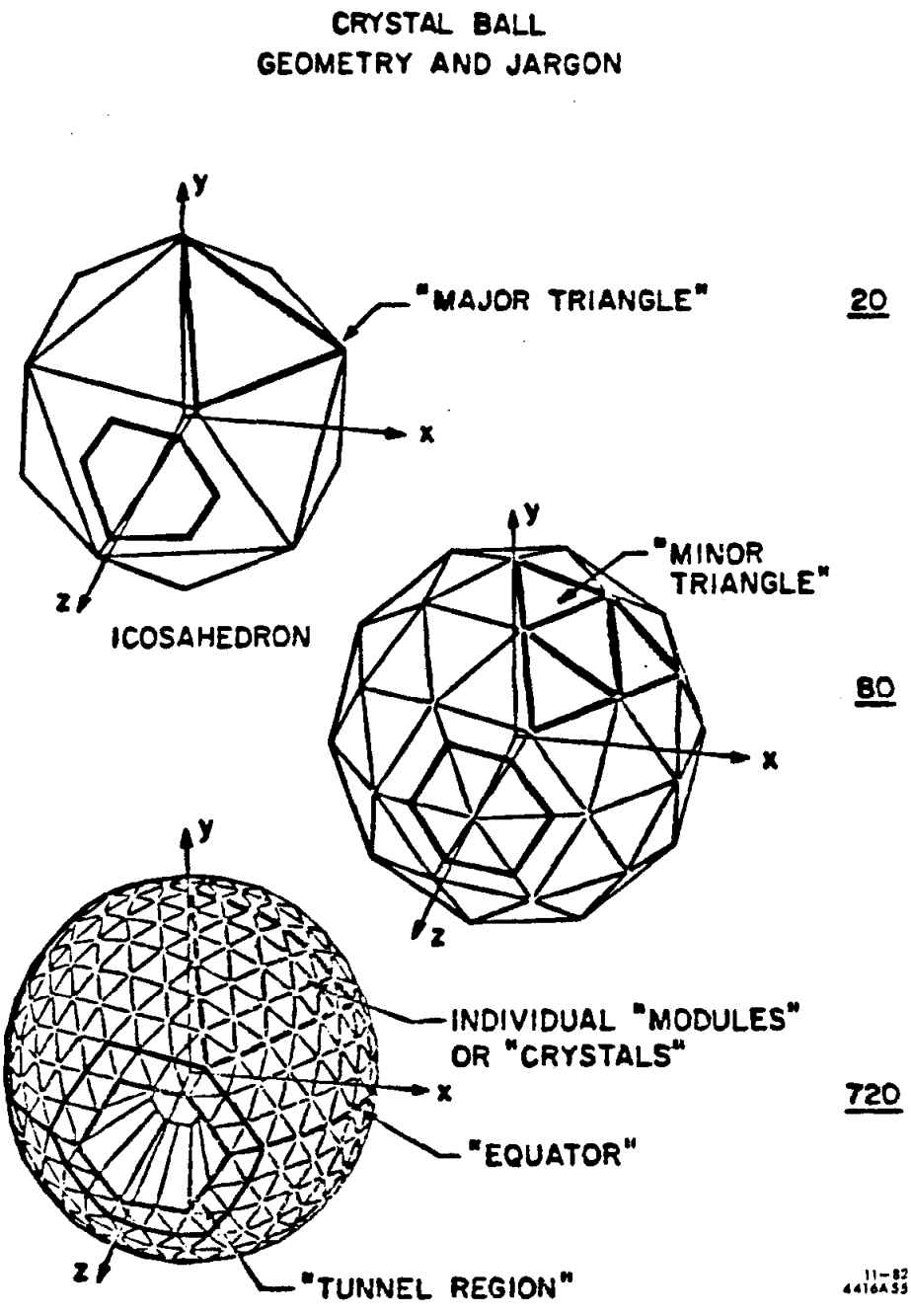

Fig. 2.3 The geometry and jargon of the Crystal Ball detector. There are 9 individual modules which make up a minor triangle. Four minor triangles make up a major triangle which corresponds to one of the twenty sides of an icosohedron.

The geometry and nomenclature of the main detector is represented in Figure 2.3. The basic underlying geometry of the main sodium iodide array is an icosehedron, a 20-sided solid. Each of the 20 triangular surfaces, called 'major triangles', is divided into four smaller triangles called 'minor triangles'. Each minor triangle is further subdivided into 9 individual modules. The individual modules point to the center of the solid which is the region where the annihilations of the electrons and positrons occur. The above divisions imply that the main array would be comprised of 720 modules; however, the beampipe carrying the electrons and positrons requires a hole through the detector and reduces the number of modules in the main Ball to 672. The solid angle covered by the main Ball is therefore reduced to 93% of 4π steradians.

Each of the two hemispheres consists of 336 optically isolated modules of NaI(Tℓ). A schematic view of an individual module is shown in Figure 2.4. The front of each crystal is about 25 cm from the interaction region and the crystal itself is 16 inches long which corresponds to 15.7 radiation lengths of NaI(Tℓ). Each crystal is wrapped in paper and aluminized mylar foil for optical isolation. At the back of each module is a window viewed by a photomultiplier tube which converts the light output into an electronic signal. The modules in each hemisphere are stacked in a steel can for support and each hemisphere is mechanically isolated. The hemispheres themselves are attached to a hydraulic mechanism which allows them to be separated about 2 meters apart. This separation allows for access to the charged tracking chambers and the beampipe and also provides protection for the NaI(Tℓ) crystals during periods of high radiation exposure such as during injection and machine physics. During data taking the two hemispheres are closed so that the gap between them is about 3.5 to 8.0 mm, with the larger value at the outer radius of the Ball.

Another view of the Crystal Ball geometry is the so called 'flats', an event display shown in Figure 2.5. This is essentially a Mercator projection of the main Ball onto a flat page. Individual modules are indicated by each small triangle.

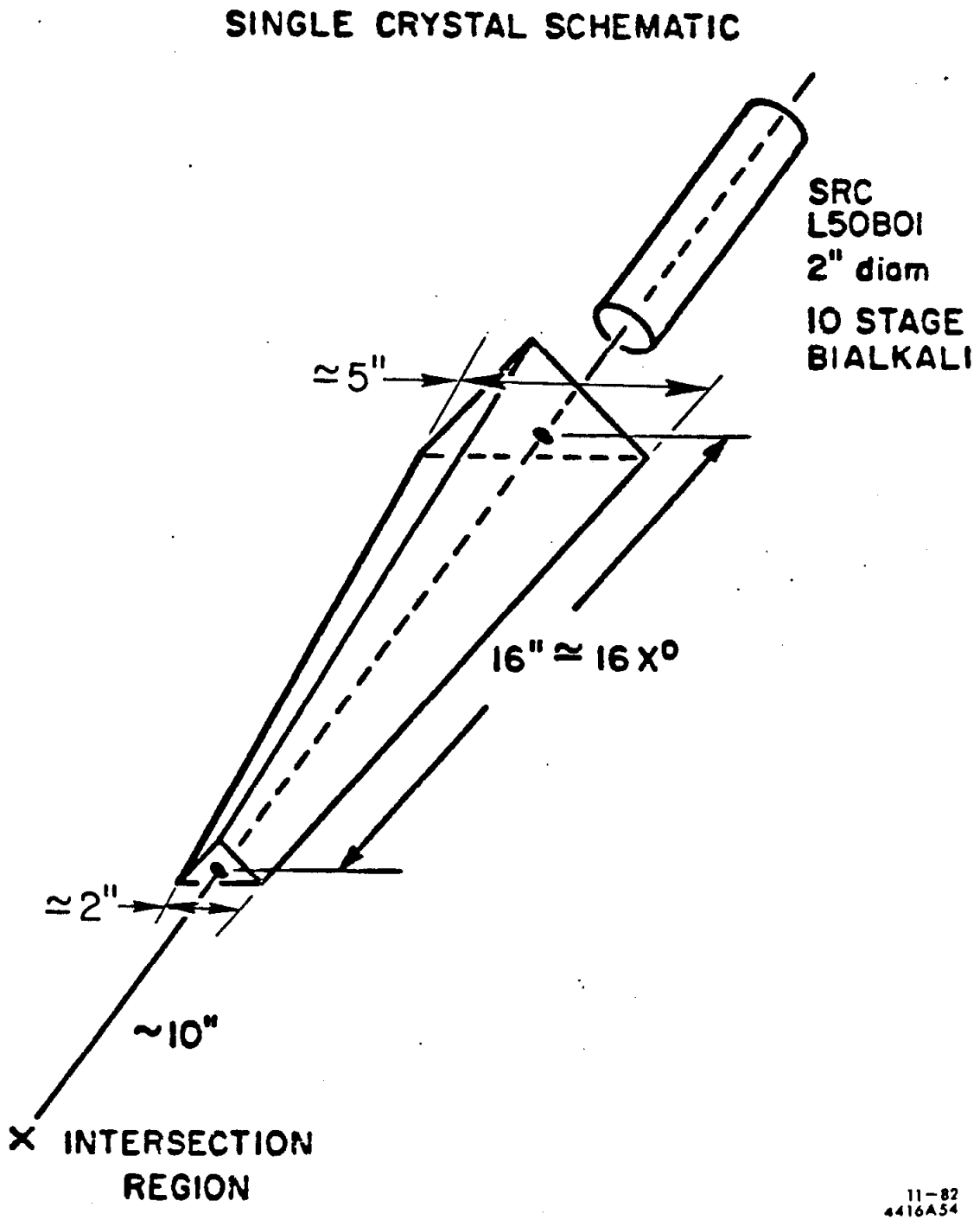

Fig. 2.4 The dimensions of a single crystal.

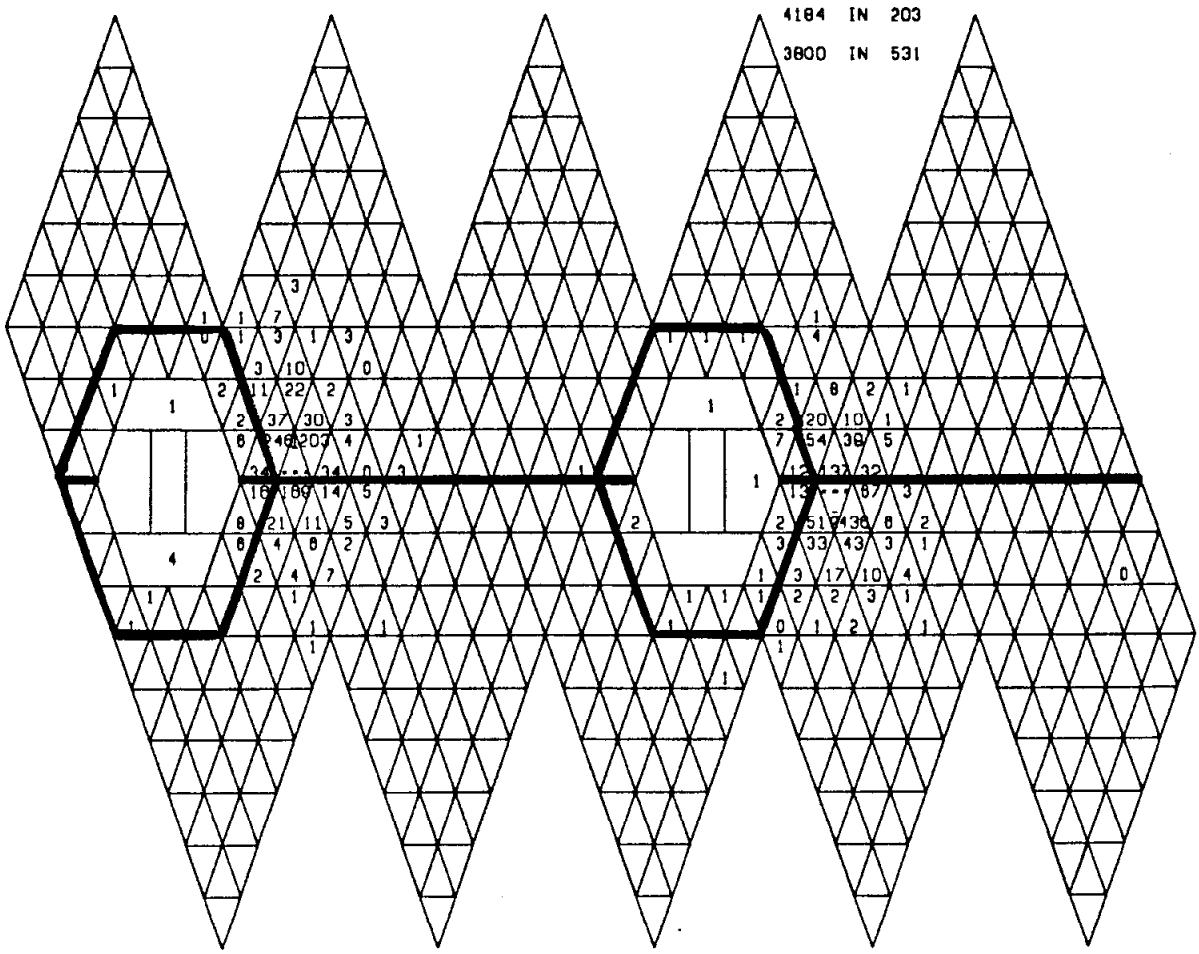

Fig. 2.5 A Mercator-like projection of an event in the Crystal Ball. Each small triangle represents an individual NaI(Tℓ) module. The numbers in each triangle represent the energy (in MeV) contained in that module. The tunnel region and the equator gap are indicated by the heavy lines.

Crystals containing $\frac{1}{2}$ MeV or more have the amount of energy (in MeV) printed within the borders of the module. The beampipe entry/exit holes are indicated as the large gaps in the main array of small triangles. The 'equator' where the two hemispheres come together is indicated as are the 'tunnel modules', the ring of modules surrounding the entry/exit holes for the beampipe.

The two hemispheres comprising the main Ball are unchanged from SPEAR. The only change incorporated in the main array for the DORIS environment was the adjustment of the phototube gains to $\frac{1}{2}$ the value used at SPEAR. This was done to match the dynamic range of the detector to the larger energies at DORIS II. For more detailed information about the main Ball see the SPEAR references.[5]

2.2.2 *Endcaps*

NaI(Tℓ) endcaps are used to provide solid angle coverage in the region near where the beampipe passes through the detector. The use of endcaps extends the solid angle coverage to 98% of 4π. Twenty hexagonal crystals are mounted in each tunnel region as shown in Figure 2.2. The endcaps at DORIS are less complete than those employed with the Crystal Ball at SPEAR because of the space limitations forced by the mini-β quadrupoles. Because of these limitations, the endcaps offer only 3–9 radiation lengths of sodium iodide (depending on position) and no precision energy measurements can be performed. The endcaps are instead used to veto events which contain large amounts of energy outside the region covered by the main Ball.

2.2.3 *Tube Chambers*

The information for the tagging and tracking of charged particles is provided by 3 double layers of proportional tube chambers with charge division readout. The geometry of the chambers is shown in Figure 2.6. The solid angle coverage from the innermost to outermost chamber is 98%, 96%, and 75% respectively. Each of the 3 chambers consists of two layers of aluminum tubes with a wall thickness of

.08 mm. These tubes are mounted on a stiff backing for support. At each end of the chambers are amplifiers to boost the signal to an acceptable level.

During the $\Upsilon(2S)$ data taking, there were two different chamber configurations used. The first set was operated at DORIS II from July 1982–June 1983 during the collection of about $\frac{1}{4}$ of the $\Upsilon(2S)$ data. These chambers had been used for data taking with the Crystal Ball at SPEAR during the Fall of 1981 and are detailed elsewhere.[6] In this configuration there were 80 tubes in each of the first 4 layers and 160 in each layer of the outer chamber. The chambers were operated with 'magic gas' (20% Isobutane, 4% Methylal, .25% Freon 13B1, and Argon) which results in a large output pulse from the chambers which is essentially independent of the primary ionization caused by the passing charged particles.

During this phase of data taking the performance of the first two chambers was quite erratic as can be seen in Figure 2.7a. This is a plot of the .OR. efficiency of the two layers of chamber 1. The data for chamber 2 looks similar to this plot. Figure 2.7b is the data for chamber 3. Each point on the plot represents a data taking run from January 1983 to March 1984. Clearly the performance of chamber 1 was degrading during the time from the beginning of 1983 until the replacement of the chambers in June of 1983, indicated by the arrow on Figure 2.7a. The major problem was found to be an organic growth on the wires resulting from a breakdown of the magic gas due to the radiation exposure from the beams. The growth on the anode wires limited the operating voltage of the chambers and resulted in a lower efficiency. The third chamber suffered less because the larger chamber radius resulted in a lower radiation exposure.

In June of 1983 the first two chambers were replaced by a second set with thicker walls for a sturdier construction. The number of tubes was reduced to 64 for each of the two layers of chamber 1 and 76 tubes for each of the two layers in chamber 2. The operating gas for the first two chambers was changed to an Argon-CO_2 mixture (20% CO_2, 1% Methane, and Argon) which does not suffer from radiation effects. As can be seen in the data to the right of the arrow in Figure 2.7a, the performance

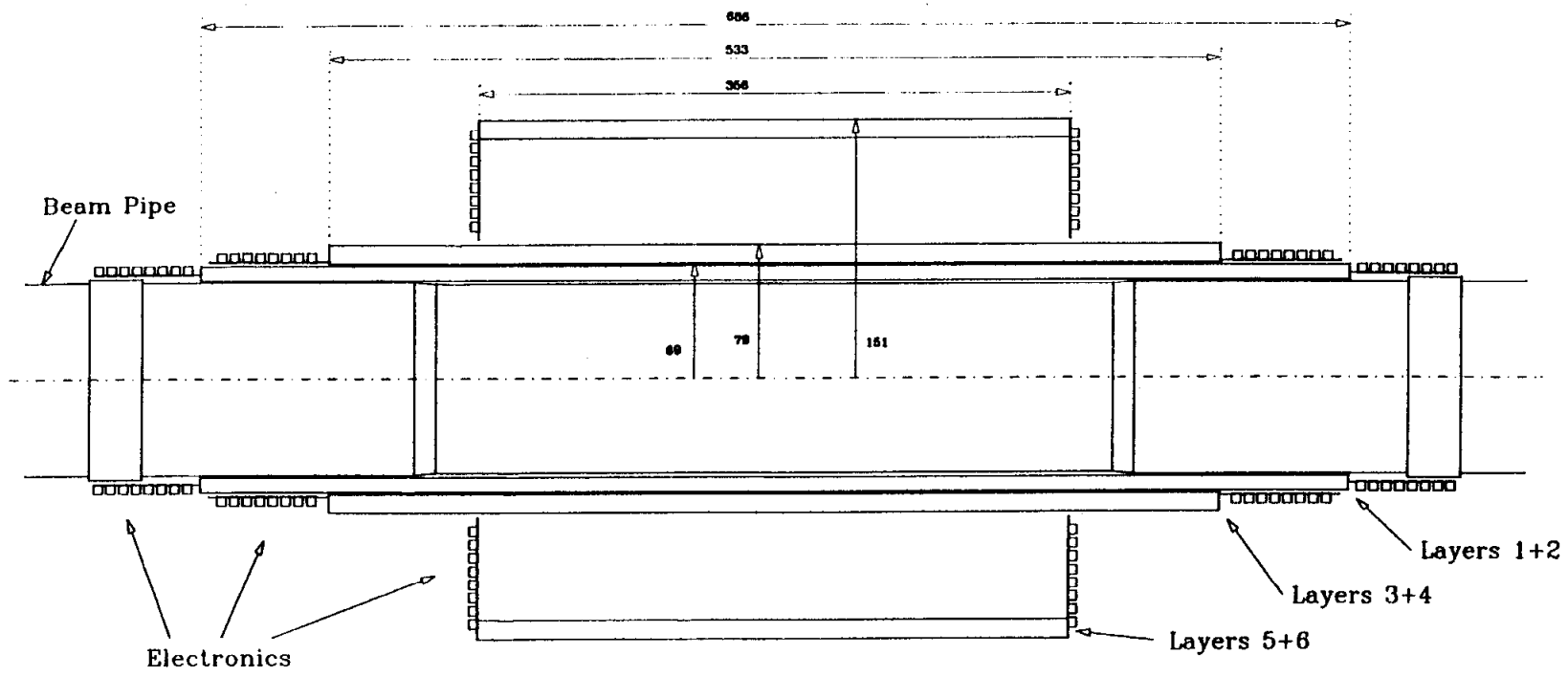

Fig. 2.6 The Crystal Ball tube chamber system. All measurements are in millimeters.

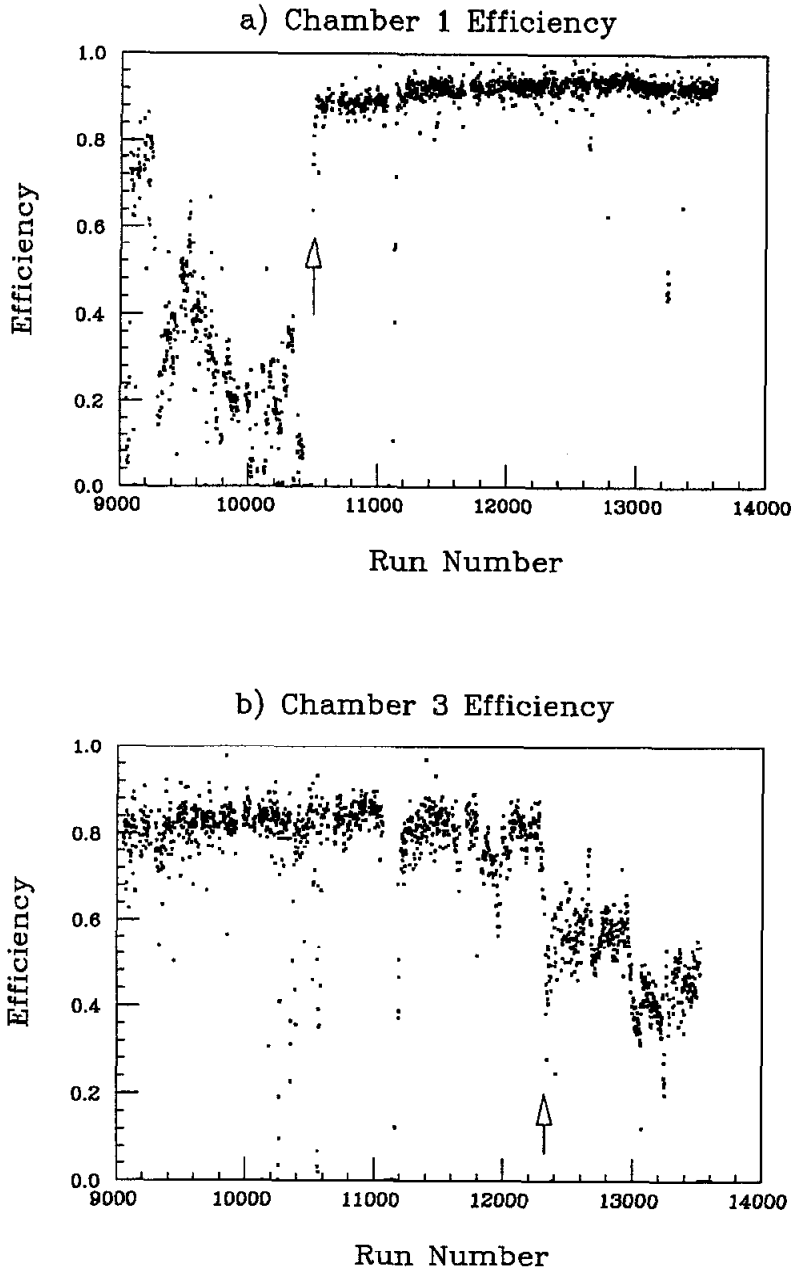

Fig. 2.7 .OR. Chamber efficiency versus time. Each point represents a run from January 1983 to March 1984. The arrow in a) indicates the time when chambers 1 and 2 were replaced. The arrow in b) indicates the beginning of 1984 and the onset of problems with chamber 3. The data for chamber 2 are similar to that of chamber 1.

of chamber 1 was dramatically improved and stabilized. Similar improvement was realized in chamber 2.

The best $\Upsilon(2S)$ data taking in terms of chamber performance occurred from June 1983 to December 1983. By January of 1984 the performance of chamber 3 was affected by the radiation. The arrow in Figure 2.7b indicates the start of the January 1984 run where ~40% of the $\Upsilon(2S)$ data were taken.

Because of the large variation of chamber performance over the year of $\Upsilon(2S)$ data taking, the chamber information has not been used in the analysis discussed in this thesis. The constraints in the $\pi^0\pi^0 l^+ l^-$ channel allow a study to be performed with little background contribution. This approach avoids the lower event detection efficiency and larger systematic uncertainties which would result from the use of the chamber information.

2.2.4 *Electronics and Trigger System*

The signal information from the photomultiplier tubes on each crystal is processed two different ways. The raw analog signal is used as input to the trigger system. In addition, the signal is digitized and recorded as part of the event for further data analysis. The output from the tube chambers is also digitized and recorded as part of the event.

Analog Signal Processing

The group of nine crystals forming a minor triangle defines a useful geometric unit. The phototube signals from the crystals in each minor triangle are summed to form an analog sum of nine (Σ_9). In the triggers we discuss here, the so called Tower triggers,[7] this is the lowest level of trigger logic. The 80 Σ_9 signals (one per minor triangle) are plugged into discriminators with thresholds of about 85 MeV. The four Σ_9 signals of each major triangle are also summed to form 20 sums of 36 crystals each (one per major triangle) which are used as input to discriminators with thresholds of about 150 MeV. The Σ_9 signals are also summed to form a total

energy sum. This sum does not include the endcap crystals or the tunnel modules which are the most susceptible to spurious beam related energy. These three types of energy sums: E_9, E_{36}, and E_{tot} form the basis of the triggers used in this study.

Triggers

Three triggers were used to capture the events studied in this analysis. The simplest trigger is the total energy trigger. This trigger requirement is met when the E_{tot} sum discussed above exceeds 1.7 GeV. This trigger is essentially 100% efficient for $\pi^0\pi^0e^+e^-$ events fully contained in the fiducial region of the detector.

Two additional triggers are employed for finding $\pi^0\pi^0\mu^+\mu^-$ events and also provide redundancy for the $\pi^0\pi^0e^+e^-$ events. The μ–pair trigger fires on events with at least 2 approximately back-to-back particles with the total event energy exceeding 220 MeV. Additionally, for each tunnel region (one at $+z$, one at $-z$), the sum of the energy in the tunnel modules is required to be less than 40 MeV. For the approximately back-to-back requirement to be met, a minor triangle A and either a) the minor triangle B 180° opposite to A must each have $\geq$85 MeV or b) one of the 3 minor triangles neighboring B must have $\geq$85 MeV. The trigger does not fire if the two minor triangles are in the same hemisphere or if either of the minor triangles includes tunnel modules.

The second trigger for $\pi^0\pi^0\mu^+\mu^-$ events is the so called 'topology' trigger. This trigger is based on the fact that the Crystal Ball can be divided 10 different ways into 20 approximate hemispheres. The topology trigger requires each of these 20 hemispheres to have $\geq$150 MeV and a total energy exceeding 770 MeV. The .OR. efficiency of the μ–pair trigger and the topology trigger is greater than 98% for $\pi^0\pi^0\mu^+\mu^-$ events fully contained in the fiducial region of the detector.

An additional special trigger, the so called DORIS Bunch Marker (DBM) trigger, is used to study beam related background. This trigger fires once every 10^7 beam crossings and coincides in time with the beam crossing. Since the beams circulate around DORIS approximately 10^6 times per second, the DBM trigger rate is

about 0.1 Hertz. This trigger is especially important for understanding the spurious energy present in the interaction region during random beam crossings since it is the only trigger which has no energy bias.

Digital Signal Processing

The analog signal from each crystal phototube is attached to 2 RC circuits which integrate the incoming charge on a capacitor. The two circuits have differing dynamic ranges so that precise measurements can be made at all energies. The 'low energy channel' covers the range from 0–330 MeV, above which the signal is above the range which can be digitized. The 'high energy channel' attenuates the signal by a factor of $\simeq$20 and covers the range 0–6.5 GeV. Each channel operates as follows: the charge on the capacitor builds up as the signal from the phototube arrives. If the trigger logic fires, then the capacitor is isolated and the voltage on each capacitor for all crystal channels is sequentially digitized by a 13 bit analog-to-digital converter and stored to a temporary memory buffer. Once all the signals have been digitized, the buffer is read out by a PDP 11/55 computer which controls the online data acquisition. If there is no trigger, then the capacitor is not isolated and the charge on the capacitor decays to a negligible level before the next beam crossing. The signals for each end of the tube chamber are processed in the same manner as the crystal signals but with only one RC circuit per tube end.

2.2.5 *Luminosity Monitor*

Measurements of the integrated luminosity collected by the experiment are provided by measuring the well known Bhabha scattering cross section for $e^+e^- \rightarrow e^+e^-$ in two ways. A small angle monitoring system, sketched in Figure 2.8, is located at about 8° from the beampipe and has a high counting rate because of the strong peaking of the Bhabha cross section toward the beamline. This monitor differs significantly from the one used at SPEAR in several ways. The most important difference is that, due to space considerations, the DORIS monitor is located inside the main Ball tunnel cutout and therefore the beampipe and tube chamber

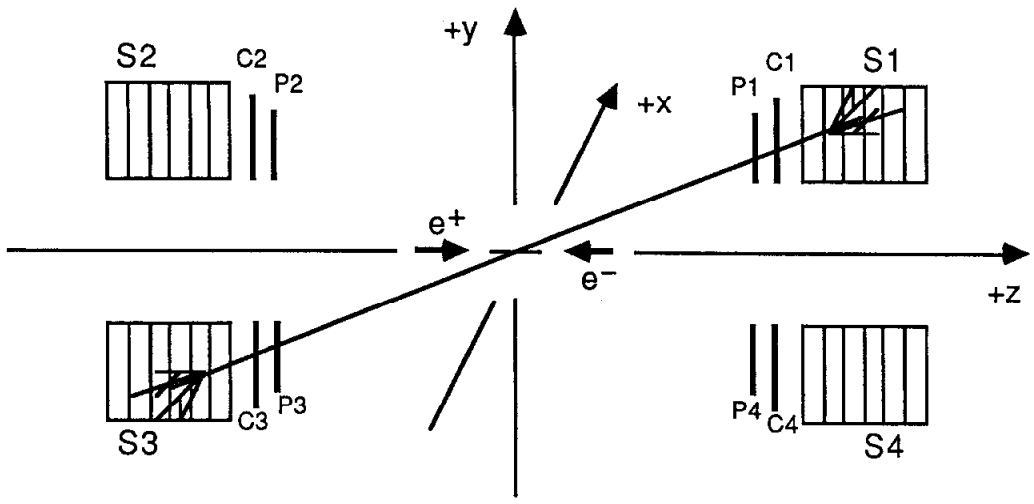

Fig. 2.8 Layout of the Crystal Ball luminosity monitor at DORIS. The +z direction is the positron beam direction, the x–z plane is the plane of the ring with +x pointing toward the center of the ring.

cables provide an uncertainty in the measurement caused by the dead material. The P and C counters indicated in the figure are scintillation counters which are used to define the solid angle acceptance of the system. The S counters are made of a lead/scintillator sandwich[8] and are used to measure the energy of the scattered electrons and positrons. The integrated luminosity is determined by dividing the number of Bhabha events detected in the counters by the visible Bhabha cross section, i.e. the Bhabha cross section integrated over the small angle detector.

A second method of determining the luminosity is provided by measuring Bhabha scattering with the main Ball itself.[9] Since the main detector is at larger angles to the beamline, this measurement is more time consuming and is not appropriate for beam optimization and quick detector diagnostics. The large angle method is used for the final luminosity measurements quoted in this thesis and a comparative check with the luminosity determined from the small angle counters is made on a run by run basis.[10]

2.2.6 *Time of Flight System*

Added to the Crystal Ball detector for the DORIS running was a system used for providing information for time of flight measurements. This system consists of 94 plastic scintillation counters, stacked outside the dryhouse containing the NaI(Tℓ) hemispheres, which cover the upper 50% of the 4π solid angle. Each counter has a phototube at each end which is used as input for both a time-to-digital converter and an analog-to-digital converter. This information provides both position and timing information so that hits in the counters can be correlated with particles detected in the upper hemisphere of the main Ball and the time of each track entering the counters can be determined. The system is intended for the rejection of cosmic ray events and is not used in this analysis. A more detailed description of the hardware for the Time of Flight system may be found in the references.[11]

2.2.7 *Additional Apparatus*

Light Flasher System

A light flasher system is available for monitoring the crystal channels during data acquisition and for monitoring the linearity of the electronics offline. The flasher system has two methods of pulsing the electronics.[12] Each phototube has a LED installed in the base which can be pulsed in groups of nine crystals (minor triangles). In addition, two XENON flash tubes, one for each hemisphere, are connected via fiber optics to each phototube. In this mode of operation, each XENON flash tube is pulsed independently, and the signal is received by all phototubes in the corresponding hemisphere. During normal data taking, the hemispheres are alternately flashed every ten seconds.

Crystal Timing Information

Event timing information over the full solid angle of the Crystal Ball is provided by measuring the time dependence of the energy deposition in the Ball. The

analog energy sum (Σ_{36}) for each major triangle is the input for a constant fraction discriminator. The pulse of each discriminator is used to stop a time-to-digital converter which is started on the beam crossing.[11] The event time is calculated from an energy weighted sum of the major triangle signal times and is calibrated so that a particle travelling at the speed of light registers an event time of 0. The resolution of the event timing distribution is about 400-800 picoseconds depending on the amount of energy in the detector, with the lower value corresponding to Bhabha events and the higher time corresponding to $e^+e^- \rightarrow \mu^+\mu^-$ events.

References

1) see for example:
Ch. Berger *et al.*, *Phys. Lett.* **76B** (1978) 243,
C. W. Darden *et al.*, *Phys. Lett.* **76B** (1978) 246,
J. K. Bienlein *et al.*, *Phys. Lett.* **78B** (1978) 360,
C. W. Darden *et al.*, *Phys. Lett.* **78B** (1978) 364,
Ch. Berger *et al.*, *Z. Phys.* **C1** (1979) 343,
H. Albrecht *et al.*, *Phys. Lett.* **93B** (1980) 500,
B. Niczyporuk *et al.*, *Phys. Rev. Lett.* **46** (1981) 92,
B. Niczyporuk *et al.*, *Phys. Lett.* **100B** (1981) 95.

2) K. Wille, DESY report number DESY-81-047 August, 1981.

3) J. Gaiser, Ph. D. thesis, Stanford University, 1982, and SLAC Report 255 (unpublished).

4) R. Lee, Ph. D. thesis, Stanford University, 1985, and SLAC Report 282 (unpublished).

5) M. Oreglia, Ph. D. thesis, Stanford University, 1980, and SLAC Report 236 (unpublished).

6) R. Horisberger, Ph. D. thesis, Stanford University, 1984, and SLAC Report 266 (unpublished).

7) G. Godfrey, Crystal Ball note 131, 1978.

8) D. Andreasyan, J. Irion, and A. Weinstein, Crystal Ball note 317, 1982.

9) G Folger, J. Irion, and B. Lockman, Crystal Ball note 600, 1984.

10) R. Nernst, Ph. D. thesis, Universität Hamburg, 1985 (unpublished).

11) D. Prindle, Ph. D. thesis, Carnegie–Mellon University, 1985 (unpublished).

12) F. Porter, Crystal Ball note 22, 1983.

Chapter 3

Data Acquisition and Preliminary Data Analysis

3.1 Doris Operation

The rebuilding of Doris into Doris II produced a new storage ring in terms of operating the machine efficiently. The first running of Doris II on the $\Upsilon(2S)$ resonance in November of 1982 resulted in high backgrounds and an integrated luminosity of about 250 nb^{-1} per day during Doris up time. The peak beam currents were about 22 milliamperes per beam. As in a new storage ring, the process of optimizing luminosity and minimizing backgrounds was accomplished slowly. Figure 3.1 indicates the luminosity per week from July 1982 to March 1984. The best running on the $\Upsilon(2S)$ came during early 1984 with filled beams of 45-50 milliamperes per beam; integrated luminosities of 1 pb^{-1} per day were common. During the first 6 weeks of running in 1984, about 40% of the entire $\Upsilon(2S)$ data set was accumulated.

The operation of Doris II is broken up into colliding beam running and single beam running. Colliding beams for high energy physics are provided during approximately $\frac{2}{3}$ of the 8-10 months of Doris II operation per year. The single beam running is dedicated beamtime for HASYLAB, a synchrotron radiation laboratory. During this HASYLAB running, large amounts of radiation bombard the Crystal Ball detector. Since large doses of radiation may ruin the optical properties of NaI(Tℓ), the Crystal Ball is shielded with lead during this running. Radiation impinging on the detector is measured instantaneously by scintillation counters. Thermoluminescent

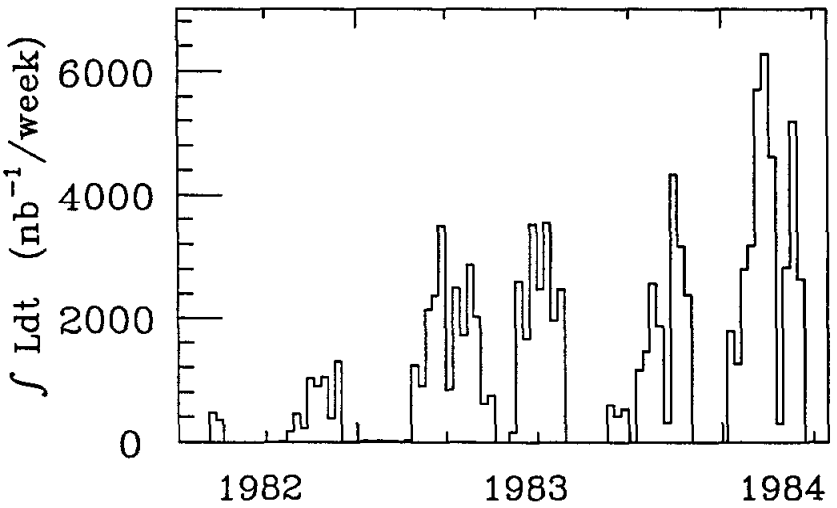

Fig. 3.1 Doris II luminosity from July 1982 to March 1984. Each bin represents one calender week.

dosimeters (TLD's) are used for accurate measurements of integrated radiation over time.

Operation for high energy physics consists of sequences of filling the machine with electrons and positrons and allowing the beams to collide until the data rate subsides. The machine is then refilled and the cycle continues. The total filling time for both electrons and positrons is about 2 minutes during normal operation. During the filling of the storage ring, increased radiation levels in the area surrounding the beampipe occur, therefore; immediately prior to filling the storage ring, the Crystal Ball hemispheres are separated into an open position by remote control. This opening moves each hemisphere about 1 meter away from the beamline and reduces the radiation levels impinging on the detector to an acceptable level.

Beam lifetimes vary from 1-3 hours depending on the amount of stored current at the beginning of a run and the vacuum in the beampipe. The best vacuum achieved in Doris II is about 10^{-9} torr. After shutdowns of the machine, the vacuum is about an order of magnitude worse and therefore the running conditions at the beginning of a data taking cycle are the poorest. A typical run during good beam conditions

has about 1-2 hours between fills.

Synchrotron radiation is produced as the bunches rotate in the storage ring and has two important consequences. Firstly, the quantum fluctuations in the amount of radiation emitted causes a Gaussian spread in the center of mass energy with $\sigma_{E_{cm}} \simeq 8$ MeV at the $\Upsilon(2S)$ resonance.[1] Secondly, the electron and positron spins become polarized as they circulate.[2] At the $\Upsilon(2S)$ energy, there are no de-polarizing resonances and the beams reach 70-80% polarization in about 3-4 minutes. The polarization of the beams affects the angular distributions of the final state and its effects must be taken into account (see Chapter 4).

3.2 Crystal Ball Operation

The process of providing data for physics analysis consists of several parts:

- the accumulation of the data through the hardware onto magnetic tape,
- data quality checks to verify proper operation of the detector,
- calibration of the apparatus, and
- production of the data to turn raw pulse height information into meaningful energies and particle tracks.

Because of the history of the experiment and its connection with SLAC, the calibration and production of the data in this thesis were done at SLAC. The great distance between the data taking site and the production site meant a time lag between data taking and production. This made data quality checks at the experimental site even more imperative than would normally be the case. Figure 3.2 summarizes the steps of acquiring the data, checking the data quality, and bringing the data to SLAC for calibration and production.

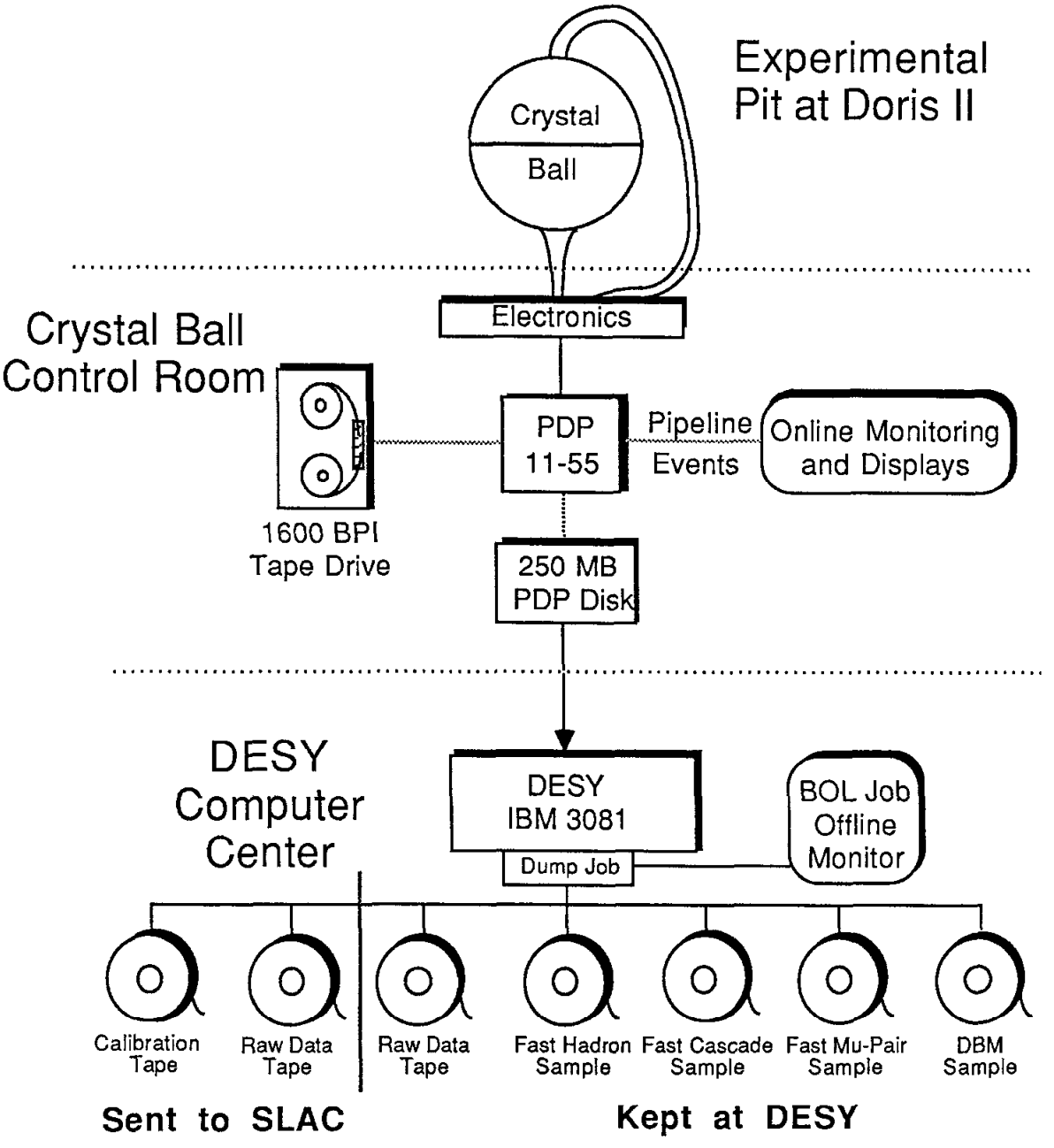

Fig. 3.2 An overview of the data flow from the experimental apparatus to SLAC for the production analysis.

3.2.1 *Data to Tape*

Data rates varied from 3-6 Hertz depending on the beam conditions and trigger settings. When an event is triggered, the analog signals are digitized and read out, creating an event record. For purposes of saving data storage space, data are compressed so that only channels whose signal exceeds a threshold above pedestal are recorded. Every 128^{th} event is fully written out in order to provide pedestal measurements. The data events are temporarily written to a 250 megabyte disk in the experimental control room and then shipped via a link to the DESY IBM 3081 where it is stored on disk. The disk local to the experiment provides a buffer of data storage during any DESY IBM outages. When enough data has been accumulated on the disk at the IBM, the raw data events are written out to a 6250 BPI tape. Two permanent copies of this tape are made; one for storage at DESY and one for shipment to SLAC. Once the copies are verified, the original tape is recycled for new data storage.

3.2.2 *Online Monitoring*

During data taking, a fraction of the data events, the so called 'pipeline events', are selected and sent through an analysis chain at the PDP on a lower priority basis. This analysis does not inhibit the collection and recording of the data. The processing of events at the online computer allows some direct monitoring of the data quality. Hadronic events and Bhabha events* can be selected from these pipeline events.

The Bhabha events are used to monitor the efficiency of the tube chambers for each run. While the normalization of such an efficiency is not well determined, the run to run changes can be used as a quick monitor of the chambers. Other

---

* Throughout, we loosely use the term 'Bhabha events' to refer to both $e^+e^- \rightarrow e^+e^-$ and $e^+e^- \rightarrow \gamma\gamma$ events since the central tracking chambers are not used in the selection of these events.

information, such as the pulse height distributions for each layer, are available as diagnostic tools.

The hadronic events can be used to provide a rough online measurement of R, the ratio of the hadronic cross section to the μ pair cross section.[3] This measurement is sensitive to hardware problems since it is calculated from both the number of hadrons and the luminosity as measured from large angle Bhabha scattering. The R_{online} measurement also provides information as to the beam energy. When sitting on a resonance such as the $\Upsilon(2S)$, changes in R_{online} outside of statistics (which are not attributed to hardware failures) indicate a shifting beam energy.

Pipeline events can also be displayed on a viewing screen to provide visual feedback. The 'flats' image of an event can also give information regarding some types of detector malfunctions. Events triggered by the Xenon flash tube have large amounts of light deposited into the phototube. Because these events give information about the activity of the electronics of each crystal channel, at the beginning of each run a check is made of a flasher event to verify that each crystal output channel is functioning properly. At the conclusion of each run a summary of diagnostic data is provided from the pipeline events. Measurements such as the trigger rates averaged over the run, event timing, deadtime, and Bhabha angular distributions are printed out at the end of each run, in addition to the luminosity, R measurements and chamber efficiencies.

Two additional checks are made at the experiment to monitor the hardware directly. During data taking, a monitor program checks the high voltage power supplies, the CAMAC crate voltages, and the beam energy every 5 minutes. If any of these values is outside of a specified tolerance around their nominal values, the shift takers are notified so they may take the appropriate action without an excessive loss of data. In addition to the automated monitoring, every 8 hours a visual inspection is made of various hardware settings and the gas supply for the tube chambers.

3.2.3 *Offline Data Flow*

In addition to the complete raw data tapes, additional tapes used for calibration are made and sent to SLAC. These calibration tapes are made up of loosely selected Bhabha and $e^+e^- \rightarrow \gamma\gamma$ events. These QED events are the input for both the crystal and tube chamber calibrations. The stripping of these tapes at DESY streamlines the calibration process once the data arrive at SLAC.

Several data sets are produced at DESY for preliminary data analysis. All data are selected with fairly loose cuts since only preliminary calibration constants are available when the selection is done. The hadronic data sample is used for offline measurements of the hadronic cross section and has been used to investigate photon transitions from the $\Upsilon(2S)$. The cascade data sets have been used to study $\Upsilon(2S) \rightarrow \gamma\chi_b \rightarrow \gamma\gamma\Upsilon(1S) \rightarrow \gamma\gamma l^+l^-$ cascade decays. While these samples do not provide final results, they supply an interesting and important preview into the data we collect. These samples also provide an additional diagnostic tool. In particular, on one occasion, an excess of cascade candidates indicated a miscabling which may not have been caught for some time otherwise.

Two additional monitors are provided offline. One monitor is the Doris Bunch Marker (DBM) events discussed in Chapter 2. These events provide information about the beam conditions and how much energy exists in the interaction region when there are no e^+e^- annihilations. This offline monitoring can spot changing beam conditions, 'hot' crystals which have energy deposited in them in a high percentage of beam crossings, and problem tube chamber channels.

While many performance checks which require a small computer load and the statistics of only 1 run may be done online by the PDP, a superior job of monitoring is done offline by the Bicycle-On-Line (BOL) job, albeit with a longer turnaround time. This job offers many of the features of the online pipeline job with additional expanded information. The BOL job provides such things as occupancy plots with various pulse height windows for monitoring the crystal and tube chamber channels,

trigger bit occupancies and rates, and checks of the Time of Flight system. At the time of the dump of the data from the IBM disk to tape, this job is submitted and the results are checked approximately once every 24 hours.

3.3 Preliminary Data Analysis

3.3.1 *Calibration*

The technique used for the calibration and calculation of the crystal energies assumes a linear response between the incident energy and the pulse heights obtained. Because there are two channels for each module, there are two slopes and pedestals which must be calibrated. In practice, the slope of the low energy channel and the ratio of the slopes of the high and low energy channels are used. In order to determine these constants we use a bootstrap approach.

This method of calibration requires the collection of three sets of data. Every two weeks during colliding beam data taking, an 8 hour access is made in order to collect data for the preliminary calibration. To determine pedestal levels for this first stage of calibration, a pulser is used to trigger the experiment with no beams in the machine. These pedestal data are recorded on disk for all online energy measurements made until the next online calibration is recorded. Next, a Cs^{137} source, which emits a .66 MeV gamma-ray is used for preliminary slope measurements. Since this energy is well below all trigger thresholds, an amplifier is used to boost the Σ_9 outputs from each integrate and hold module in order to trigger the experiment. The events are triggered by requiring that the sum of 9 crystals exceeds roughly $\frac{1}{2}$ the energy of the photon emitted from the Cs^{137} source. At these low energies, a good fraction of the photons are fully contained within a single crystal, enabling the photon spectrum to be fit for each crystal and a slope calculated so that the photon peak is at the proper energy.

The second stage of the bootstrap procedure uses photons which are a factor of ten higher in energy than those of Cs^{137} . A Van de Graaff generator is used to

produce 450 keV protons which bombard a fluorine target. The resulting nuclear reactions produce 6.1 MeV photons. At this energy, photons leave their energy spread over more than one crystal in the detector. Since this data is more complicated than the Cs^{137} data, it is written to magnetic tape via the 1600 BPI tape drive located at the experiment and the analysis is continued offline at SLAC. The analysis of these 6 MeV photons begins with the slopes obtained from the Cs^{137} data. Because these photons deposit their energy over more than one crystal, the calibration constants determined from these data depend on the constants of its nearest neighbors and an iterative procedure must be used. Details regarding this procedure may be found in the references.[4]

The results of the Van de Graaff data are used as input for the final stage of calibration which uses the QED data sets sent from DESY to SLAC. Again the energy deposited by electrons and photons at the beam energy is spread over many crystals. An iterative procedure is again used with the resulting constants chosen so that the Bhabha peak is at the beam energy.

The calibration and standard calculation of all energies in the Crystal Ball assume that the response of the detector is completely linear. This is found to not be the case. Evidence for deviations from linearity of ~5% at 100 MeV is presented in Appendix A. Because of the non-linearities found in the data, an additional correction, referred to as ELOG, has been made to all data discussed in this thesis in order to correct for the energy scale errors. These ELOG corrections are discussed in Appendix A.

3.3.2 *Analysis Data Sets*

The data sets we use for the analysis in this thesis correspond to 193,000 $\Upsilon(2S)$ resonance decays from 60.6 pb^{-1} of integrated luminosity and approximately 300,000 $\Upsilon(1S)$ resonance events from ~30 pb^{-1}. The $\Upsilon(2S)$ data were taken from November 1982 to February 1984 with about 40% of the data taken during the first 6 weeks of 1984. About $\frac{2}{3}$ of the $\Upsilon(1S)$ data were taken in August and September of 1984

with the remainder taken sporadically from August 1982 to October 1983.

The number of $\Upsilon(2S)$ resonance decays is determined from the hadronic event data sample. The selection of hadronic events is detailed elsewhere.[5] The two most important elements in the calculation of the number of $\Upsilon(2S)$ produced resonance decays are the amount of continuum hadronic events present in the hadronic sample taken at the $\Upsilon(2S)$ resonance energy and the efficiency for detecting the resonance decays. The off-resonance contribution is estimated from the number of hadronic events found in 4.6 pb^{-1} of data taken at 9.98 GeV, i.e. the continuum below the $\Upsilon(2S)$ resonance. This number is scaled to the amount of luminosity taken at the $\Upsilon(2S)$ and corrected for the $\frac{1}{S}$ dependence of the continuum hadronic cross section. We may write the number of observed $\Upsilon(2S)$ resonance events as:

$$N^{obs}_{\Upsilon(2S)} = N^{had}_{10.023} - N^{had}_{9.98}\frac{L_{10.023}}{L_{9.98}}\frac{(9.98)^2}{(10.023)^2}$$

where $N^{had}_{10.023}$ is the number of hadronic events observed when running on resonance, $N^{had}_{9.98}$ is the number of hadrons observed in the continuum, $L_{10.023}$ is the integrated luminosity at the $\Upsilon(2S)$ center of mass energy, and $L_{9.98}$ is the integrated luminosity taken in the continuum.

The number of observed $\Upsilon(2S)$ decays is related to the number of produced $\Upsilon(2S)$ decays by the detection efficiency:

$$N^{produced}_{\Upsilon(2S)} = \frac{N^{obs}_{\Upsilon(2S)}}{\epsilon_{\Upsilon(2S)}}$$

The detection efficiency $\epsilon_{\Upsilon(2S)}$ is found via Monte Carlo techniques and reflects both the non-hadronic decays of the $\Upsilon(2S)$ and the inefficiency of the cuts used in the selection of hadronic events. We find $\epsilon_{\Upsilon(2S)} = 0.86 \pm 0.07$. The error on the detection efficiency is almost entirely systematic and is due to uncertainties in the modelling of $\Upsilon(2S)$ decays and the detector. More information regarding this efficiency determination is available in the references.[5,6] From the number of

observed hadrons in the continuum and on resonance, the hadronic event detection efficiency, and the luminosities, we find N($\Upsilon(2S)$)=193,000 $\pm$ 15,000 events. The error on the number of events is almost entirely due to the uncertainty in the hadronic detection efficiency.

3.3.3 *Production*

Production is the analysis of the raw data which turns it into useful 4-vectors. During the production of data taken at DORIS II, there is also an attempt to classify and select interesting physics processes such as general hadronic events, exclusive cascade decays of the $\Upsilon(2S)$, and two photon physics events.[7] The production analysis program, EOTAP, also removes events not classified in any predetermined event category in order to reduce the amount of data needing further processing. The cuts in this selection process are scaled to the beam energy so that they make sense for all the running in the DORIS II energy regime. Details of the production analysis beyond that described here may be found in the references.[8,9]

The production begins with the conversion of the raw crystal pulse heights into energies using the calibration constants. Once each crystal has an energy assigned to it, localized regions of energy deposition called 'connected regions' are identified. A given connected region consists of a contiguous set of crystals, each crystal containing greater than 10 MeV of energy. A crystal is a member of a contiguous set if it shares a vertex or face with another member of the set. Figure 3.3 shows a 'flats' display of a hadronic event with the connected region borders outlined. Once these global regions of energy deposition are found, smaller energy maxima are found by the 'bumps' algorithm. This algorithm may unfold two or more particles whose energy depositions overlap forming one connected region.

The bumps algorithm is used for each connected region independently. First the highest energy crystal in a connected region is labelled as a bump module and the 3 nearest neighbors (see Figure 3.4) are associated with it. The energy of the bump module, E_{bump}, is defined as the sum of these four crystals. Other crystals

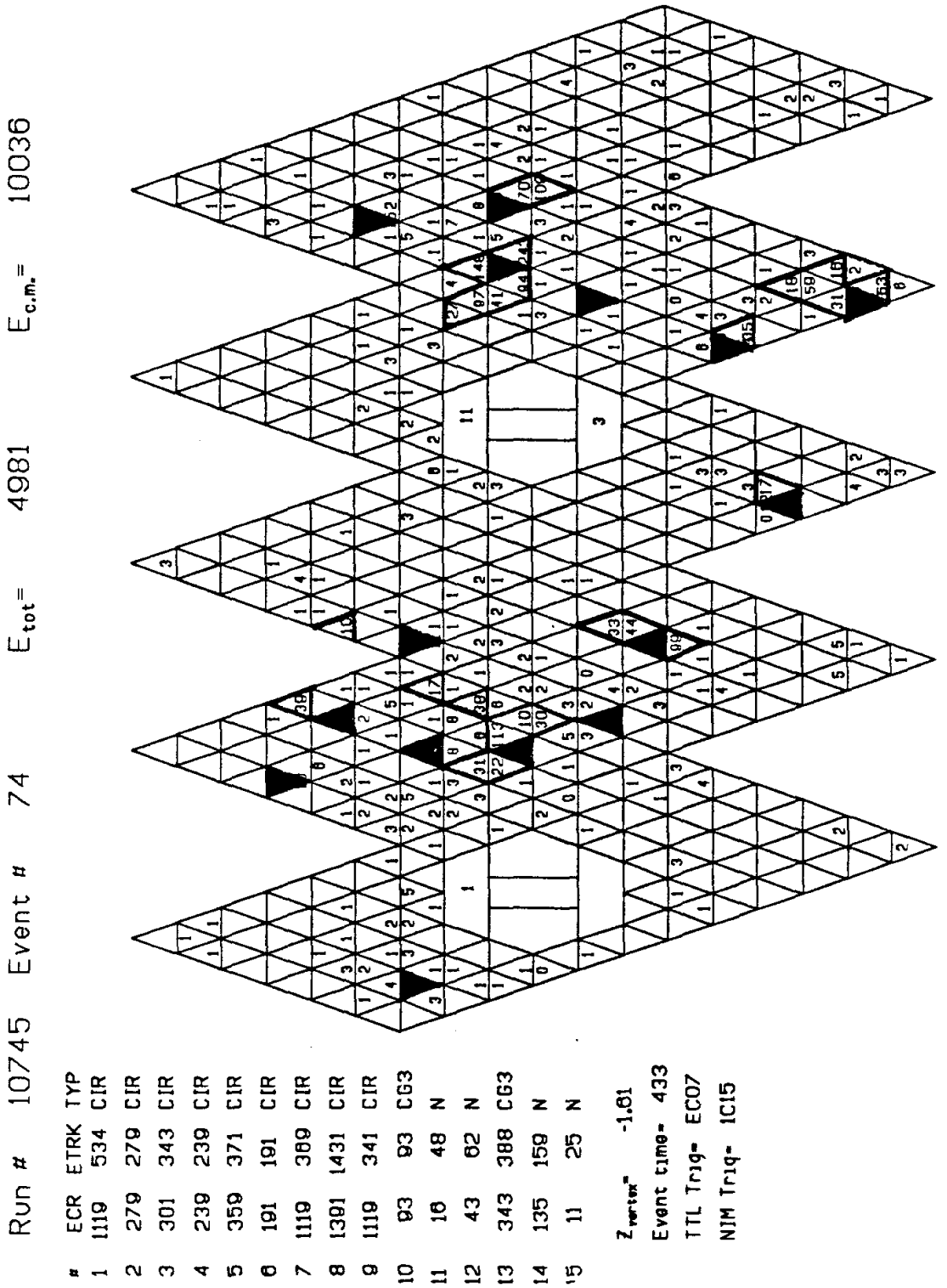

Fig. 3.3 A 'flats' display of a typical hadronic event. The heavy borders indicate the connected region boundaries and the shaded crystals are the bump modules.

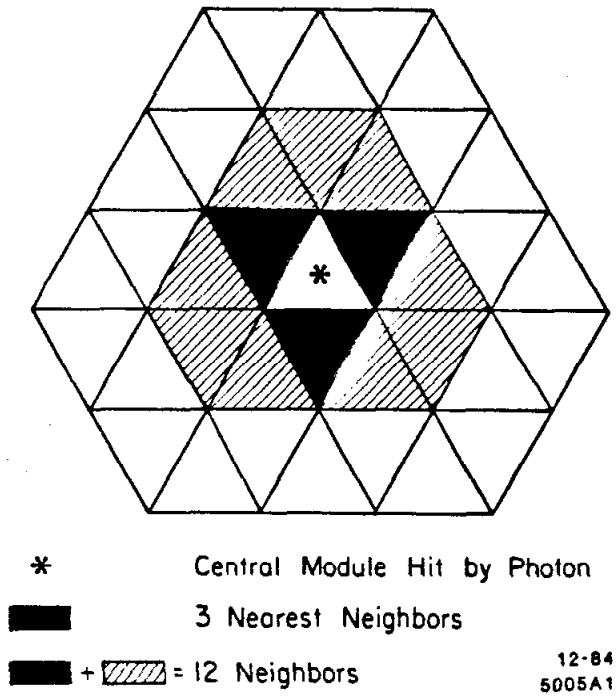

Fig. 3.4 Layout of a central module and the twelve nearest neighbors.

within the connected region are associated with the bump module if:

$$E_i < E_{bump} \times 0.72e^{-9.4(1-cos\theta_i)} \quad \text{for } 15° < \theta_i < 45° \qquad OR \qquad \theta_i < 15°$$

where θ_i is the angle between the i^{th} module and the bump module, and E_i is the energy in the i^{th} module. All crystals in the connected region are tested and if there are any crystals which are not associated with the first bump module, then the process begins again with only the unassociated crystals used. The unassociated crystal with the highest energy is flagged as another bump module and the process continues until all modules in a connected region are either a bump module or are associated with one as indicated above. The completely shaded modules in the event display of Figure 3.3 are bump modules and each bump module is considered to be the location of entry of a different particle into the Crystal Ball.

The bump algorithm was derived empirically for SPEAR data.[10] It is a trade-off between good particle detection efficiency and the creation of spurious particle tracks. While the method used was based on data at lower energies, no problems with the method have appeared at these energies.

Once the bumps step is complete, the process of labelling the events into physics categories begins. This is done after the bumps step in order to reject non-physics background events before the time consuming final stages of production are done. The bump energies and directions are used for this labelling. Ten percent of the events not falling in any of the 'good event' categories are kept for possible checks, the rest are rejected. The cuts for the 'good event' categories are loose enough so that only ~30% of all triggers are rejected.

After this preliminary event selection, the production continues with the tracking stage. First the raw tube chamber pulse heights are transformed into ϕ and z coordinates in the chambers. Particle tracks are fitted using the hits in the chambers forming so called 'IR tracks'. Those tracks which point to a bump module are used for the particle directions assigned to that bump which is labelled as charged. After all tracks are formed, bumps which have not been correlated with chamber tracks are tagged as charged or neutral based on the remaining hits in the chambers. Tagging a bump as charged requires one hit within a ϕ,z window around the bump. A tagged charged track is assigned the direction of the bump module. Once all bumps have been classified as neutral, charged tagged, or charged IR tracks, the tracking step is complete and track energies and neutral track directions can be assigned.

The ESORT stage of analysis sorts out energy assignments and particle directions. The standard Crystal Ball method of measuring energies is called the sum of thirteen (Σ_{13}). The term Σ_{13} refers to the sum formed from the raw energy in the bump module and the twelve surrounding neighbors (see Figure 3.4), corrected for two effects. The first correction is for energy deposited which is not contained in the volume of the 13 crystals. The fraction of energy outside the group of 13 is found

to be 2.25% for Bhabha events and this is used as an estimate for all measurements of Σ_{13}. The second correction is due to the fact that the energy measured by the raw sum of 13 depends on the position of entry of the incident particle. Those particles entering a crystal near the gap between crystals leave a larger fraction of their energy in the material between the crystals where it is unmeasured. The position correction, called PCORR, is based on the ratio of the energy in the bump module divided by the raw sum of thirteen.[4] The standard Σ_{13} is formed from the raw sum of thirteen modules, corrected for these losses.

The directions used for neutral energy depositions are based on the expected shape of energy depositions of photons in NaI(Tℓ) based on Monte Carlo studies. Each bump module is divided into 16 submodules for calculational purposes. A photon entering a given submodule leaves a pattern of energy deposited in neighboring crystals which, on average, is distinct from a photon entering another submodule. The neutral particle is considered to have entered the submodule where the differences between the expected and observed energy depositions in the group of 13 are minimized. The direction cosines of the photon are assigned those of the submodule chosen. Note that the directions of neutral particles are quantized due to this technique.

The final step of the analysis is the time of flight analysis step. The purpose is to associate hits in the time of flight counters with particle tracks and provide information as to the time a given particle traversed the counter. Since this apparatus is not used in this analysis, details are left to the references.[11]

Once the production is completed, two data sets are written to tape. The full data set written consists of all events tagged as physics events and 10% of those events not labelled as physics events by EOTAP. The second data set is a summary data set consisting of all events tagged by the hadron event selector and those tagged in the 'cascade event' selector of EOTAP. The cascade data set consists of all events loosely classified as $\Upsilon(2S) \rightarrow \pi\pi\Upsilon(1S)$ or $\Upsilon(2S) \rightarrow \gamma\gamma\Upsilon(1S)$ with the $\Upsilon(1S)$ decaying into e^+e^- or $\mu^+\mu^-$. All cuts made by EOTAP may be found in the

references.[7]

3.3.4 *Post Production Re-analysis*

As stated in Chapter 2, we ignore the tracking chamber information for this analysis. In order to do this, we redo part of the production process, ignoring the tracking chambers. The events labelled as 'cascade events' by EOTAP are stripped from the output data tapes and are inserted into the re-analysis chain. The first step of the re-analysis is to discard all the information from production after the bumps step. The new analysis skips the chamber tracking section completely so that all particles are considered neutral for purposes of assigning direction cosines. Once the tracking step is skipped, the ESORT step continues normally. The cascade data set output from this re-analysis is the input data set to the final event selection discussed in Chapter 4. The result of this re-analysis is that all chamber information has been ignored and all direction cosines are calculated from an event vertex at z=0. The method of determining particle directions in ESORT now applies to all bumps.

References

1) D. P. Barber *et al.*, *Phys. Lett.* **135B** (1984) 498.

2) I. M. Ternov, Y. M. Loskutov, and L. I. Korovina, *Zh. Eksp. Teor. Fiz.* **41** (1961) 1924 [*Sov. Phys.–JETP* **14** (1962) 921].
Sokolov, A.A., and Ternov, I.M. R, *Dokl. Akad. Nauk. SSS* **153** (1963) 1052 [*Sov.Phys.–Dokl.* **8** (1964) 1203].

3) B. Lockman, Crystal Ball note 157, 1982.

4) R. Lee, Ph. D. thesis, Stanford University, 1985, and SLAC Report 282 (unpublished).

5) R. Nernst, Ph. D. thesis, Universität Hamburg, 1985 (unpublished).

6) R. Clare, and J. Irion, Crystal Ball note 166, 1985.

7) J. Gaiser, D. Gelphman, J. Irion, B. Lockman, and J. Tompkins, Crystal Ball note 167, 1983.

8) M. Oreglia, Ph. D. thesis, Stanford University, 1980, and SLAC Report 236 (unpublished).

9) Crystal Ball Offline Workshop, SLAC, August 29-September 2, 1983.

10) R. Partridge, Crystal Ball note 6, 1979.

11) D. Prindle, Ph. D. thesis, Carnegie–Mellon University, 1985 (unpublished).

Chapter 4

Final Analysis and Results

4.1 Data Analysis

4.1.1 *Introduction*

To study $\Upsilon(2S) \rightarrow \pi^0\pi^0\Upsilon(1S)$ transitions we choose the exclusive channel where the $\Upsilon(1S)$ decays to e^+e^- or $\mu^+\mu^-$ and the pions each decay into two photons.* This removes the large background of continuum and resonance events which contain many π^0's not associated with the $\pi^0\pi^0$ transitions from the $\Upsilon(2S)$ to the $\Upsilon(1S)$. Selection of the leptonic decays of the $\Upsilon(1S)$ gives the opportunity of observing these hadronic transitions with very little background.

The characteristic topology of these events is important for the selection process. The final state consists of $\gamma\gamma\gamma\gamma l^+l^-$ ($l = \mu$ or e) where the two leptons from the decay are essentially back to back since the mass of the $\Upsilon(1S)$ is large compared to the total energy available (563 MeV) to the four photons. This means that the $\Upsilon(1S)$ is moving slowly and the leptons resulting from the $\Upsilon(1S)$ decay do not fold

* Because no charged particle tagging is used, events where one or both of the pizeros decays via the Dalitz decay $\pi^0 \rightarrow \gamma e^+e^-$ (which occurs in less than 3% of the events) may look identical to the case where each π^0 decays into two photons. The Dalitz decay is included in the Monte Carlo modelling of the π^0 decays in order to properly calculate the efficiency.

up appreciably. The minimum opening angle between the leptons is realized when the kinetic energy of the $\Upsilon(1S)$ is maximum. This is the case when the invariant mass of the $\pi^0\pi^0$ system ($M_{\pi^0\pi^0}$) is minimum (i.e. $M_{\pi^0\pi^0}=2M_{\pi^0}$) and the minimum opening angle is 174°.

Identifying these $\gamma\gamma\gamma\gamma l^+l^-$ events requires the particle identification allowed by the Crystal Ball detector. Electrons and photons create electromagnetic showers in the sodium iodide. The pattern of energy deposition in the NaI(Tℓ) can be used to separate electromagnetically showering particles from other types of particles. Figure 4.1 is a $\gamma\gamma\gamma\gamma e^+e^-$ event candidate. This picture (a so called 'flats') is a projection of the crystal faces of the main Ball onto a flat page as discussed in Chapter 2. This flat display of the crystals gives a good indication of the typical pattern of energy deposition for electrons and photons. The energy deposited in each ring of crystals around the central one falls off smoothly as one moves away from the centroid of the shower. One observes that much of the energy is deposited in the central module of the shower with less energy deposited in the three surrounding modules and still less in the nine crystals surrounding the central four. Most of the energy of an isolated electromagnetic shower in the Crystal Ball is contained in the thirteen crystals around the point of entry. The energy measurement provided by the sum of the 13 crystals around and including the crystal with the maximum energy (referred to as Σ_{13}*) is approximately proportional to the energy of the incident electron or photon. The deviation from an ideal relationship between the energy measured with Σ_{13} and the incident energy is discussed in Appendix A.

Minimum ionizing particles such as energetic muons have a qualitatively different pattern of energy deposition. Figure 4.2 is a candidate $\gamma\gamma\gamma\gamma\mu^+\mu^-$ event. The muon candidates indicated have the typical signature of a minimum ionizing particle. The energy deposited is usually confined to one or two crystals with less

---

* Corrections such as PCORR and the correction for leakage outside the group of thirteen crystals are included in Σ_{13} as discussed in Chapter 3.

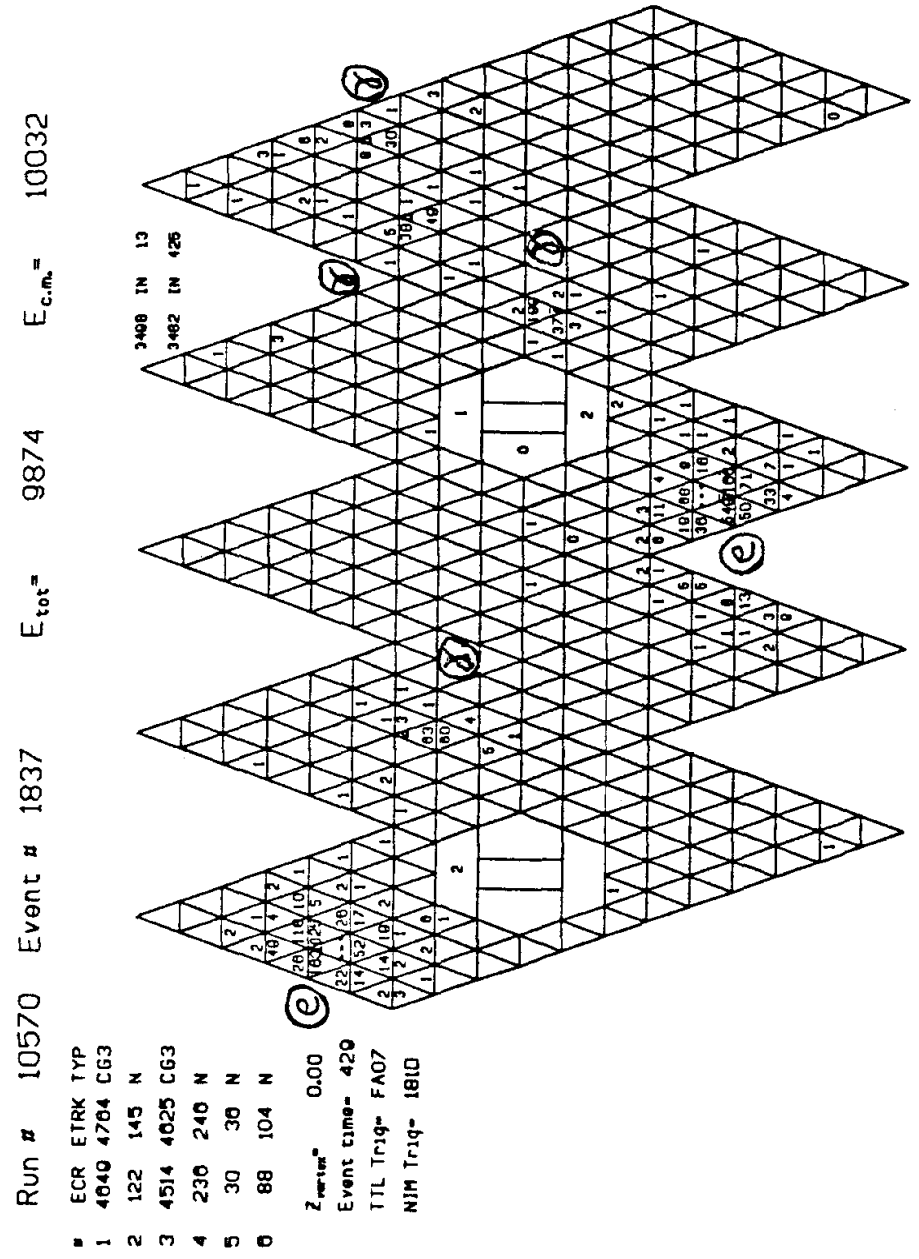

Fig. 4.1 A $\gamma\gamma\gamma\gamma e^+e^-$ candidate event shown as a 'flats' projection. Typical electron and photon showers are indicated.

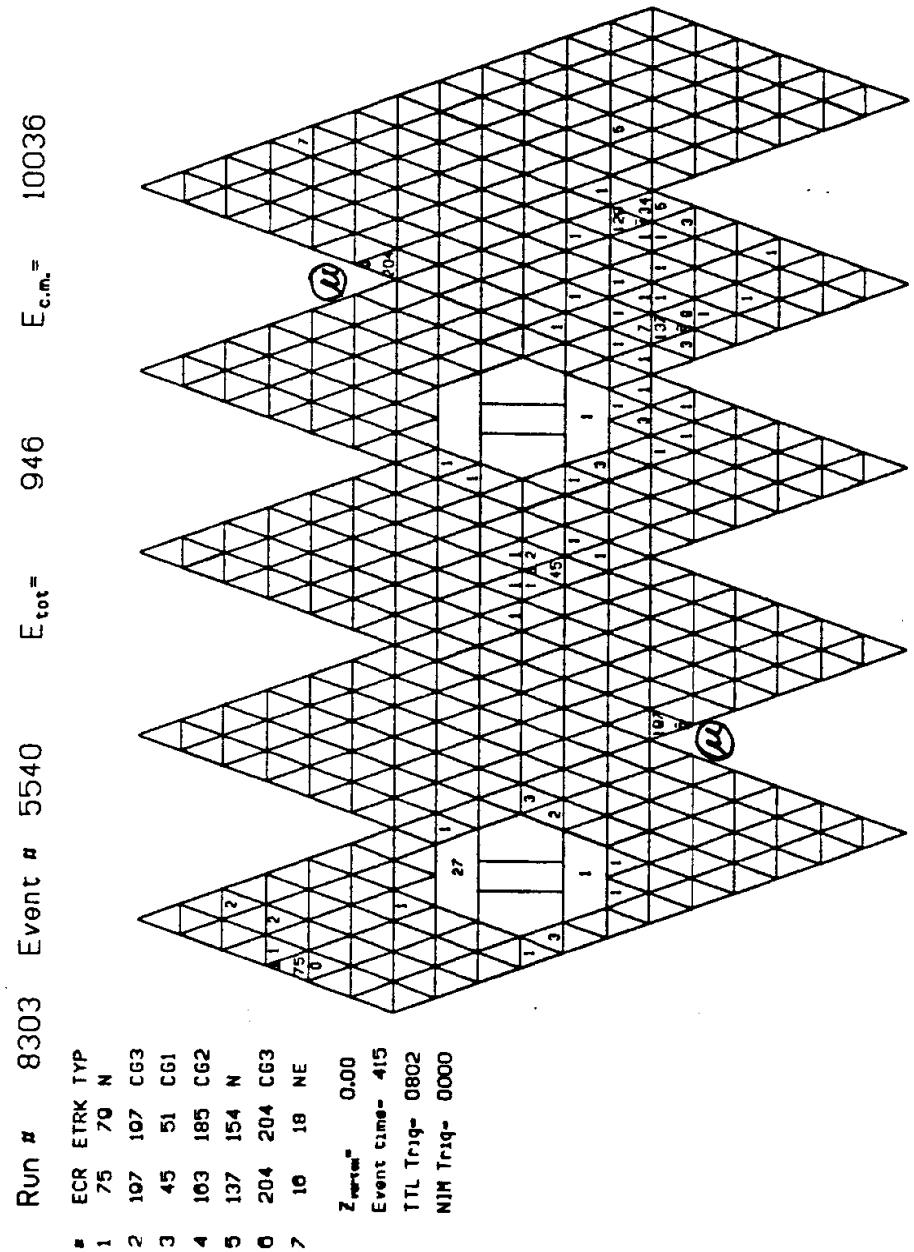

Fig. 4.2 A candidate $\gamma\gamma\gamma\gamma\mu^+\mu^-$ event shown in the 'flats' display. The typical energy deposition for a muon is indicated.

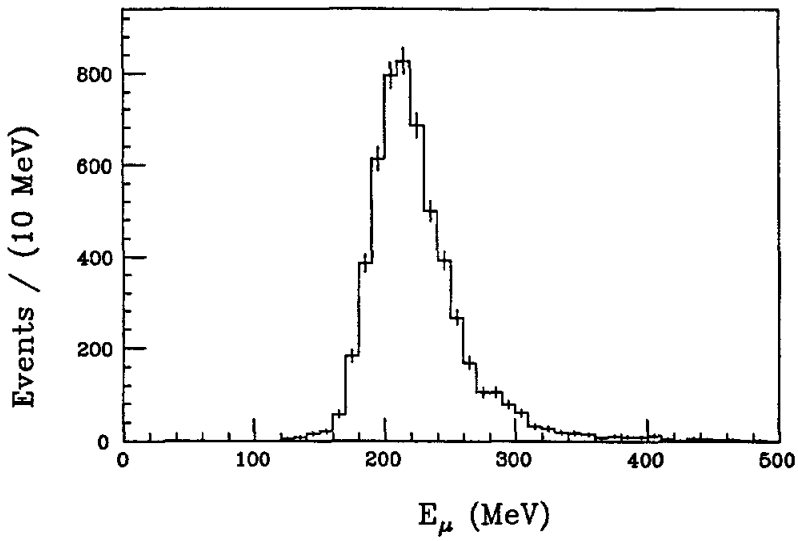

Fig. 4.3 The measured energy distribution of ~5 GeV muons from $e^+e^- \rightarrow \mu^+\mu^-$ events at the $\Upsilon(1S)$.

than 10 MeV of energy occasionally deposited in one or two other crystals in the group of thirteen crystals. The measured energy is not proportional to the incident energy but rather is distributed in a Landau distribution with a most probable energy loss of about 205 MeV and a Landau tail extending toward higher energies. Figure 4.3 shows the measured energy of ~5 GeV muons from $e^+e^- \rightarrow \mu^+\mu^-$ annihilation events.[1]

These features of energy deposition are used in the selection procedure to identify photons as well as muons. The selection methods we use involve ratios of the energy contained in various combinations of crystals surrounding, and including, the module with the highest energy (the so called 'bump' module). Figure 4.4 indicates the geometry used for the cuts on the energy patterns. The relevant quantities are:

a) E_1, which is the energy in the bump module and is the largest of the group of 13 modules,

b) E_2, which is the sum of the energy in the bump module and the energy contained in the crystal with the second highest energy in the group of thirteen,

c) E_4, which is the summed energy of the bump module and the three modules

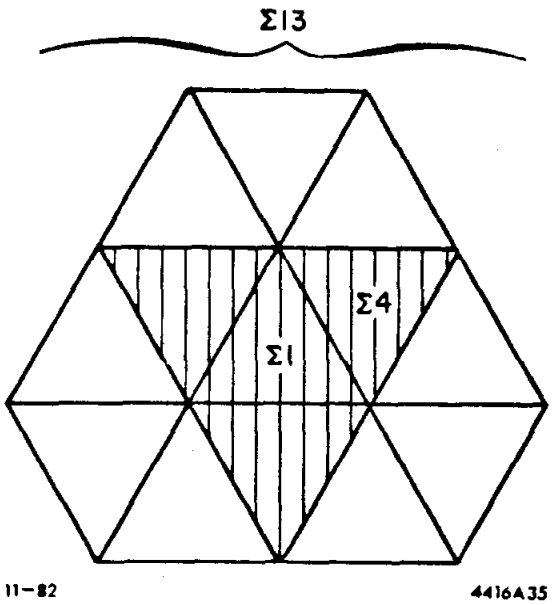

Fig. 4.4 The thirteen crystals used for making the energy measurements and pattern cuts. The bump module, the group of four and group of thirteen are indicated.

surrounding the bump module, and

d) E_{13}, which is the sum of the energies in the thirteen modules indicated in Figure 4.4.

The ratios $\frac{E_1}{E_4}$, $\frac{E_2}{E_4}$, and $\frac{E_4}{E_{13}}$ all quantify the relative energy fraction which is located in the different regions around the central module. For minimum ionizing particles, the fractions $\frac{E_2}{E_4}$ and $\frac{E_4}{E_{13}}$ are nearly 1 since the energy from minimum ionizing particles is mostly distributed in only one or two crystals. For photons, the energy is distributed more uniformly and the corresponding ratios are lower. Detailed studies of photons and minimum ionizing particles have been conducted by John Gaiser in his thesis work and the results of those studies[2] are used in this analysis. Table 4.1 lists the pattern cuts used for identifying photons and muons.*

* There exists some overlap in the pattern cuts such that some particles may be classified as a photon *and* a muon. Because of this problem, we require muon and photon candidates to

Called Muon If:	$\frac{E_4}{E_{13}} \geq 0.9875$	OR	$\frac{E_2}{E_4} \geq 0.9975$
	OR		
	$\frac{E_4}{E_{13}} \geq .95$ AND $\frac{E_2}{E_4} \geq .9975\text{-}(\frac{E_4}{E_{13}}\text{-}.95)^{1.23}$		
Called Photon If:	$0.4 \leq \frac{E_1}{E_4} \leq 0.98$		
	AND		
	$0.7 \leq \frac{E_4}{E_{13}} \leq 0.995$		

Table 4.1 Pattern cuts used to define muons and photons.

Each of these pattern cuts has a transmission efficiency of greater than 90%.

4.1.2 *Event Selection*

The input data set to the final selection process is the preselected data discussed in Chapter 3. This is the re-analyzed output from the production job EOTAP. The selection process continues by strengthening cuts made by EOTAP and adding new selection criteria which eliminate substantial background. The EOTAP selection adds no cuts beyond the final selection discussed here; hence, we discuss only the final selection procedure itself.

The analysis of the data is broken up into two separate categories, one for $\gamma\gamma\gamma\gamma\mu^+\mu^-$ events and one for $\gamma\gamma\gamma\gamma e^+e^-$ events. The quantity E_{vis}, defined as the sum of the energy in all the NaI(Tℓ) modules, is used to define the two categories. As Figure 4.3 indicates, a typical muon deposits significantly less than its total energy in the crystals. Electrons and photons leave essentially all their energy in the NaI(Tℓ). This means that $\gamma\gamma\gamma\gamma\mu^+\mu^-$ events have a much lower total energy deposition than $\gamma\gamma\gamma\gamma e^+e^-$ events. The maximum energy of the four photons (without including detector resolution effects) in a given $\pi^0\pi^0 l^+l^-$ event is the mass difference: $\Delta M = M(\Upsilon(2S)) - M(\Upsilon(1S)) = 563.3$ MeV.[3]

fulfill other requirements besides the pattern cuts.

Analysis Cuts	$\pi^0\pi^0 e^+e^-$ candidates	$\pi^0\pi^0\mu^+\mu^-$ candidates
EOTAP Selection	105207	105207
Energy Limits	29903	75042
Exactly 6 Particles	741	21012
2 Leptons	697	1708
Overlap Cut	398	989
Cleanliness Cut ($\pi^0\pi^0\mu^+\mu^-$ only)	N.A.	268
γ Pattern Cut	341	137
Fit CL>0.05	315	95
π^0 Mass Cut	50	50
ΔM Cut	46	44

Table 4.2 Table of cuts for the $\pi^0\pi^0 l^+l^-$ analysis. The ordering of the cuts and the number of events remaining after each cut are indicated.

The $\gamma\gamma\gamma\gamma\mu^+\mu^-$ events deposit approximately 970 MeV of energy on average if all particles are within the 93% solid angle of the main Ball. To allow for resolution effects and the variation of the measured muon energies, an event is processed further as a $\gamma\gamma\gamma\gamma\mu^+\mu^-$ candidate if 600 $MeV < E_{vis} <$ 1300 MeV. Since $\gamma\gamma\gamma\gamma e^+e^-$ events leave the entire center of mass energy deposited in the detector, an event is considered a $\gamma\gamma\gamma\gamma e^+e^-$ candidate if 8 $GeV < E_{vis} <$ 12 GeV. All events with E_{vis} outside of either of these ranges are rejected. Table 4.2 indicates the amount of data remaining in each data category after this cut is made.

All remaining events are required to have exactly 6 particles within $|cos\Theta| \leq .85$ where Θ is defined as the polar angle of the particle relative to the incoming positron beam direction. Throughout, the term *particle* refers to a localized energy cluster which passes the bump discriminator described in Chapter 3. This solid angle cut requires that all particles are located in the main Ball and are away from the

edge effects of the tunnel modules. Any energy clusters outside the $|cos\Theta| \leq .85$ region are ignored for particle counting purposes. Events are rejected if any of the 6 particles in the detector overlap such that $\cos\theta_{ij} > 0.9$ for any particles in the event, where the angle θ_{ij} is the angle between any two particles in a given event. This ensures that an energy measurement is made for each particle without overlapping energies with another particle in the event.

We require 4 photon candidates and 2 lepton candidates in each event. The lepton pair from $\gamma\gamma\gamma\gamma l^+l^-$ events is required to be colinear with the maximum acollinearity being 17 degrees.* For electron events, the electrons are each required to deposit $\geq$ 3.5 GeV. For muon events, the muons are required to deposit between 150 MeV and 330 MeV each and also pass the pattern cut for minimum ionizing particles indicated in Table 4.1.

The remaining 4 particles in each event are considered photon candidates. To remove background while retaining a high efficiency, a pattern cut is made only on photons with E_{13}> 100 MeV. Photons of lower energy are more likely to have an asymmetric energy deposition and therefore have a reduced transmission efficiency. The pattern cut used for electromagnetically showering particles is listed in Table 4.1. An event is rejected if any photon candidate of $E_{vis} > 100$ MeV fails to pass the pattern cut.

A possible background in the $\pi^0\pi^0\mu^+\mu^-$ channel is from real $\pi^0\pi^0\pi^+\pi^-$+ X events where the charged pions may mimic the signature of muons. This type of background may leave a spray of energy in the Ball from the interaction of the charged pions in the sodium iodide or extra energy in the endcap crystals. To suppress this type of background, as well as muon events with lots of beam related

* The kinematic limit of the acollinearity of leptons originating from $\Upsilon(2S)\rightarrow\pi^0\pi^0\Upsilon(1S)\rightarrow \gamma\gamma\gamma\gamma l^+l^-$ is 6°. The larger acollinearity value used in this analysis also takes into account the uncertainty in the angular measurements of the leptons due to the detector angular resolution and the 2.5 cm DORIS bunch length.

spray, a cut is made on the event cleanliness. The excess energy in the main Ball which is not assigned to any of the 6 particles must be less than 80 MeV, and the sum of all endcap energy must be less than 40 MeV.† A study of random beam crossing triggers (the DBM events discussed in Chapter 2) together with the Monte Carlo studies (see below) indicates that these cuts do not remove a significant number of good events.

The remaining events are subjected to a 2 constraint (2–C) kinematic fit to energy and momentum conservation. Both event samples are fit using the photon energies as measured quantities and the lepton energies as being unmeasured.* Each event is required to fit the hypothesis of four-momentum conservation with a confidence level exceeding 5%. The confidence level for all events subjected to the fit is shown in Figure 4.5.

4.1.3 *Final Selection*

The photons in the remaining events are used to select for events with two $\pi^0 s$. In Figure 4.6 we plot the two photon invariant mass $m_{\gamma\gamma}$ of each pairing combination versus the invariant mass of the remaining photons. Figure 4.6a is a plot for electron candidate events and Figure 4.6b is the corresponding plot for muon candidate events. The scatter plots contain three entries for each event due to the different combinations of the four photons. There is a clear clustering of events around the region corresponding to two $\pi^0 s$ in an event. Figures 4.7a,b are projections of the scatter plot onto a single axis, where there are six $m_{\gamma\gamma}$ combinations per event. Figures 4.7a,b correspond to the electron and muon candidates respectively.

---

† Excluded from the endcap energy sum are the two modules 723 and 777 which measure non-negligible amounts of energy during a large fraction of the beam crossings.

* The electron energies are not used as constraints in the fitting procedure. A discussion of this point and further details of the kinematic fitting procedure may be found in Appendix B.

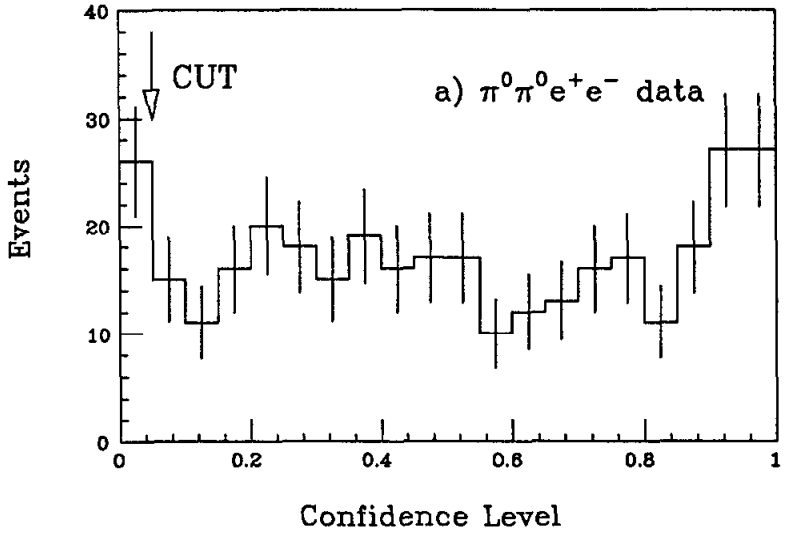

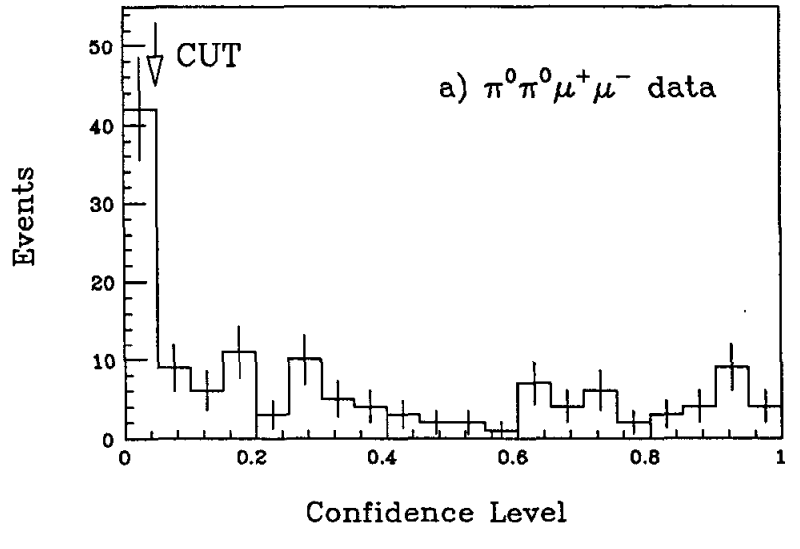

Fig. 4.5 Confidence level distributions of fits to the a) $\gamma\gamma\gamma\gamma e^+e^-$ and b) $\gamma\gamma\gamma\gamma\mu^+\mu^-$ final states.

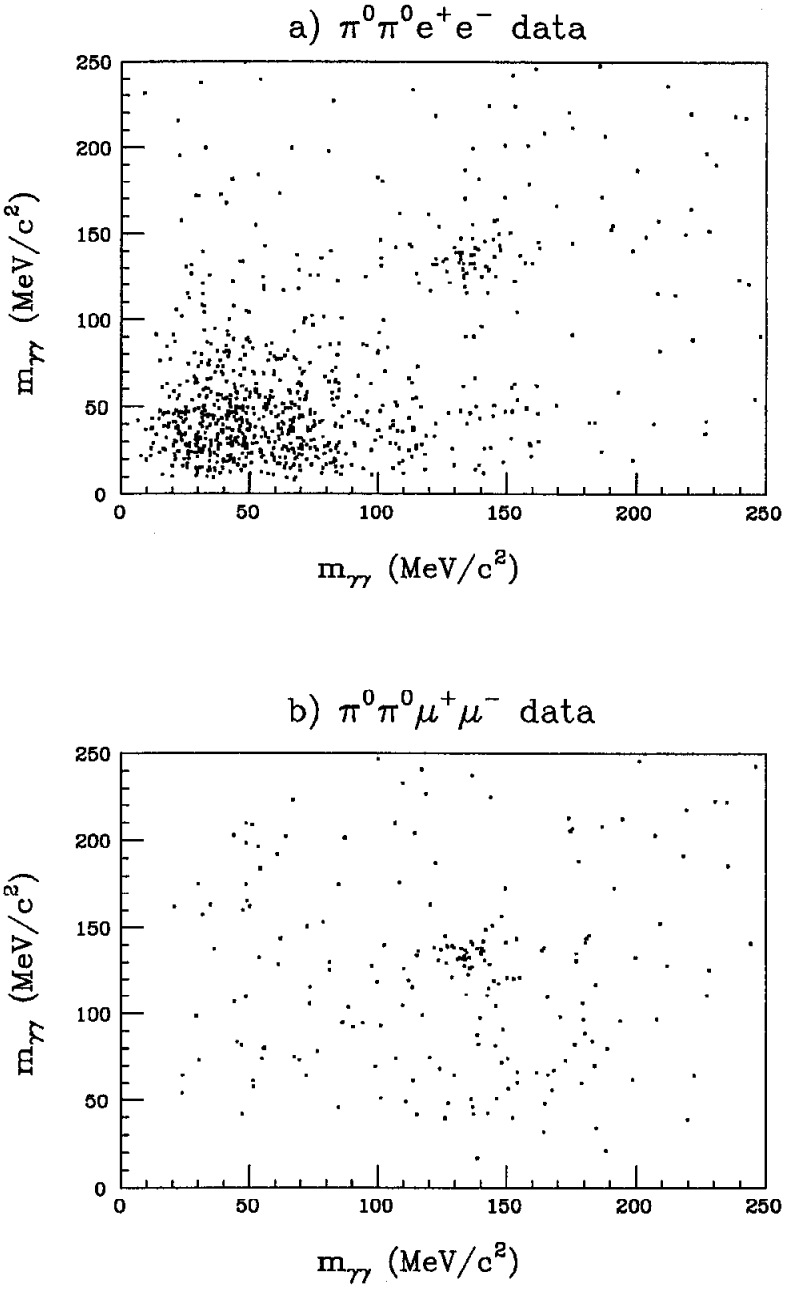

Fig. 4.6 Scatter plot of $m_{\gamma\gamma}$ vs $m_{\gamma\gamma}$ for a) $\gamma\gamma\gamma\gamma e^+e^-$ events and b) $\gamma\gamma\gamma\gamma\mu^+\mu^-$ events. There are three entries per event.

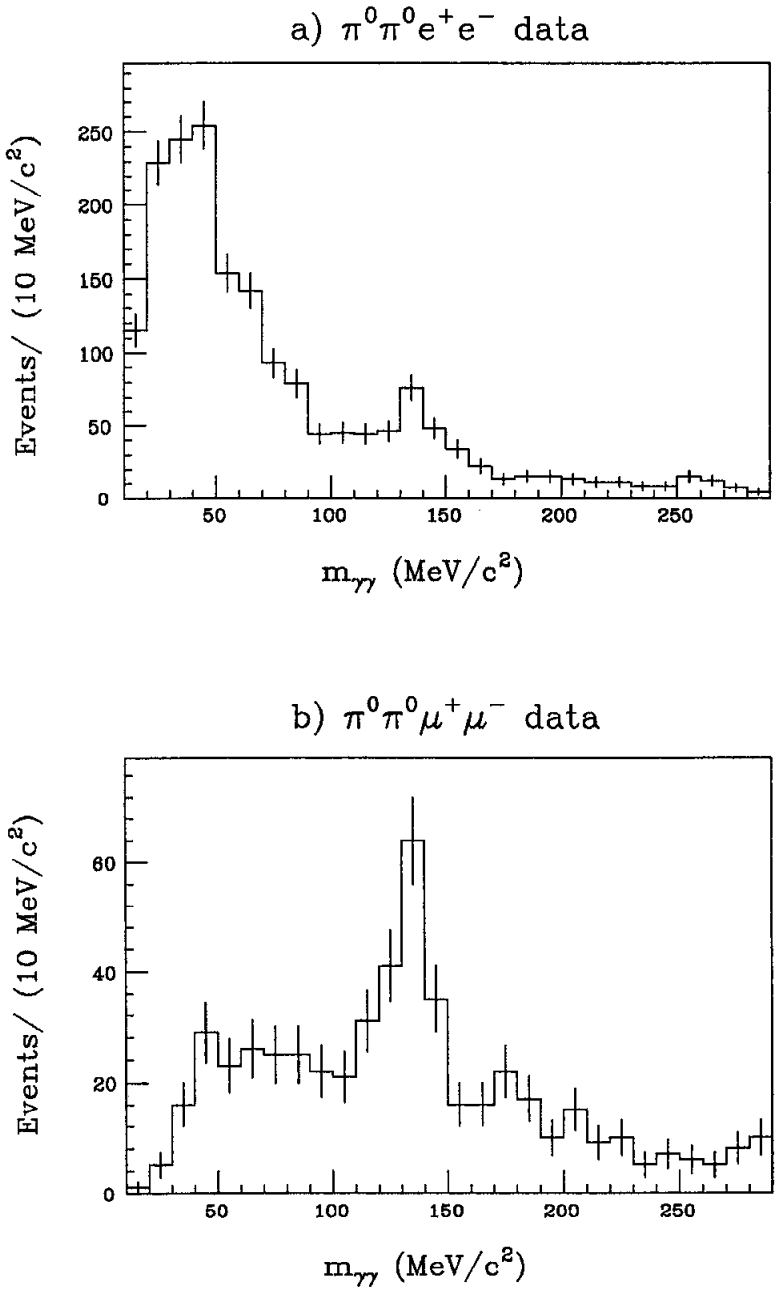

Fig. 4.7 All $\gamma\gamma$ mass combinations for a) $\gamma\gamma\gamma\gamma e^+e^-$ events and b) $\gamma\gamma\gamma\gamma\mu^+\mu^-$ events. There are 6 $\gamma\gamma$ mass combinations for the four photons in each event.

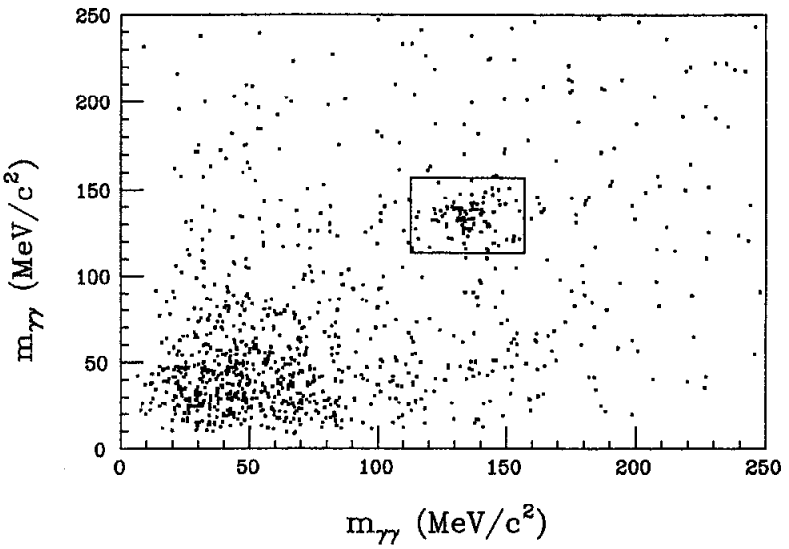

Fig. 4.8 Scatter plot of $m_{\gamma\gamma}$ vs $m_{\gamma\gamma}$ for both $\gamma\gamma\gamma\gamma e^+e^-$ and $\gamma\gamma\gamma\gamma\mu^+\mu^-$ candidate events. The box indicates the cut at ± 22 MeV/c^2.

We see evidence for $\pi^0 s$ in both channels although the total number of counts is about 3 times larger for electron events than for the events in the muon channel. The bulk of this background in the electron channel is due to radiative Bhabha events with extra energy clusters. These extra energy clusters can result from either spurious energy which is beam related or from fluctuations in the large electromagnetic showers of electrons. Sometimes fluctuations in the shower profile of high energy showers can cause the detection of low energy bumps (called 'splitoffs') near the electrons but outside of our overlap cut. Because these clusters typically have energy $\leq$ 50 MeV, the invariant masses formed from them is low. Note that the muon candidates (Figure 4.7b) do not suffer from this low mass background. A contribution to the background, present in both channels throughout the $\gamma\gamma$ mass spectrum, is due to miscombinations of photons from real $\pi^0\pi^0$ events.

Figure 4.8 indicates the cut made to further select $\pi^0\pi^0$ events. The box indicates the cut which is made at ± 22 MeV/c^2 on both axes around the π^0 mass. This requires that each event have one combination of the four photons into pairings $m_{\gamma_1\gamma_2}, m_{\gamma_3\gamma_4}$ within the above limits. This cut corresponds to approximately ± 3

standard deviations of our π^0 mass resolution.

For the 100 events remaining after the $2\pi^0$ cut, we calculate the mass difference $\Delta M = M(\Upsilon(2S)) - M_{recoil}$. The quantity M_{recoil} is the mass recoiling against the four photon system and is calculated from the energy corrected four-momentum vectors of the photons. For transitions from the $\Upsilon(2S)$ to the $\Upsilon(1S)$, we expect ΔM to peak at about 563 MeV/c^2, the mass difference of the $\Upsilon(2S)$ and $\Upsilon(1S)$.[3]

Figures 4.9a,b are histograms of this mass difference for electron and muon candidates. Both data sets show a large peak at about 560 MeV/c^2 with a small amount of background on either side of the peak.* The final cut is made by requiring $\Delta M = 563 \pm 60$ MeV/c^2. The ΔM resolution based on the energy and angular resolution is about 18 MeV/c^2, so ± 60 MeV/c^2 is slightly greater than ± 3 standard deviations. Figure 4.10 is a plot of all the data with the expectation for the width based on energy and angular resolution overlaid and indicates good agreement between the curve and the data. After the ΔM cut we find 46 $\pi^0\pi^0 e^+e^-$ events and 44 $\pi^0\pi^0\mu^+\mu^-$ events.

4.1.4 *Background Estimates*

We estimate the background contribution to the signal by examination of the sideband regions around the signal region, each of equal area to the signal region. As indicated in Figure 4.9, the sidebands range from 443-503 MeV/c^2 and 623-683 MeV/c^2. The amount of background contained in the signal region is estimated by averaging the number of events in the two sideband regions. We find 4 sideband events in the electron channel and estimate 2 ± 1 background events in the final sample of 46 $\pi^0\pi^0 e^+e^-$ events. In the muon channel we find 2 sideband events and estimate $1 \pm \frac{\sqrt{2}}{2}$ background events in the final sample of 44 $\pi^0\pi^0\mu^+\mu^-$ events. For branching ratio calculations, these numbers of background events are subtracted

* Note that this mass difference was forced to peak at 563 MeV as part of the ELOG energy corrections derived from the $\pi^0\pi^0 l^+l^-$ and $\gamma\gamma l^+l^-$ events, as discussed in Appendix A.

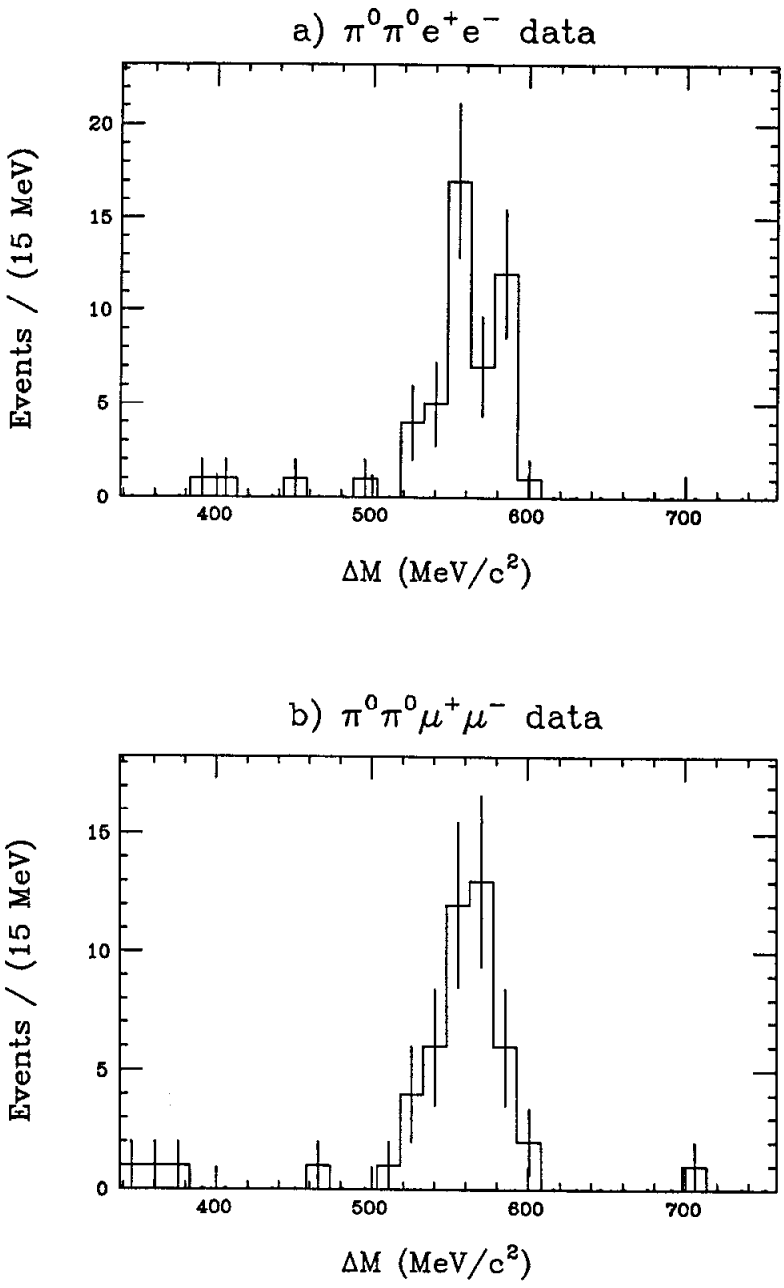

Fig. 4.9 The mass difference $\Delta M = M(\Upsilon(2S)) - M_{recoil}$ for a) $\gamma\gamma\gamma\gamma e^+e^-$ event candidates and b) $\gamma\gamma\gamma\gamma\mu^+\mu^-$ events.

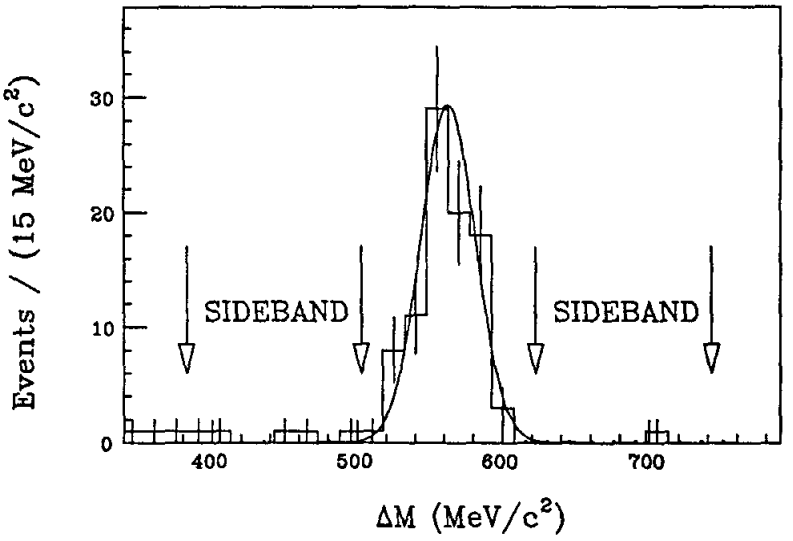

Fig. 4.10 ΔM distribution for both $\gamma\gamma\gamma\gamma e^+e^-$ events and $\gamma\gamma\gamma\gamma\mu^+\mu^-$ events. The curve represents the width expected for this distribution based on energy and angular resolution. The sideband regions around the signal region are indicated.

from the number of observed events listed above.

Possible sources of background in our data sample are the following processes:

a) $\Upsilon(2S) \to \pi^0\pi^0\Upsilon(1S)$ with the $\Upsilon(1S)$ decaying into $\tau^+\tau^-$,

b) cosmic ray events,

c) radiative Bhabha events with additional spurious energy in the detector,

d) low multiplicity hadronic events originating from $\Upsilon(2S)$ decays or continuum processes,

e) photon cascades $\Upsilon(2S) \to \gamma\chi_b \to \gamma\gamma\Upsilon(1S) \to \gamma\gamma l^+l^-$ with additional spurious energy in the detector, and

f) $\pi^+\pi^-$ cascades from the $\Upsilon(2S)$ to the $\Upsilon(1S)$ with extra tracks in the detector.

The $\tau^+\tau^-$ contribution has been studied by Monte Carlo techniques. We generate $\pi^0\pi^0\tau^+\tau^-$ Monte Carlo events and transport them through a simulation of the detector (see below for details of the Monte Carlo simulation). After applying the full analysis to 2600 events, we find 2 events in the $\pi^0\pi^0\mu^+\mu^-$ channel

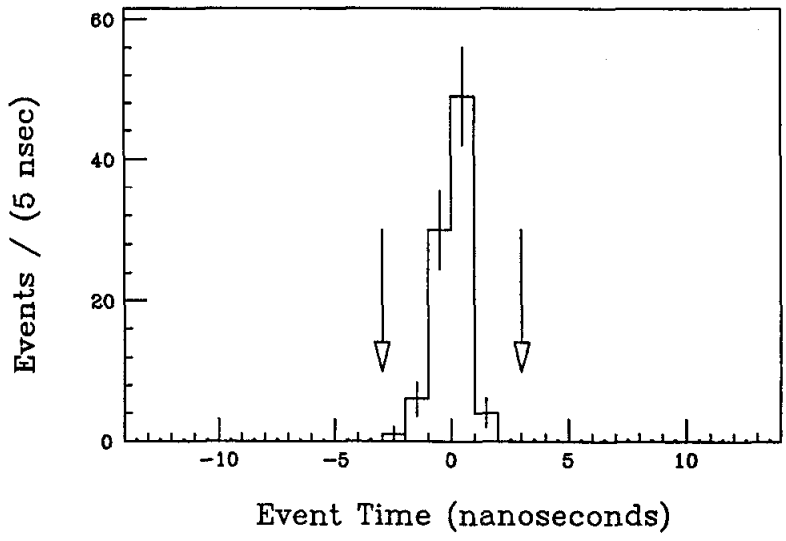

Fig. 4.11 The event timing information for all events passing the π^0 mass cuts. Events originating from the beam crossing should be within the window indicated by the arrows at 0 ± 3 nanoseconds.

and no events in the $\pi^0\pi^0 e^+e^-$ channel. We calculate the expected number of $\pi^0\pi^0\tau^+\tau^-$ decays in our $\Upsilon(2S)$ data sample by using previous measurements of $\mathrm{Br}(\Upsilon(2S)\to\pi^+\pi^-\Upsilon(1S)\to\pi^+\pi^- l^+l^-)$, and assuming an I=0 assignment for the $\pi\pi$ system. For the $\pi^0\pi^0\tau^+\tau^-$ background contribution in our sample we estimate no events in the $\pi^0\pi^0 e^+e^-$ channel and ~ 0.4 events in the $\pi^0\pi^0\mu^+\mu^-$ channel. Due to the small size of these estimates, this background is neglected.

The cosmic ray background is estimated by examining the event timing information, described in Chapter 2, for the $\pi^0\pi^0 l^+l^-$ events in both the signal and sideband region of the ΔM plot. The event time for all events lies within the timing window expected for events originating from the colliding beams. With no events found in the sidebands of this timing plot, we conclude that the number of cosmic ray events in the signal region is negligible.

The background processes c) and d) above are estimated from the $\simeq 30 pb^{-1}$ of $\Upsilon(1S)$ resonance data. The $\Upsilon(1S)$ data represents about half the number of continuum events and about 1.5 times the number of resonance decays in our analyzed

$\Upsilon(2S)$ data sample. The same cuts, scaled for the different center of mass energies of the $\Upsilon(2S)$ and $\Upsilon(1S)$, are applied to the data. We find one $\pi^0\pi^0\mu^+\mu^-$ event and no $\pi^0\pi^0 e^+e^-$ events after all cuts.

The background contribution from the photon transitions through the χ_b states is estimated via similar Monte Carlo techniques as described for process a) above. We again find a negligible number of events in the signal region and neglect the contribution of this background process to the signal.

The decays $\Upsilon(2S) \rightarrow \pi^+\pi^-\Upsilon(1S)$ may result in a background to the signal because the charged pions can interact or decay within the detector to produce extra observed tracks. The details of the interaction of hadrons in the detector are not easily modelled and hence this background is not estimated via the Monte Carlo techniques described above. We do not expect the observed mass difference of those background events surviving all the cuts (including the requirement of two pizeros) to peak at the $\Upsilon(2S)$,$\Upsilon(1S)$ mass difference since the pions do not deposit their full energy in the detector. Instead, we expect these background events to have a spread of values of the mass difference ranging from below that of the $\pi^0\pi^0 l^+l^-$ signal region to higher values of ΔM. We therefore use the sideband estimate above to evaluate the contribution of this background to the signal. Since all other sources of background considered are small, we use the sideband estimate as a reasonable estimate of the total background contributing to the signal region.

4.2 Monte Carlo Studies

4.2.1 *Event Modelling*

To describe the model used to generate the Monte Carlo events we first introduce a number of quantities which characterize these events. We consider these transitions to be a type of two body decay $\Upsilon(2S) \rightarrow X + \Upsilon(1S)$ where $X \rightarrow \pi^0\pi^0$ and $\Upsilon(1S) \rightarrow l^+l^-$. Some variables we consider are:

- the mass of X (M_X), which has kinematic limits from $2M_{\pi^0}$ to ΔM, the mass difference,
- the orbital angular momentum (L) between X and the $\Upsilon(1S)$,
- the orbital angular momentum (ℓ) between the two pions from the X decay, which is equivalent to the spin of X since the pions have spin zero.

These quantities M_X, L, and ℓ affect the angular distributions of the final state particles and also the efficiency for observing these decays.

The model we use is the simplest configuration. We use a flat M_X distribution in order to determine the acceptance over the allowed kinematic range. We choose ℓ=L=0. The value L=0 conforms to previous studies of $\Upsilon(2S) \rightarrow \pi^+\pi^-\Upsilon(1S)$[6,7] and $\psi' \rightarrow \pi^+\pi^-\psi$[8] transitions. The choice of ℓ=0 is consistent with that found for $\psi' \rightarrow \pi^+\pi^-\psi$.[8] We will see that our resulting angular distributions are consistent with this hypothesis, lending validity to these assumptions. These choices yield isotropic distributions of the final state for the $\pi^0\pi^0$ system and its decay products.

Since no angular momentum is carried off by the $\pi^0\pi^0$ system, the $\Upsilon(1S)$ retains the polarization properties of the $\Upsilon(2S)$. The angular distribution used for modelling the decay $\Upsilon(1S) \rightarrow e^+e^-$ or $\mu^+\mu^-$ is: $1 + cos^2\theta + P_\perp^2 sin^2\theta cos2\phi$, i.e. that of a transversely polarized spin 1 object decaying into two spin $\frac{1}{2}$ objects. The angles θ, ϕ are measured in the $\Upsilon(1S)$ rest frame relative to axes which are parallel to those of lab frame. Here $P_\perp$ is the transverse beam polarization of Doris II. The transverse beam polarization on the $\Upsilon(2S)$ has been measured and found to be 70–80%.[9] All Monte Carlo results discussed here are obtained for $P_\perp$=70%. Results obtained from trials with $P_\perp$=80% are within the statistical errors of those obtained with the samples discussed here.

4.2.2 *Detector Simulation*

The simulation of the Crystal Ball detector is divided up into several parts. Electrons and photons are simulated by using the Electron Gamma Shower (EGS)

code.[10] The detailed geometry of the Crystal Ball detector is modelled in EGS, including the different crystal shapes, the material between the crystals themselves, the gap between the two hemispheres, and the stainless steel washer forming the base of each hemisphere. The endcap arrays are not modelled except for the deposition of spurious beam related energy (see below). The shower profiles and energy deposition of EGS have been well studied[11,12] and reproduce the attributes of electromagnetic showers well.

Muons in the Crystal Ball are reproduced in the Monte Carlo by adding the observed energies and energy distribution of real muons, observed in $e^+e^- \rightarrow \mu^+\mu^-$ events, to the Monte Carlo events. The resulting muon tracks reproduce those characteristics of real muons. The pattern selection efficiency and angular resolution are consistent with $e^+e^- \rightarrow \mu^+\mu^-$ events studied at the J/ψ. There are two difficulties with this simulation of muons, however. Firstly, this simulation does not account for the hemisphere gap which leads to an inefficiency in the detection of muons. Also, while most muons have the typical minimum ionizing behavior indicated earlier, some muons may knock electrons off of atoms in the NaI(Tℓ) and therefore create small showers which deposit additional energy in the detector. These muons may not be selected in the search for $e^+e^- \rightarrow \mu^+\mu^-$ and therefore will not be used in the Monte Carlo simulation. Because these factors are not taken into account completely when we add muons to the events, we overestimate the muon selection efficiency.

A correction for this selection problem is made by using another simulation of muons, called MUONEGS, where the muons are completely simulated in the detector. We then compare these new results with those obtained by using the real muons. This second simulation attempts to model the physical processes of a muon traveling through NaI(Tℓ).[13] These processes include ionization energy loss, multiple scattering and delta ray production. We find that for each event, the MUONEGS simulation indicates that there is an additional 3% inefficiency due to the effects not accounted for by adding the selected real muons to the Monte Carlo

data. For the final acceptance results, the efficiencies obtained by adding the real muons to the data are corrected by this value and we use 3% as the systematic error on the determination of the efficiency of the muon energy and pattern cut.

Once the events are passed through the detector itself, we simulate the effects of Doris II machine background. This is done using the Doris Bunch Marker (DBM) events taken during the $\Upsilon(2S)$ running period. We select a subsample of about 120,000 events which are randomly selected from runs according to the luminosity in each run. Runs with high luminosity have a proportionally higher number of DBM events in the luminosity weighted sample than those with low luminosity. For each Monte Carlo event in the sample, the energies from all the crystals in a DBM event chosen from the luminosity weighted sample are added to the Monte Carlo event energies already present. The effect is to overlay the beam related background with the Monte Carlo events.

The final step in the detector simulation procedure is the modelling of the triggers. This modelling is done by studying the trigger energy thresholds for each major and minor triangle. In addition, the total energy threshold for each trigger is studied. Each Monte Carlo event is checked to see whether it satisfies the requirements of any of the three triggers modelled. Those events which do not satisfy one of the three trigger requirements are rejected. A detailed report of these trigger threshold studies and efficiencies is presented elsewhere.[14] We find that for events fully contained in the fiducial volume of the detector, the efficiency for $\pi^0\pi^0e^+e^-$ events is essentially 100% and is greater than 97% for $\pi^0\pi^0\mu^+\mu^-$ events.

4.2.3 *Results of Acceptance Studies*

For acceptance studies, 5000 $\pi^0\pi^0e^+e^-$ and $\pi^0\pi^0\mu^+\mu^-$ Monte Carlo events are generated and simulated in the detector as described above. All cuts applied to the data are applied to the Monte Carlo data including the EOTAP selection discussed in Chapter 3. We note that the additional inefficiency, due to the EOTAP selection, for events which have been selected by the standard analysis and trigger cuts is

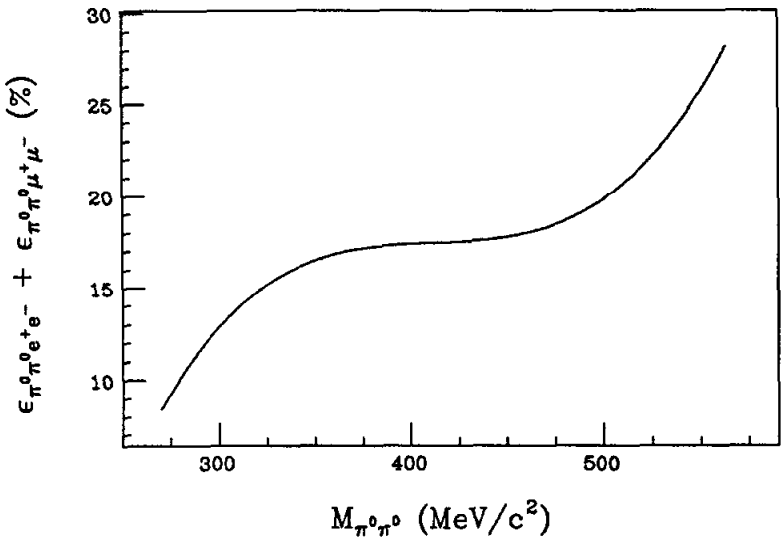

Fig. 4.12 Summed efficiency of the $\pi^0\pi^0e^+e^-$ and $\pi^0\pi^0\mu^+\mu^-$ decay modes vs $M_{\pi^0\pi^0}$.

about 2% for $\pi^0\pi^0\mu^+\mu^-$ events. This is due to a slightly stricter muon pattern cut in EOTAP than in the final analysis.[14] There is no additional inefficiency due to EOTAP in the $\pi^0\pi^0e^+e^-$ channel.

We find from our acceptance studies that our efficiency is highly dependent on the invariant mass $M_{\pi^0\pi^0}$ of the $\pi^0\pi^0$ system. Figure 4.12 is the summed acceptance of both the $\pi^0\pi^0e^+e^-$ and $\pi^0\pi^0\mu^+\mu^-$ decay modes versus the mass of the $\pi^0\pi^0$ system. The acceptance drops off as $M_{\pi^0\pi^0}$ approaches the lower kinematic limit. Figure 4.13 indicates why this is the case. For smaller values of $M_{\pi^0\pi^0}$ the velocity of the $\pi^0\pi^0$ system is higher, and the photons from the different pions will be boosted more forward and therefore will be more likely to overlap. This leads to a lower efficiency for the overlap cut.

4.2.4 *Systematic Effects*

A number of sources of systematic error on the event selection efficiency have been examined. Most studies consist of varying an individual cut around the value used in the analysis. The acceptance corrected number of events (i.e. the number

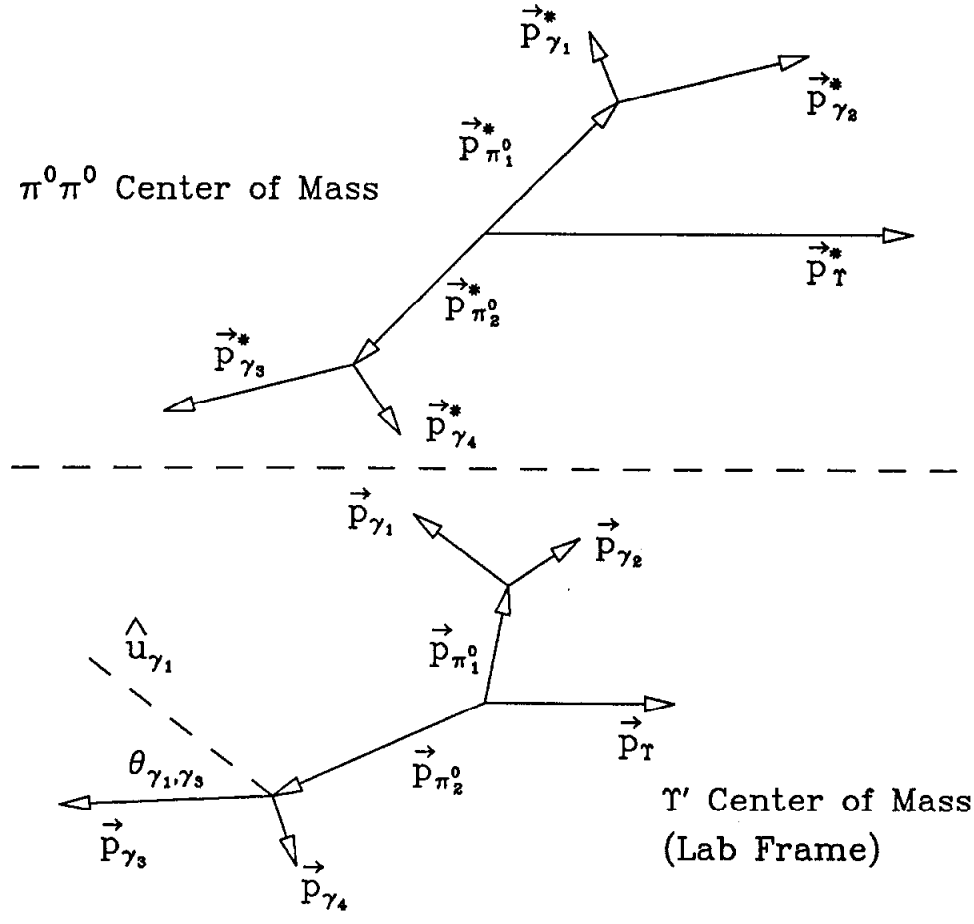

Fig. 4.13 Indication of the reason for a strong variation of detection efficiency over the $M_{\pi^0\pi^0}$ kinematic range. As $M_{\pi^0\pi^0}$ approaches the lower kinematic limit, the velocity of the $\pi^0\pi^0$ system increases. The angle $\theta_{\gamma_1,\gamma_3}$ becomes smaller for increasing $\beta_{\pi^0\pi^0}$. Because of this overlap between photons originating from different pions, the efficiency is reduced as $M_{\pi^0\pi^0}$ decreases.

of data events found, divided by the acceptance) is used as a measure of systematic effects. When a change in the acceptance corrected number of events outside of statistics occurs, that effect is considered systematic. The results of a given variation are averaged to determine the final systematic error quoted below. This method

of variation of the cuts allows one to check the simulation of the detector and the model as compared to the data. The systematic errors on the detection efficiency are listed in Table 4.3. The effects considered include:

- variations of the fiducial region of the detector (acceptance checks)
- changes of the overlap criteria for tracks
- increasing and decreasing the amount of excess energy allowed in the Ball for $\pi^0\pi^0\mu^+\mu^-$ events
- cuts in ϕ around the hemisphere gap to check the modelling of the gap in the Monte Carlo events
- variation of the confidence level cut for checking the fitting procedure
- variation of the cut made on $m_{\gamma\gamma}$ for selection of $\pi^{0\prime}s$
- check of the photon detection efficiency at low energies by varying the lower limit of track energies
- the uncertainty in the muon detection efficiency (as discussed in the section on the modelling of muons in the detector)

All errors were added in quadrature, resulting in systematic errors on the efficiency of 9% for $\epsilon_{\mu\mu\pi^0\pi^0}$ and 6% for $\epsilon_{ee\pi^0\pi^0}$.

4.3 Physics Results

4.3.1 $\pi^0\pi^0$ *Mass Distribution*

From the final event sample of 46 $\pi^0\pi^0e^+e^-$ events and 44 $\pi^0\pi^0\mu^+\mu^-$ events, we obtain the invariant $\pi^0\pi^0$ mass distribution shown as the histogram in Figure 4.14. The dashed curve in Figure 4.14 is the $\pi^0\pi^0$ mass distribution expected from phase space and corrected for acceptance. The confidence level for the agreement between the data and the phase space curve is less than 10^{-5}. Previous measurements of

Effect Examined	$\pi^0\pi^0 e^+e^-$ channel	$\pi^0\pi^0\mu^+\mu^-$ channel
Acceptance	no effect	5%
Overlap Cut	no effect	no effect
E_{excess}	N.A.	4%
Hemisphere Gap	no effect	no effect
Kinematic Fitting	2%	3%
π^0 Mass Cut	no effect	no effect
Low Energy γ Efficiency	6%	5%
Muon Selection Efficiency	N.A.	3%
Total Systematic Error	6%	9%

Table 4.3 Systematic errors in both the $\pi^0\pi^0 e^+e^-$ and $\pi^0\pi^0\mu^+\mu^-$ channel. The individual errors are added in quadrature to find the total systematic error.

$\Upsilon(2S) \rightarrow \pi\pi\Upsilon(1S)$[4,5,6,7,15] and $\psi' \rightarrow \pi\pi\psi$[8,16] have also indicated a peaked mass distribution.

To quantify this result, we fit the observed spectrum to three different theoretical expressions[17,18,19] folded with our experimental resolution of 8 MeV and the acceptance curve of Figure 4.12. The confidence level for all fits is greater than 79%. Within the drawing accuracy, all fits are represented by the solid curve in Figure 4.14. The functional form and value of the fitted parameter* of each model are listed in Table 4.4. We summarize all previous results for $\Upsilon(2S) \rightarrow \pi^+\pi^-\Upsilon(1S)$ in Table 4.5 for comparison. We find that this measurement for $\Upsilon(2S) \rightarrow \pi^0\pi^0\Upsilon(1S)$ is consistent with those made for $\Upsilon(2S) \rightarrow \pi^+\pi^-\Upsilon(1S)$.

* The effects of the uncertainty in the energy scale have been studied by varying the the ELOG correction. The systematic error on the parameters due to the energy scale uncertainty is small compared to the statistical error obtained from the fit.

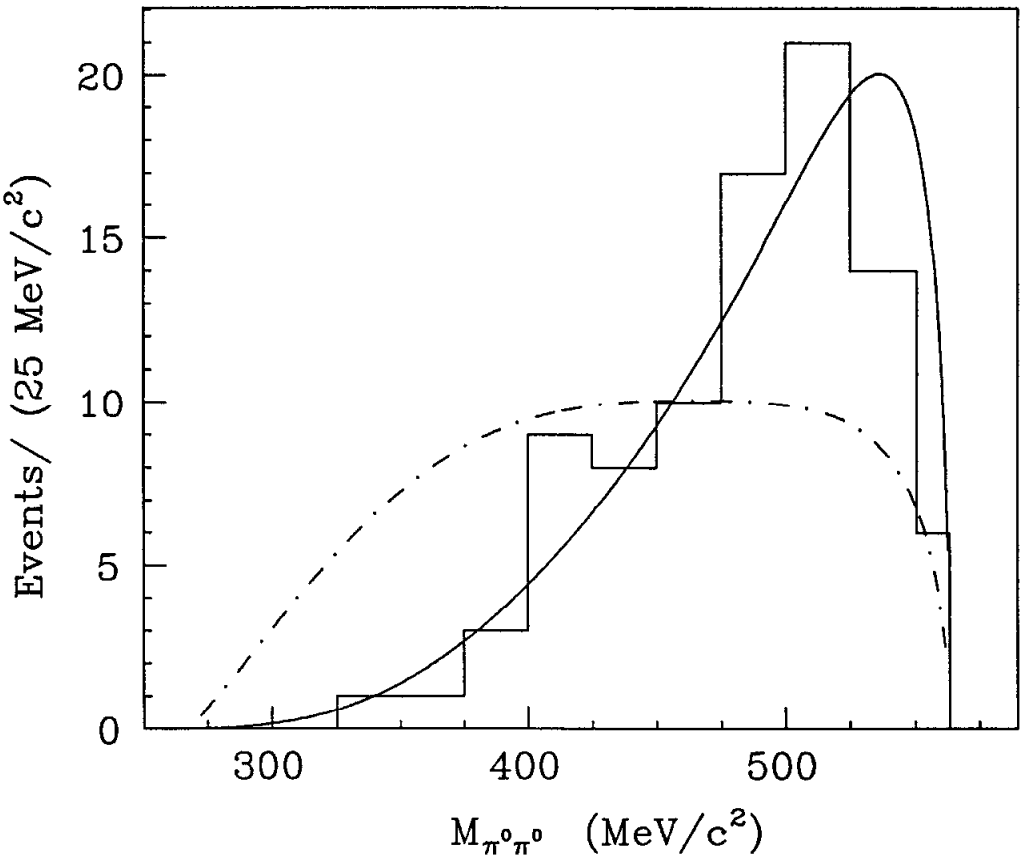

Fig. 4.14 The $M_{\pi^0\pi^0}$ distribution for the final data sample containing both $\pi^0\pi^0 e^+e^-$ and $\pi^0\pi^0\mu^+\mu^-$ events. The histogram is the data. The solid curve represents the fit to the data with the three theoretical expressions of Table 4.4 folded with our experimental resolution of 8 MeV and the acceptance curve of Figure 4.12. The dashed curve represents a phase space distribution folded with the acceptance. The confidence level for the agreement between the expectation from phase space and the data is less than 10^{-5}.

Model	Mass Distribution $\frac{dN}{dM_{\pi\pi}}$	Fit Result
Yan[a]	$\propto K\{(M^2_{\pi\pi}-2M^2_\pi)^2$ $+(\frac{B}{3A})(M^2_{\pi\pi}-2M^2_\pi)\,[(M^2_{\pi\pi}-4M^2_\pi)$ $+2(M^2_{\pi\pi}+2M^2_\pi)\frac{K_0^2}{M^2_{\pi\pi}}\,]+O(\frac{B^2}{A^2})\}$ $[K_0=(M^2_{\Upsilon'}+M^2_{\pi\pi}-M^2_\Upsilon)/(2M_{\Upsilon'})]$	$\frac{B}{A}=-0.18^{+0.18}_{-0.13}$
Voloshin–Zakharov[b]	$\propto K(M^2_{\pi\pi}-\lambda M^2_\pi)^2$	$\lambda = 3.3^{+1.0}_{-1.4}$
Novikov–Shifman[c]	$\propto K[M^2_{\pi\pi}-\kappa(M_{\Upsilon'}-M_\Upsilon)^2(1+2\frac{M^2_\pi}{M^2_{\pi\pi}})]^2$ $+O(\kappa^2)$	$\kappa = 0.14^{+0.05}_{-0.06}$

[a] References 17 and 20

[b] Reference 18

[c] Reference 19

where $K=[((M_{\Upsilon'}+M_\Upsilon)^2-M^2_{\pi\pi})((M_{\Upsilon'}-M_\Upsilon)^2-M^2_{\pi\pi})(M^2_{\pi\pi}-4M^2_\pi)]^{\frac{1}{2}}$ is the phase space factor.

Table 4.4 Functional form of fitting functions and results of fits to the $M_{\pi^0\pi^0}$ distribution

Fit Result for:	CLEO[a]	CUSB[b]	ARGUS[c]
B/A =	-0.18±0.06	-0.02±0.09	-0.09±0.07
λ =	3.2±0.4	not quoted	2.6±0.5
κ =	0.15±0.02	not quoted	0.12±0.02

[a] Reference 6

[b] Reference 7

[c] Reference 15

Table 4.5 Summary of results on $M_{\pi^+\pi^-}$ from previous experiments.

4.3.2 *Acceptance and Branching Ratio Results*

The mass distribution observed in these $\pi^0\pi^0 l^+l^-$ events is used to determine the acceptance corrected number of events. We have determined the acceptance as a function of mass as indicated in Figure 4.12. The acceptance corrected number of events is obtained by binning the data in $M_{\pi^0\pi^0}$ and correcting each bin for the efficiency averaged over that bin. We calculate average efficiencies from the number of observed events divided by the acceptance corrected number of events and obtain $\epsilon_{ee\pi^0\pi^0} = 0.10 \pm 0.01$ and $\epsilon_{\mu\mu\pi^0\pi^0} = 0.09 \pm 0.01$ where the errors are the statistical and systematic errors added in quadrature.

From the number of background subtracted events, the average detection efficiencies, and the number of $193 \pm 15 \times 10^3$ produced $\Upsilon(2S)$ decays (see Chapter 3), we obtain the following product branching ratios (the first error is statistical, the second systematic):

$$B(\Upsilon(2S) \to \pi^0\pi^0\Upsilon(1S)) \times B(\Upsilon(1S) \to e^+e^-) = (2.2 \pm 0.4 \pm 0.2) \times 10^{-3},$$

$$B(\Upsilon(2S) \to \pi^0\pi^0\Upsilon(1S)) \times B(\Upsilon(1S) \to \mu^+\mu^-) = (2.4 \pm 0.4 \pm 0.3) \times 10^{-3}.$$

Assuming lepton universality, we average the electron and muon results and find a product branching ratio of:

$$B(\Upsilon(2S) \to \pi^0\pi^0\Upsilon(1S)) \times B(\Upsilon(1S) \to l^+l^-) = (2.3 \pm 0.3 \pm 0.3) \times 10^{-3}.$$

Dividing out the present world average value[21] of the leptonic branching ratio $B_{ll}(\Upsilon(1S)) = 2.9 \pm 0.3\%$ we obtain $\mathrm{B}(\Upsilon(2S) \to \pi^0\pi^0\Upsilon(1S))= 8.0 \pm 1.5\%$ where the statistical and systematic errors are added in quadrature.

Our result is consistent with the recently published CUSB[7] value of $\mathrm{B}(\Upsilon(2S) \to \pi^0\pi^0\Upsilon(1S)) = (10.3 \pm 2.3)\%$. The present average value of the branching ratio $\mathrm{B}(\Upsilon(2S) \to \pi^+\pi^-\Upsilon(1S))$, derived from exclusive and inclusive measurements,[22]

is $(18.8 \pm 1.0)\%$. Using this value and our measurement for the $\pi^0\pi^0$ channel we obtain a ratio $\frac{\Gamma(\Upsilon(2S)\to\pi^0\pi^0\Upsilon(1S))}{\Gamma(\Upsilon(2S)\to\pi^+\pi^-\Upsilon(1S))} = 0.43 \pm 0.07$. Taking into account phase space we expect this ratio to be 0.53 for an $I = 0$ isospin assignment of the $\pi\pi$ system, which is required if isospin is conserved. Our result agrees with this expectation with a confidence level of 11%.

4.3.3 *Angular Distributions*

The angular distributions of the $\pi^0\pi^0$ system and its decay products give information about the orbital angular momentum between the $\pi^0\pi^0$ system and the $\Upsilon(1S)$ (denoted L) and the spin of the $\pi^0\pi^0$ system (denoted ℓ). Information about L and ℓ is obtained by examining the distributions of $\cos\theta_{\pi^0\pi^0}$, $\phi_{\pi^0\pi^0}$, $\cos\theta^*_{\pi^0}$, and $\phi^*_{\pi^0}$. These angles are defined in Figure 4.15. The angles $\theta_{\pi^0\pi^0}$,$\phi_{\pi^0\pi^0}$ are the polar and azimuthal angles of the $\pi^0\pi^0$ momentum vector in the laboratory frame. The angles $\theta^*_{\pi^0}$,$\phi^*_{\pi^0}$ are the polar and azimuthal angles of a π^0 in the center of mass frame of the $\pi^0\pi^0$ system. The axes of this coordinate system coincide with those of the lab frame. This frame results from a pure boost (without rotation) in the direction of the $\pi^0\pi^0$ momentum vector into its center of mass.

The maximum information on L and ℓ would be obtained by looking at $\theta_{\pi^0\pi^0}$, $\phi_{\pi^0\pi^0}$, $\theta^*_{\pi^0}$, $\phi^*_{\pi^0}$ without integration over any of the variables.[23] Due to the low statistics of our event sample, we are unable to examine correlations of these variables. Instead we examine the distributions individually. We note that in several previous analyses[6,7] the pion angular distribution in the di-pion rest frame has been studied in the helicity frame. If the di-pion system is emitted in an S–wave, it can be shown (see Appendix C) that $\frac{dN}{dcos\theta^{hel}_{\pi}} = const$, regardless of the spin of the $\pi\pi$ system. Thus the distribution of $cos\theta^{hel}_{\pi}$ cannot analyze the spin of the di-pion system if the latter results from an S–wave decay of the $\Upsilon(2S)$.

We plot in Figure 4.16a the $\cos\theta_{\pi^0\pi^0}$ distribution and in Figure 4.16b we plot the $\phi_{\pi^0\pi^0}$ distribution for all events. Figure 4.17 is the data in the $\pi^0\pi^0$ rest frame coordinates. Figure 4.17a is the $\cos\theta^*_{\pi^0}$ distribution and Figure 4.17b is for $\phi^*_{\pi^0}$.

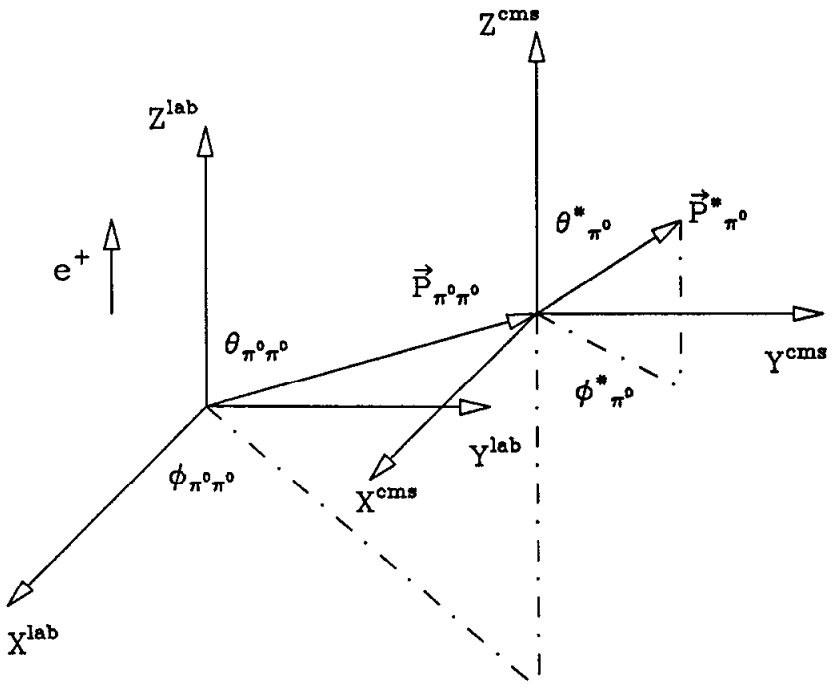

Fig. 4.15 Definitions of the two coordinate systems $\theta_{\pi^0\pi^0}$,$\phi_{\pi^0\pi^0}$ and $\theta^*_{\pi^0}$,$\phi^*_{\pi^0}$ used for the presentation of the angular distributions. The angles $\theta_{\pi^0\pi^0}$,$\phi_{\pi^0\pi^0}$ are the polar and azimuthal angles of the $\pi^0\pi^0$ momentum vector in the laboratory frame. The angles $\theta^*_{\pi^0}$,$\phi^*_{\pi^0}$ are polar and azimuthal angles of a π^0 in the center of mass frame of the $\pi^0\pi^0$ system. The axes of this coordinate system coincide with those of the lab frame. This frame results from a pure boost (without rotation) in the direction of the $\pi^0\pi^0$ momentum vector into its center of mass.

In each figure the histogram is the data and the solid line is the Monte Carlo prediction which is calculated using our measured $M_{\pi^0\pi^0}$ distribution and using isotropic decay distributions as expected for a di-pion system of spin zero emitted in an S-wave (L=ℓ=0). The data for $\phi_{\pi^0\pi^0}$, $\cos\theta^*_{\pi^0}$, and $\phi^*_{\pi^0}$ are in good agreement with isotropy. For the distribution of $\cos\theta_{\pi^0\pi^0}$, the confidence level of the agreement between the data and the prediction from isotropy is only 3%. This low confidence level is due to the high number of counts at $\cos\theta_{\pi^0\pi^0} = -0.5$. We have looked for and have found no systematic effect which can explain this. Since such a one bin effect is not likely to be a physics effect, we believe that this high bin is due to a

statistical fluctuation and that this distribution is consistent with isotropy. These results are consistent with the expectation for a spin zero assignment for the dipion system emitted in a relative S wave.* These results are also consistent with the previous measurements of isotropic decay distributions in the decays $\Upsilon(2S) \rightarrow \pi^+\pi^-\Upsilon(1S)$[6,7] and $\psi' \rightarrow \pi^+\pi^-\psi$.[8]

* The limited statistical precision of our measurement only allows us to demonstrate consistency with isotropy and does not allow us to rule out nonzero values of ℓ and L.

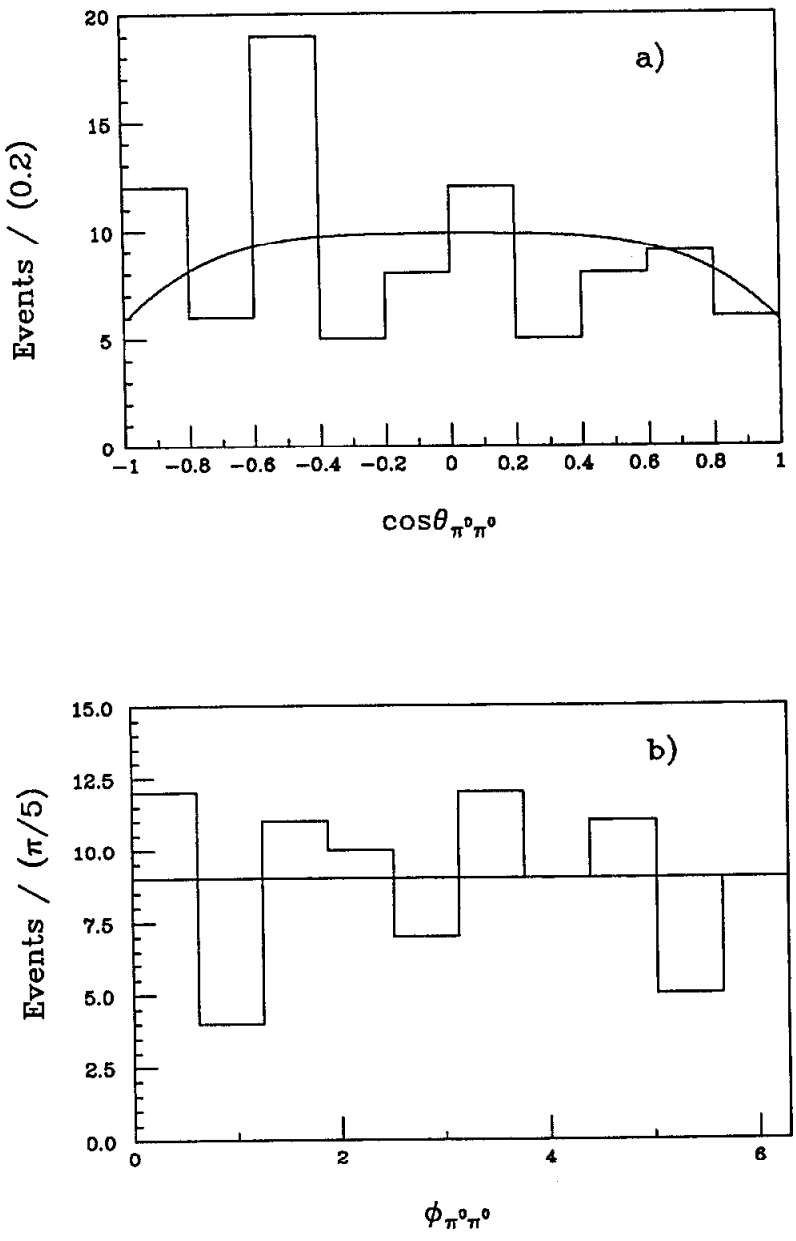

Fig. 4.16 Angular distributions of the $\pi^0\pi^0 l^+l^-$ events in the lab coordinate system. a) The $\cos\theta_{\pi^0\pi^0}$ distribution. b) The $\phi_{\pi^0\pi^0}$ distribution. The curves represent the expectation for an S–wave decay of the $\Upsilon(2S)$ and a spin zero di-pion system.

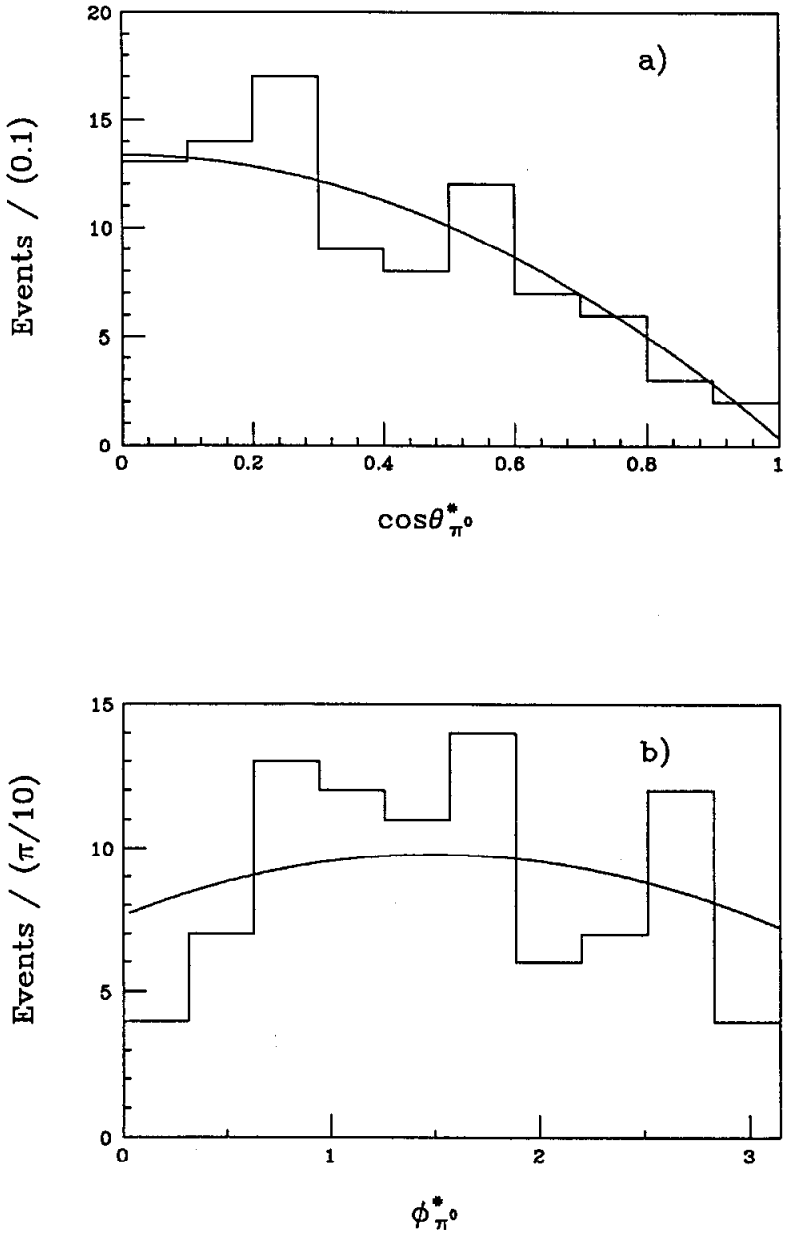

Fig. 4.17 Angular distributions of the $\pi^0\pi^0 l^+l^-$ events in the $\pi^0\pi^0$ center of mass. a) The $\cos\theta^*_{\pi^0}$ distribution. b) The $\phi^*_{\pi^0}$ distribution. The curves represent the expectation for an S–wave decay of the $\Upsilon(2S)$ and a spin zero di-pion system.

References

1) The $e^+e^- \rightarrow \mu^+\mu^-$ annihilation events were provided by Duncan Prindle. For more information regarding these data see D. Prindle, Ph. D. thesis, Carnegie–Mellon University, 1985 (unpublished).

2) J. Gaiser, Ph. D. thesis, Stanford University, 1982, and SLAC Report 255 (unpublished).

3) Particle Data Group, *Rev. Mod. Phys.* **56** (1984) No. 2, Part II.

4) G. Mageras *et al.*, *Phys. Rev. Lett.* **46** (1981) 1115.

5) J. Mueller *et al.*, *Phys. Rev. Lett.* **46** (1981) 1181.

6) D. Besson *et al.*, *Phys. Rev.* **D30** (1984) 1433.

7) V. Fonseca *et al.*, *Nucl. Phys.* **B242** (1984) 31.

8) G. Abrams, Properties of the New Particles $\psi(3095)$ and $\psi'(3684)$, Proc. of the 1975 Int. Symp. on Lepton and Photon Interaction at High Energies, Ed. W.T. Kirk, (Stanford University, Stanford, 1975).

9) D. P. Barber *et al.*, *Phys. Lett.* **135B** (1984) 498.

10) R.L. Ford and W.R. Nelson, Stanford Linear Accelerator Center report, SLAC-0210 (1978).

11) R. Partridge, Ph. D. thesis, California Institute of Technology, 1984, (unpublished).

12) R. Lee, Ph. D. thesis, Stanford University, 1985, and SLAC Report 282 (unpublished).

13) D. Prindle, Ph. D. thesis, Carnegie–Mellon University, 1985 (unpublished).

14) D. Gelphman and W. Walk, Crystal Ball note 260, 1984.

15) H. Albrecht *et al.*, *Phys. Lett.* **134B** (1984) 137.

16) M. Oreglia *et al.*, *Phys. Rev. Lett.* **45** (1980) 959.

17) T.M. Yan, *Phys. Rev.* **D22** (1980) 1652.
Y.P. Kuang and T.M. Yan, *Phys. Rev.* **D24** (1981) 2874.

18) M. Voloshin and V. Zakharov, *Phys. Rev. Lett.* **45** (1980) 688.

19) V.A. Novikov and M.A. Shifman, *Z. Phys.* **C8** (1981) 43.

20) The form given is derived from a formula in Ref. 17 and explicitly quoted in Ref. 6, 7.

21) The average value of $B_{\ell\ell}(\Upsilon(1S))$ is calculated assuming lepton universality and excluding values derived from measurements of hadronic cascade transitions. The value of $B_{\ell\ell}(\Upsilon(1S))$ for each measurement is listed after each reference. Ch. Berger *et al.*, *Z. Phys.* **C1** (1979) 343 ($2.2 \pm 2.0\%$); Ch. Berger *et al.*, *Phys. Lett.* **93B** (1980) 497 ($5.1 \pm 3.0\%$); H. Albrecht *et al.*, *Phys. Lett.* **93B** (1980) 500 ($2.9 \pm 1.3 \pm 0.5\%$); B. Niczyporuk *et al.*, *Phys. Rev. Lett.* **46** (1981) 92 ($3.5 \pm 1.4 \pm 0.4\%$); D. Andrews *et al.*, *Phys. Rev. Lett.* **50** (1983) 807 ($2.7 \pm 0.3 \pm 0.3\%$); R. Giles *et al.*, *Phys. Rev. Lett.* **50** (1983) 877 ($3.4 \pm 0.4 \pm 0.4\%$); The CUSB measurement is taken from: P.M. Tuts, Experimental Results in Heavy Quarkonia, Proc. of the 1983 Int. Symp. on Lepton and Photon Interaction at High Energies, Eds. D.G. Cassel and D.L. Kreinick, (Cornell, Ithaca, 1983) ($2.7 \pm 0.3 \pm 0.3\%$).

22) To calculate the average value of $B(\Upsilon(2S) \to \pi^+\pi^-\Upsilon(1S))$ we have used the exclusive measurements by LENA ($0.61 \pm 0.21\%$), see B. Niczyporuk *et al.*, *Phys. Lett.* **100B** (1981) 95; CUSB $(0.63 \pm 0.13 \pm 0.10\%)$[4], ($0.56 \pm 0.04 \pm 0.05\%$ for $\pi^+\pi^-e^+e^-$ and $0.52 \pm 0.04 \pm 0.04\%$ for $\pi^+\pi^-\mu^+\mu^-$)[7]; CLEO $(0.74 \pm 0.18\%)$[5], ($0.53 \pm 0.05\%$ for $\pi^+\pi^-e^+e^-$ and $0.55 \pm 0.05\%$ for $\pi^+\pi^-\mu^+\mu^-$)[6]; and ARGUS $(0.50 \pm 0.06\%)$[15] and $B_{\ell\ell}(\Upsilon(1S)) = (2.9 \pm 0.3)\%$. The LENA and ARGUS results are derived from numbers quoted in their publications. The results of the inclusive measurements are taken from ARGUS $(17.9 \pm 0.9 \pm 2.1\%)$[15] and CLEO$(19.1 \pm 3.1 \pm 2.9\%)$[5], $(19.1 \pm 1.2 \pm 0.6\%)$[6].

23) R. Cahn, *Phys. Rev.* **D12** (1975) 3559.

Chapter 5

Conclusions

We have measured the decays $\Upsilon(2S) \rightarrow \pi^0\pi^0\Upsilon(1S)$ where the $\Upsilon(1S)$ decays into e^+e^- or $\mu^+\mu^-$ and find a product branching ratio $B(\Upsilon(2S) \rightarrow \pi^0\pi^0\Upsilon(1S))$ $\times B_{\ell\ell}(\Upsilon(1S))=(2.3\pm0.3\pm0.3)\times10^{-3}$ where the first error is statistical and the second is systematic. We find that our measurement of this decay is in good agreement with the previous measurement by CUSB.[1] Our measured branching ratio $B(\Upsilon(2S) \rightarrow \pi^0\pi^0\Upsilon(1S))=(8.0\pm1.5\%)$ agrees well with the CUSB result, and the mass spectrum and those angular distributions which can be compared are in qualitative agreement.

When comparisons are made to the $\pi^+\pi^-$ transitions, we find our results are in substantial agreement with those expected for an isospin zero di–pion system. The $\pi^0\pi^0$ mass spectrum shows quantitative agreement with that measured for $\Upsilon(2S) \rightarrow \pi^+\pi^-\Upsilon(1S)$ transitions.[1,2,3] Measurements of the angular distributions of the di–pion system and its decay products for both the charged[1,3,4] and neutral $\pi\pi$ transitions agree with the expectation of a spin zero $\pi\pi$ system emitted in an S–wave. The ratio of the partial widths for the two decays is in reasonable agreement with that expected for a $\pi\pi$ system with I=0.

The theoretical framework provides a prediction for the ratio of rates for the hadronic transitions $\Upsilon(2S) \rightarrow \pi\pi\Upsilon(1S)$ and $\psi' \rightarrow \pi\pi\psi$. We compare the partial width $\Gamma(\psi' \rightarrow \pi^0\pi^0\psi)$ and $\Gamma(\Upsilon(2S) \rightarrow \pi^0\pi^0\Upsilon(1S))$ by using our measured branching fraction $\mathrm{Br}(\Upsilon(2S) \rightarrow \pi^0\pi^0\Upsilon(1S))$ and the world average values:[5] $\mathrm{Br}(\psi' \rightarrow$

$\pi^0\pi^0\psi) = 17 \pm 2\%$, $\Gamma(\psi' \rightarrow all) = 215 \pm 40$ keV, $\Gamma(\Upsilon(2S) \rightarrow all) = 29.6 \pm 4.7$ keV. We calculate the ratio of partial widths:

$$\frac{\Gamma(\psi' \rightarrow \pi^0\pi^0\psi)}{\Gamma(\Upsilon(2S) \rightarrow \pi^0\pi^0\Upsilon(1S))} = 15 \pm 5$$

This is in good agreement with the expectation of $\simeq$16 based on the scaling laws derived from the multipole expansion assuming the radiation of two spin 1 gluons. For the emission of two spin 0 gluons, the multipole expansion predicts the ratio of partial widths to be $\simeq$1.[6] Within the framework of this model, the data disagree with the prediction based on a scalar gluon at a level of 3 standard deviations.

The comparison of the experimental results for the mass spectrum and the angular distributions of the $\pi^0\pi^0$ system shows reasonable agreement with the theoretical model. While this experiment does not provide the statistical precision necessary to rule out spin assignments other than zero for the di–pion system, we find the data to be consistent with that hypothesis. For the case of a spin zero $\pi\pi$ system emitted in an S–wave, the use of PCAC and current algebra[7] predicts that the mass of the $\pi\pi$ system should be peaked as $(phase\ space) \times (M^2_{\pi\pi} - \lambda m^2_\pi)^2$ with $\lambda = 2$. We have measured $\lambda = 3.3^{+1.0}_{-1.4}$ for the $\pi^0\pi^0$ transitions which, within the large errors, agrees with the expectation $\lambda = 2$.

The work on $\Upsilon(2S) \rightarrow \pi^0\pi^0\Upsilon(1S)$ presented in this thesis adds to the experimental picture of these hadronic transitions. Higher statistics measurements of these $\Upsilon(2S) \rightarrow \pi\pi\Upsilon(1S)$ transitions are necessary to make more precise measurements of the mass distribution and the angular distributions of the di–pion system. New experimental results focussed on the transitions from the $\Upsilon(3S)$ will be of interest since the current small data samples available indicate considerable differences in the mass spectrum compared to the $\Upsilon(2S)$ transitions which are not accounted for by the theory. Additionally, no information exists on the angular distributions resulting from these decays. More quantitative studies will allow the theoretical understanding of these processes to improve.

References

1) V. Fonseca *et al.*, *Nucl. Phys.* **B242** (1984) 31.

2) H. Albrecht *et al.*, *Phys. Lett.* **134B** (1984) 137.

3) D. Besson *et al.*, *Phys. Rev.* **D30** (1984) 1433.

4) Contributed paper to 1983 Int. Symp. on Lepton and Photon Interaction at High Energies, Cornell University, August 1983.
ARGUS Collaboration, H. Albrecht *et al.*, DESY preprint number ARGUS 83–01.

5) Particle Data Group, *Rev. Mod. Phys.* **56** (1984) No. 2, Part II.

6) T. M. Yan, *Phys. Rev.* **D22** (1980) 1652.

7) L. S. Brown and R. N. Cahn, *Phys. Rev. Lett.* **35** (1975) 1.

Appendix A

Energy Scale Corrections

In this appendix we discuss the need for and the method for correcting the energy measurements beyond those provided by the standard Σ_{13}. In addition we present an example of the application of these corrections to the low energy photon spectra resulting from the decays of the type $\Upsilon(2S) \rightarrow \gamma\chi_b \rightarrow \gamma\gamma\Upsilon(1S) \rightarrow \gamma\gamma l^+l^-$.

A.1 Evidence for Energy Scale Shifts

There is substantial evidence for systematic shifts in the energy scale of low energy photons (10–450 MeV) provided in both inclusive[1] and exclusive channels. Here we discuss two exclusive channels:

$$\Upsilon(2S) \rightarrow \pi^0\pi^0\Upsilon(1S) \rightarrow \gamma\gamma\gamma\gamma l^+l^- \tag{1}$$

$$\Upsilon(2S) \rightarrow \gamma\chi_b \rightarrow \gamma\gamma\Upsilon(1S) \rightarrow \gamma\gamma l^+l^- \tag{2}$$

For reaction (1) we find that measurements of the π^0 mass and the mass difference $\Delta M = \mathrm{M}(\Upsilon(2S)) - M_{recoil}$ calculated from the four photons are shifted to lower energy than the nominal values[2] when the standard Σ_{13} energies are used. Figure A.1 is a plot of all $\gamma\gamma$ masses formed from the six $\gamma\gamma$ pairings for each $\pi^0\pi^0$ candidate which has passed the kinematic fit and all previous cuts (see Chapter 4 for the details of these cuts). The energies of the photons have <u>not</u> been corrected

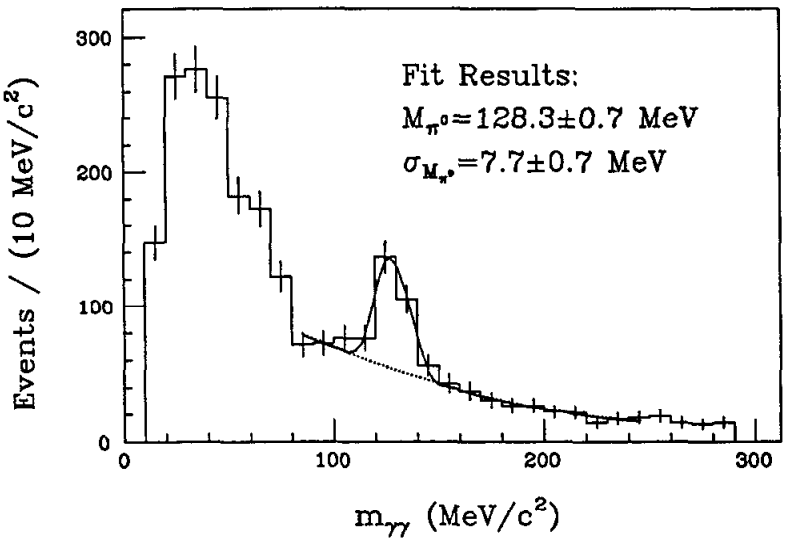

Fig. A.1 Plot of all uncorrected masses $m_{\gamma\gamma}$ for $\pi^0\pi^0 l^+l^-$ candidate events passing the confidence level cut. The curve indicates a fit to a single Gaussian of variable mean and width on top of a quadratic background.

using the ELOG corrections discussed in Chapter 3 but rather only the standard Σ_{13} has been used.* In this appendix, the term *uncorrected* refers to the standard Σ_{13} energy measurement. Figure A.1 includes both $\pi^0\pi^0 e^+e^-$ and $\pi^0\pi^0\mu^+\mu^-$ events. To find the measured π^0 mass before energy corrections we fit Figure A.1 for $m_{\gamma\gamma}$ between 80 MeV/c^2 and 250 MeV/c^2 to a single Gaussian with a quadratic background. The 80 MeV/c^2 cutoff is made to avoid the radiative Bhabha background (discussed in Chapter 4) which cannot be smoothly joined to the background at masses 80 MeV/c^2 and higher. The result of the fit, shown as the curve in Figure A.1, is a Gaussian of mean 128.3 ± 0.7 MeV/c^2 and width 7.7 ± 0.7 MeV/c^2. While the width is consistent with that expected for low energy π^0's in our detector, the mass is about 5% below the 135 MeV/c^2 accepted for the π^0 mass.[2]

We select events with a combination of photons $m_{\gamma_1\gamma_2}, m_{\gamma_3\gamma_4}$ with both masses

* We note that the standard Σ_{13} includes both the PCORR correction and the correction for leakage outside the group of thirteen crystals discussed in Chapter 3.

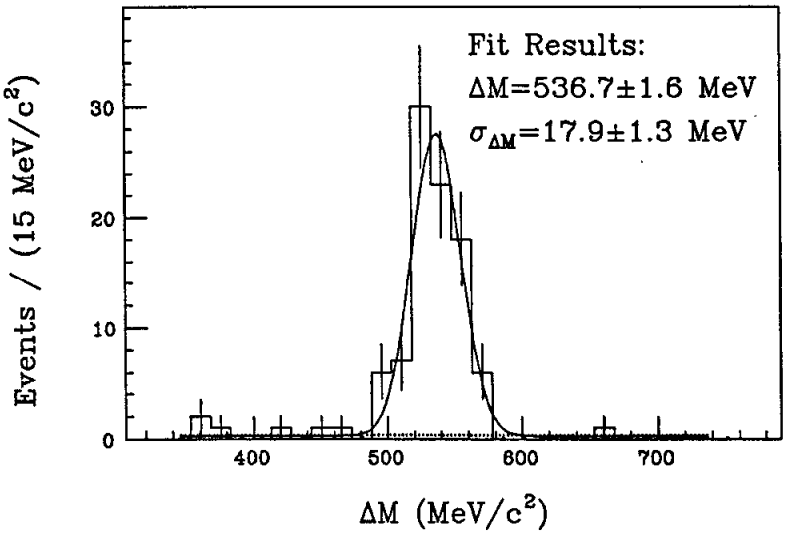

Fig. A.2 Mass difference plot for $\Upsilon(2S) \rightarrow \pi^0\pi^0\Upsilon(1S)$ events using uncorrected energies. The curve indicates a fit to the data with a single Gaussian of variable width and mean on top of a flat background.

within ± 22 MeV/c^2 of our measured π^0 mass of 128 MeV/c^2. We plot in Figure A.2 the mass difference ΔM for all events surviving this modified π^0 mass cut. The overlaid curve is a fit to a single Gaussian and a flat background. The fit result is $\Delta M = 536.7 \pm 1.6$ MeV/c^2 with $\sigma_{\Delta M} = 17.9 \pm 1.3$ MeV/c^2. Again the width is consistent with the Monte Carlo expectations based on energy and angular resolution, but the mass difference is about 5% below the nominal value. For channel (1) we find both ΔM and m_{π^0} to be about 5% below their nominal values.

For the $\gamma\gamma$ transitions of channel (2) we have applied essentially the same cuts as those for channel (1) except we require exactly two photon candidates per event and place a lower limit of 50 MeV on E_γ. In Figure A.3 we plot the mass difference as calculated from the two photons. Again we expect this distribution to peak at 563.3 MeV/c^2, corresponding to transitions from the $\Upsilon(2S)$ to the $\Upsilon(1S)$. The curve in Figure A.3 indicates the fit obtained with a single Gaussian on a flat background over the region indicated in the plot. We find $\Delta M = 541.6 \pm 2.7$, again lower than expected for an accurate energy scale.

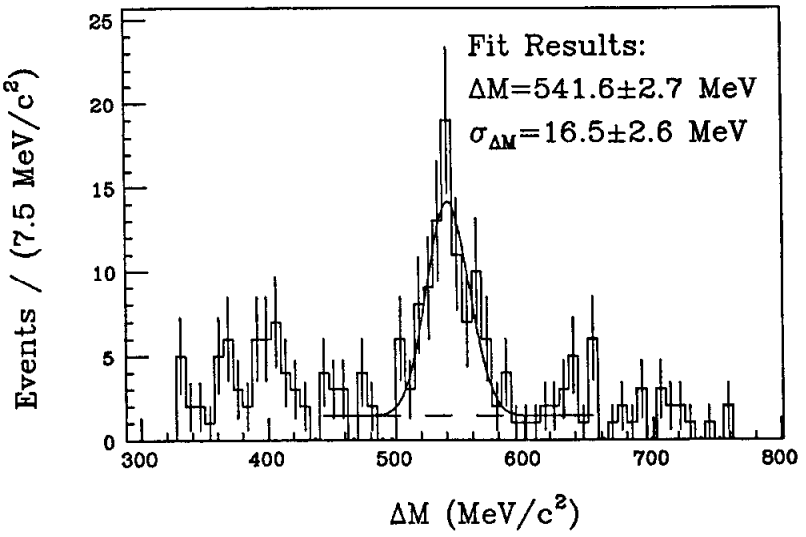

Fig. A.3 Plot of the mass difference ΔM calculated for $\Upsilon(2S) \rightarrow \gamma\gamma\Upsilon(1S)$ decays. The curve is a fit of a single Gaussian plus a flat background over the region indicated.

Here we have distinct measurements in two channels which indicate that our energy scale is low for photons in this energy range. Figure A.4a is the spectrum of photons for $\pi^0\pi^0$ events with $\Delta M = 537 \pm 60$ MeV/c^2. Figure A.4b is the spectrum of photons for $\gamma\gamma l^+l^-$events with $\Delta M = 542 \pm 45$ MeV/c^2. We see that the photons used in these measurements cover the energy region from about 10 MeV to about 450 MeV.

A.2 Methods of Correcting Energy Scale Shifts

One possible way to explain these results is to postulate that every photon in the energy range covered by these two channels is measured low by a fixed amount independent of the true photon energy. We note that since ΔM is approximately $\sum_{i=1}^{n_\gamma} E_{\gamma_i}$, then we would expect the deviation of the mass difference for $\gamma\gamma\gamma\gamma l^+l^-$ events from the true mass difference to be roughly twice the deviation for $\gamma\gamma l^+l^-$ events. Instead we note that the deviation is about the same. This indicates that the energy shift must have some kind of energy dependence.

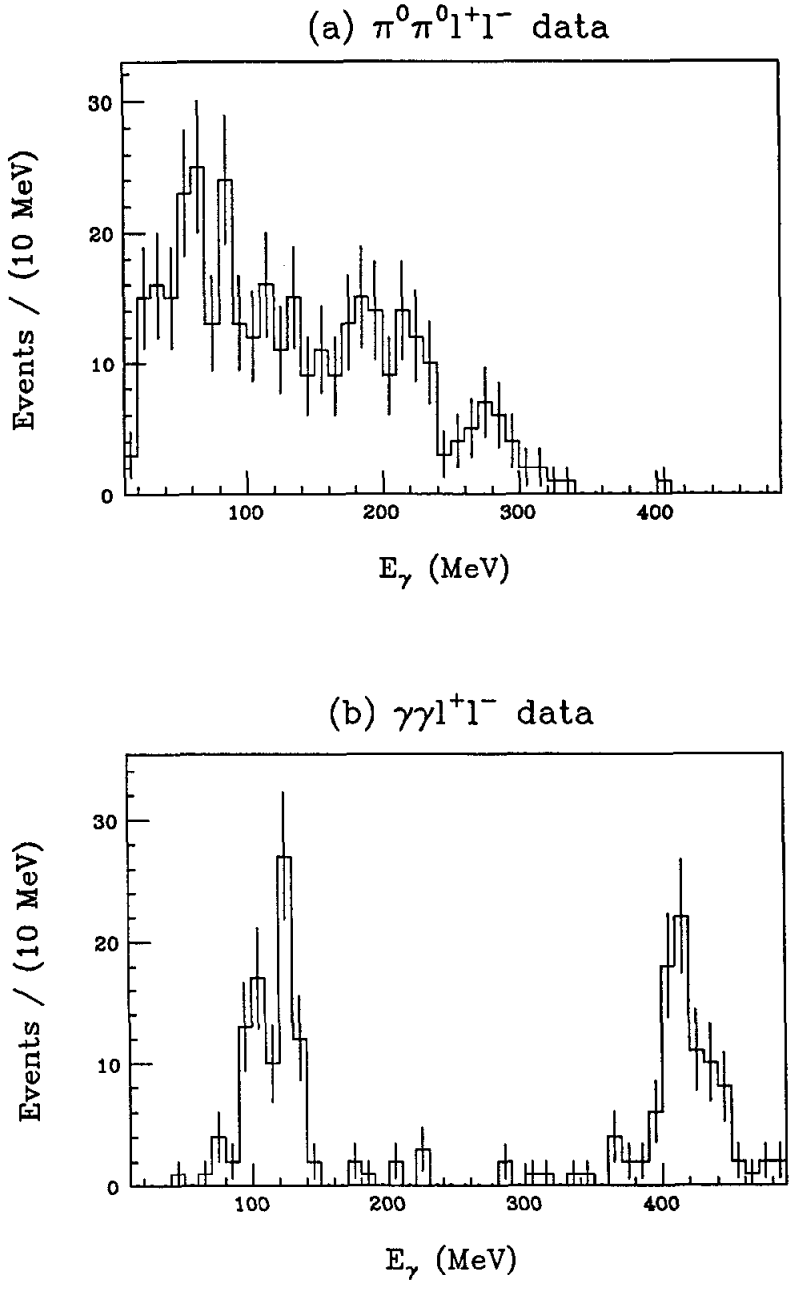

Fig. A.4 Photon energy spectrum for a) $\pi^0\pi^0 l^+l^-$ event candidates and b) $\gamma\gamma l^+l^-$ event candidates.

We discuss here two different types of energy corrections which have been made in an attempt to solve the energy scale problem. The first is a simple correction which assumes that the error in the energy measurement, ΔE, is proportional to the incident energy. That is:

$$\Delta E = \alpha_{linear}\, E_{true}$$
$$E_{true} = E_{meas} + \alpha_{linear}\, E_{true}$$

since $E_{true} \approx E_{meas}$,

$$E_{true} \approx E_{meas}(1 + \alpha_{linear})$$

This correction has the difficulty that at the beam energy the correction does not disappear. Since the beam energy is the calibration point for the data we should expect all corrections to vanish at $E_\gamma \sim 5000$ MeV.

The correction we use for the final results of Chapter 4 provides a more sensible behavior as the observed energy increases. We choose a logarithmic form:

$$E_{true} = \frac{E_{meas}}{1 + \alpha_{log} \ln \frac{E_{meas}}{E_{beam}}}$$

This form has the virtue that the corrections to observed energies near the Bhabha calibration point are small and grow slowly as the observed energy decreases. We use the logarithmic form as an *ad hoc* correction and below present a model as one possible motivation for choosing such a form.

Our model explaining the systematic lowering of the energy scale assumes that the amount of unmeasured energy of a given photon is not only proportional to the incident true energy of the photon, but also to the radial distance of the shower maximum within a crystal from that of the Bhabha calibration point. The position of the shower maximum provides a first order parameterization of the development of electromagnetic showers in NaI(Tℓ). We assume that there is some attenuation in the crystal such that the amount of light which does not reach the phototube

(and hence is not counted as measured energy) is proportional to the distance from the calibration point. This has the desirable feature of vanishing at the calibration point. Investigations into the electronics have found no significant deviations from linearity[3] and make it reasonable to assume that a mechanism within the crystals is responsible for the deviations of our energy measurements from the linearity assumed by our calibration procedure.

The form of this correction is derived as follows:

$$\Delta E \equiv E_{true} - E_{measured}$$

assume:

$$\Delta E = \kappa E_{true} \Delta d$$

where κ is a constant and Δd is the distance of the shower maximum from the calibration point at E_{beam}.

$$\Delta d = d_{calib} - d_{true}$$

where

$$d_i = a \ln E_i + b$$

for electromagnetic showers in NaI(Tℓ) where a and b are constants.[2,4] Substituting for d_{calib} and d_{true} we find:

$$\begin{aligned} \Delta d &= a\left(\ln E_{beam} - \ln E_{true}\right) \\ &= -a \ln \frac{E_{true}}{E_{beam}} \end{aligned}$$

Therefore:

$$\Delta E = -a\kappa E_{true} \ln \frac{E_{true}}{E_{beam}}$$

and:

$$\begin{aligned} E_{true} &= E_{meas} + \Delta E \\ &= E_{meas} - a\kappa E_{true} \ln \frac{E_{true}}{E_{beam}} \end{aligned}$$

Solving for E_{true} and assuming $E_{true} \approx E_{meas}$ we find:

$$E_{true} = \frac{E_{meas}}{1 + \alpha_{log} \ln \frac{E_{meas}}{E_{beam}}} \qquad \alpha_{log} \equiv a\kappa$$

This is the form used for the ELOG energy corrections as discussed in Chapter 3.

A.3 Determination of α_{log} and α_{linear}

The energy correction constants are determined empirically from the $\pi^0\pi^0 l^+l^-$ events and are checked by applying the corrections to the $\gamma\gamma l^+l^-$ data. The $\pi^0\pi^0 l^+l^-$ events are selected by the standard analysis of Chapter 4 but with a M_{π^0} cut of 128 ± 22 MeV/c^2 and a ΔM cut of 538 ± 45 MeV/c^2 where all the energies used for these quantities are uncorrected. For the remaining events we form the sum:

$$\chi^2 = \sum_{i}^{N_{events}} \left(\frac{\Delta M_i(\alpha) - 563.3}{\sigma_{\Delta M}} \right)^2$$

Here $\Delta M_i(\alpha)$ is a function of α_{linear} (or α_{log}) and is dependent on the correction constant to be determined. The best value of α is determined by minimizing this χ^2 sum. Through this technique, we tune the value of the correction by forcing the centroid of the mass distribution to the nominal value. We find $\alpha_{linear} = 0.0492 \pm 0.0035$ and $\alpha_{log} = 0.0137 \pm 0.0009$. The errors on the parameters indicate the statistical error on the mass difference due to the limited number of events in the sum.

We can also determine these parameters by forcing the π^0 mass to the accepted value. The π^0 mass and the mass difference ΔM are not completely independent,

but this is a good check of our technique. When we force M_{π^0} to its nominal value we find $\alpha_{linear} = .0556 \pm .0053$ and $\alpha_{log} = .0137 \pm .0012$.

We check these results by applying the different corrections to the photons in the $\Upsilon(2S) \rightarrow \gamma\chi_b \rightarrow \gamma\gamma\Upsilon(1S) \rightarrow \gamma\gamma l^+l^-$ decays described above. Figure A.5a is the mass difference for the $\gamma\gamma l^+l^-$ events with the linear corrections applied using $\alpha_{linear} = 0.0492$ determined from the mass difference in $\pi^0\pi^0 l^+l^-$ events. The fitted curve is a Gaussian with a flat background and gives a corrected mass difference of $\Delta M = 569.2 \pm 2.4$ MeV. Using the value $\alpha_{linear} = 0.0556$ determined from fixing the π^0 mass, we find $\Delta M = 575.2 \pm 2.3$ MeV. Figure A.5b is the mass difference for the $\gamma\gamma l^+l^-$ events with the logarithmic correction applied using $\alpha_{log} = 0.0137$. A fit with a single Gaussian on a flat background gives $\Delta M = 564.2 \pm 2.7$ MeV, in agreement with the true mass difference of 563.3 MeV.[2] The success of the logarithmic correction in both the $\pi^0\pi^0$ and $\gamma\gamma$ transitions discussed here is encouraging. The two different channels have quite different photon spectra (see Figure A.4) and are two independent channels. The linear correction does not work equally well in the two channels and suffers from the fact that it does not go to zero as E_{meas} approaches the Bhabha calibration point. For these reasons, the logarithmic correction is the one applied to the data in the $\pi^0\pi^0$ channel discussed in this thesis and in the exclusive cascade events $\Upsilon(2S) \rightarrow \gamma\chi_b \rightarrow \gamma\gamma\Upsilon(1S) \rightarrow \gamma\gamma l^+l^-$ to be published.[5]

We note that the only physics result we present in this thesis which depends on the energy corrections is the mass distribution of the $\pi^0\pi^0$ system. The uncertainty in the energy scale introduces a systematic error on the fitted parameters determined from the fits to this spectrum. We estimate this error by comparing the results obtained by using the linear and logarithmic corrections and find that the resulting error is small compared to the statistical error.

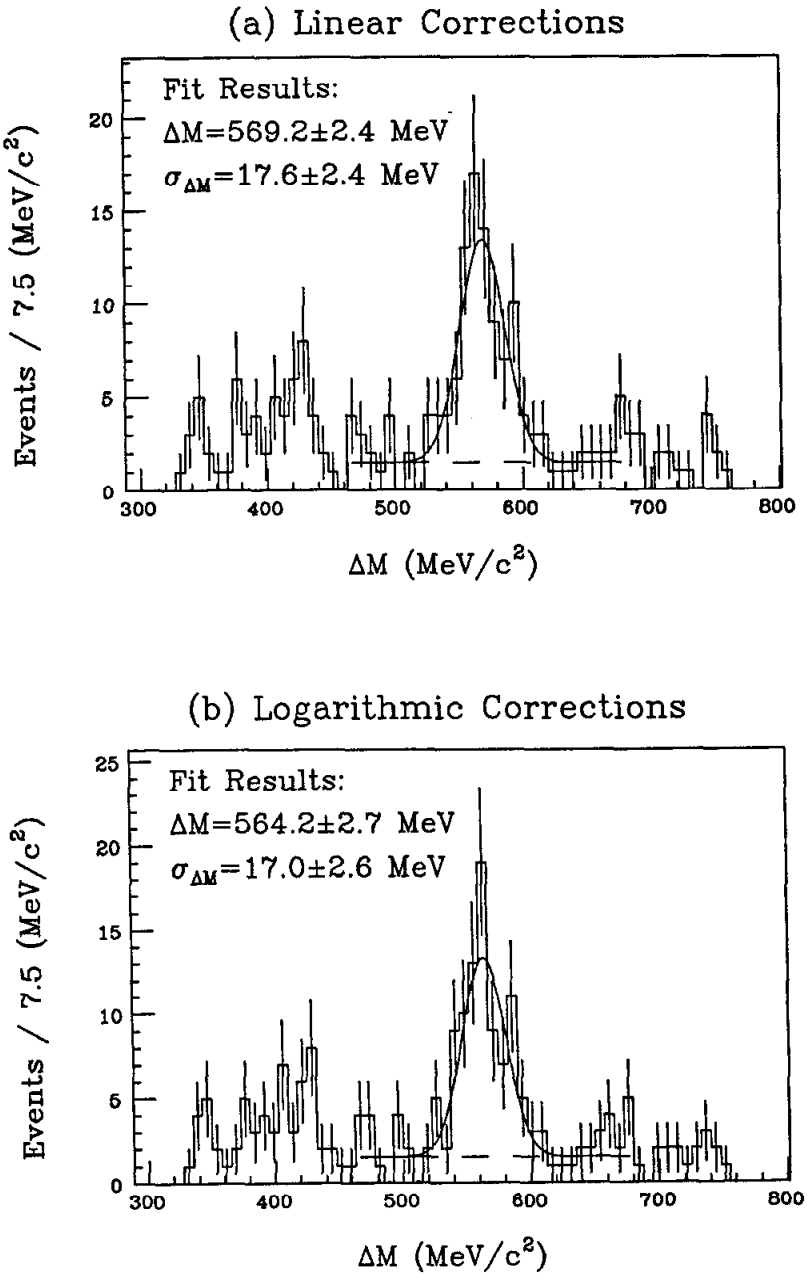

Fig. A.5 Mass difference for $\gamma\gamma l^+l^-$ events with energy corrections applied. a) linear corrections applied with $\alpha_{linear} = 0.0492$. b) logarithmic corrections applied with $\alpha_{log} = 0.0137$.

A.4 Logarithmic Corrections on $\Upsilon(2S) \rightarrow \gamma\chi_b \rightarrow \gamma\gamma\Upsilon(1S)$

As an example of the effect of these corrections on photons in the 100–140 MeV energy range, we use the cascade transitions $\Upsilon(2S) \rightarrow \gamma\chi_b \rightarrow \gamma\gamma\Upsilon(1S) \rightarrow \gamma\gamma l^+l^-$. We examine the events plotted in Figure A.3. These are all $\gamma\gamma l^+l^-$events which have passed all cuts including the kinematic fit but not a mass difference cut. The energies used are uncorrected. We select events corresponding to $\gamma\gamma$ transitions from the $\Upsilon(2S)$ to the $\Upsilon(1S)$ by selecting events with $\Delta M = 542 \pm 45$ MeV/c^2. For the selected events we plot in Figure A.6a the energy of the lower energy photon. We fit this spectrum with a flat background and two NaI(Tℓ) lineshapes[6] of width fixed at the detector resolution. The fit is shown in Figure A.6b. We find a good fit with $E_{\gamma_1} = 101.5 \pm 1.2$ MeV and $E_{\gamma_2} = 125.5 \pm 1.0$ MeV. We compare this with the energy distribution of E^{γ}_{low} corrected using the logarithmic correction with α_{log} = 0.0137. Figure A.7a is a plot of the corrected energy distribution of the low energy photon with the fit indicated in Figure A.7b. The corrected energies found are $E^{corr}_{\gamma_1} = 106.8 \pm 1.2$ MeV and $E^{corr}_{\gamma_2} = 132.2 \pm 1.1$ MeV. The correction adds about 5 MeV of energy to a photon in the 100–140 MeV energy range. Note that the energies quoted here are for comparison only and are not intended to be used for calculation of the ^3P_J energy levels.

For this example we also estimate the energy scale uncertainty on E^{γ}_{low}which remains after the correction is applied. Part of this error results from the statistical uncertainty in the determination of α_{log}. This uncertainty translates into a systematic uncertainty in the energy scale. Another part of this remaining overall scale uncertainty is due to the uncertainty in the form of the correction. For this we use the results of the linear correction. Considering these two sources of error together, we estimate the contribution to the total systematic uncertainty on E^{γ}_{low} due to the energy scale to be ± 0.5 MeV for photons in the energy range 100–140 MeV.

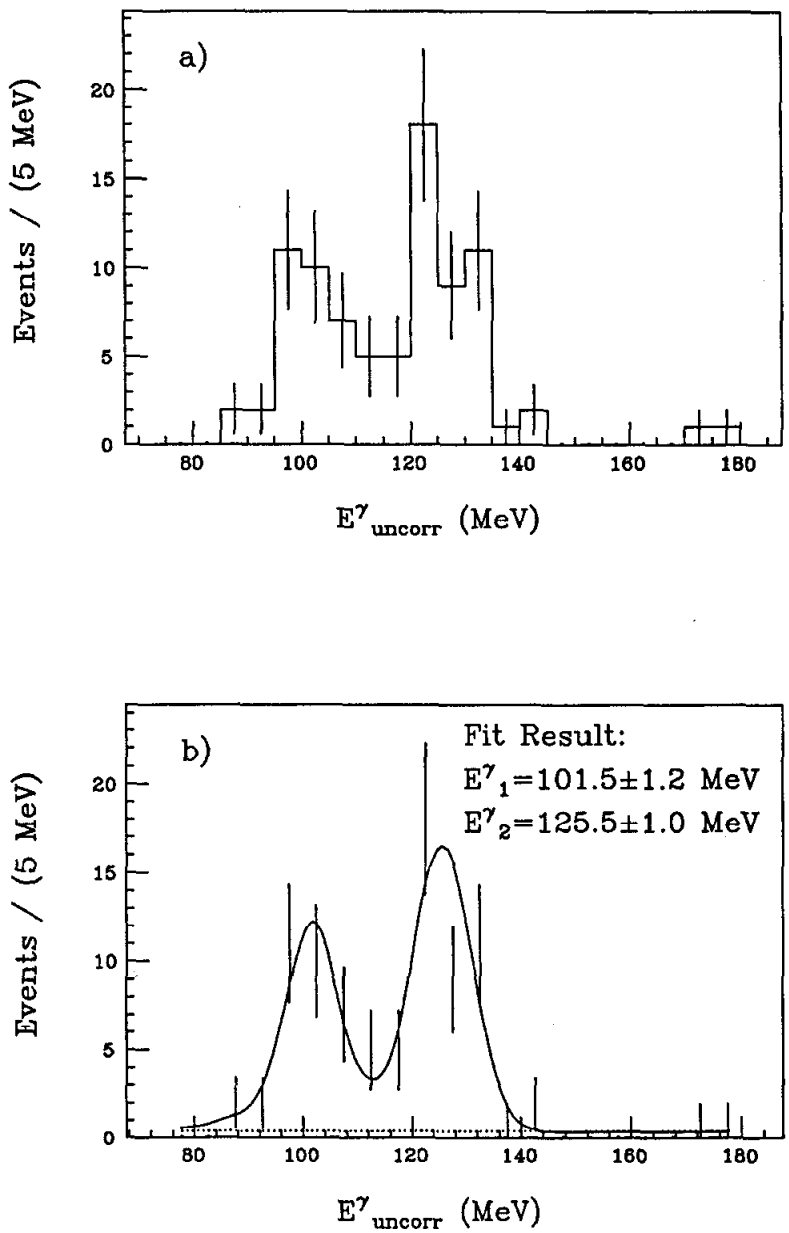

Fig. A.6 Low energy photon from $\gamma\gamma$ transitions without energy corrections applied. The curve in Figure A.6b is a fit to the data with a flat background and two NaI(Tℓ) lineshapes of fixed resolution.

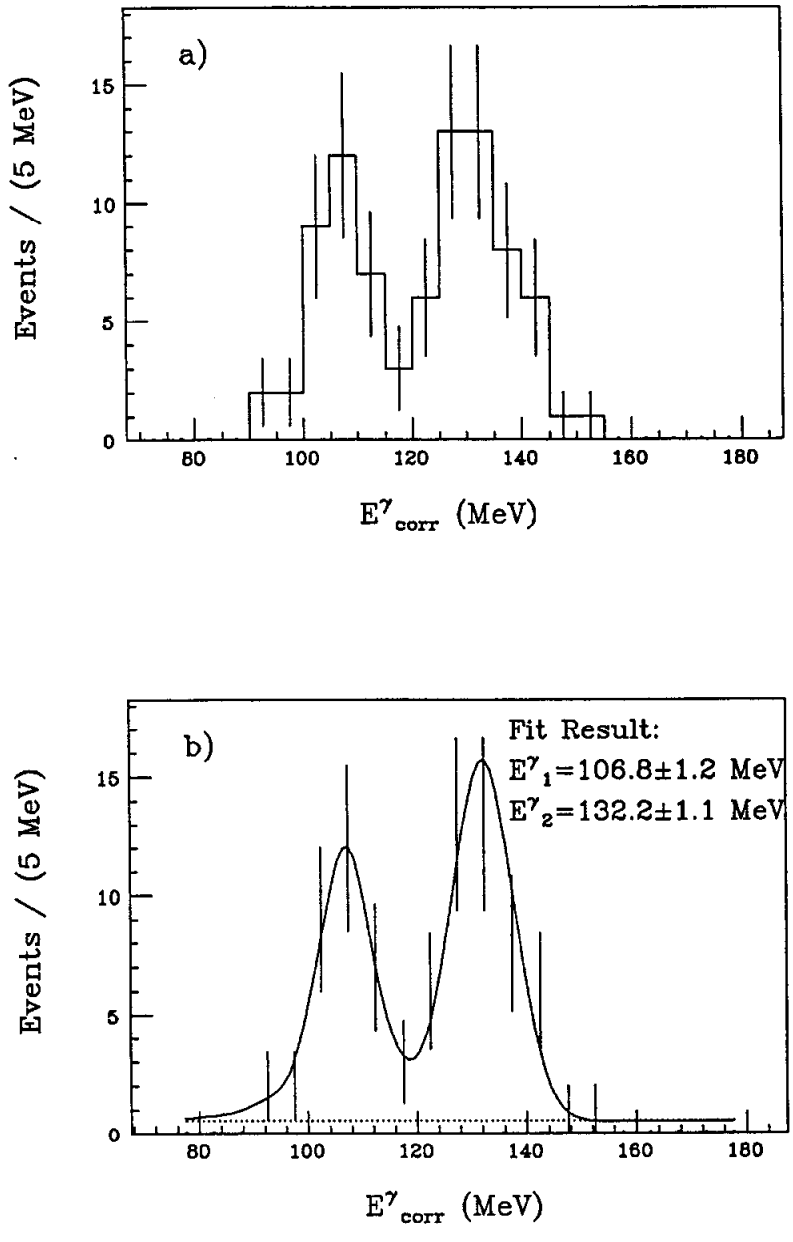

Fig. A.7 Low energy photon from $\gamma\gamma$ transitions with logarithmic energy corrections applied. The curve in Figure A.7b is a fit to the data with a flat background and two NaI(Tℓ) lineshapes of fixed resolution.

References

1) R. Nernst, Ph. D. thesis, Universität Hamburg, 1985 (unpublished).

2) Particle Data Group, *Rev. Mod. Phys.* **56** (1984) No. 2, Part II.

3) S. Lowe, private communication.

4) B. Rossi, *High Energy Particles* (Prentice–Hall, New York, 1952).

5) W. Walk *et al.*, 'Observation of Two χ_b States in Exclusive Radiative Decays of the $\Upsilon(2S)$', to be submitted for publication in *Physical Review D.*

6) R. Lee, Ph. D. thesis, Stanford University, 1985, and SLAC Report 282 (unpublished).

Appendix B

Kinematic Fitting

We use kinematic fitting to select events satisfying energy and momentum conservation. For each event we wish to fit the 4-vectors of the 6 particles. These 4-vectors are related by the four constraint equations provided by energy and momentum conservation. When the fit is performed, the mass of each particle is fixed and the polar and azimuthal angles, and the energy are varied. The fit is evaluated by forming a χ^2 goodness of fit from the fitted and measured quantities while folding the measurement errors of these quantities into the calculation. The best fit is found by minimizing this χ^2 sum. A detailed discussion of kinematic fitting procedures can be found elsewhere.[1]

We also include the event vertex as a fit parameter. The vertex is varied only along the beam axis. This is done to decouple the uncertainty of the beam position from the uncertainty of the theta measurement due to the crystal segmentation. Events in the sample are fit using z=0 as a measured quantity with the event vertex size of 1.5cm used as the measurement uncertainty of the z vertex. Although the vertex is treated as a measured quantity and this is not strictly true, this approximation yields good results.

Muon energies are treated as unmeasured. This is due to the fact that they do not deposit energy in proportion to their incident energy (as discussed in Chapter 4). The angular measurements are made based on the pattern of energy deposition

in the crystals. The errors we use for the fit are σ_{θ_μ}=35 milliradians and $\sigma_{\phi_\mu}=\frac{\sigma_{\theta_\mu}}{sin\theta_\mu}$. This is due to the fact that the azimuthal angle subtended by a crystal increases as $\theta \rightarrow 0$, i.e. as we approach the beam direction.

For photons and electrons, we measure the energy with a resolution of $\frac{\sigma_E}{E} = \frac{2.6\%}{E^{\frac{1}{4}}}$ (E in GeV). The angular resolution is determined by the shower profile. At lower energies the energy deposition is limited to a few crystals and the angular resolution is the same as that for muons. As the energy increases, the shower becomes more well defined and the resulting angular resolution is improved. For electromagnetically showering particles (e,γ) the resolution in $\sigma_{\theta_{e,\gamma}}$ is taken to be 35 milliradians below 100 MeV, 20 milliradians above 1000 MeV and assumed to vary linearly from 35 to 20 milliradians as the energy of the particle varies from 100-1000 MeV. For the resolution in ϕ we again use $\sigma_{\phi_{e,\gamma}}=\frac{\sigma_{\theta_{e,\gamma}}}{sin\theta_{e,\gamma}}$. These choices for the resolution are based on Monte Carlo studies.

As indicated above, all quantities except for the muon energies are measured in $\pi^0\pi^0\mu^+\mu^-$ events. With 4 constraint equations and two unknowns, the fit is overconstrained and is considered a 2–C fit. For electron events, we measure all quantities and are able to make a 4–C fit.

Although we do measure electron energies in the detector, lineshape and leakage effects at these high energies distort the shape of measured energies away from a pure Gaussian. The histogram in Figure B.1a is a plot of the observed electron energies in the final event candidates. These events are selected with a 2–C kinematic fit which treats the electron energies as unmeasured. The equivalent plot for Monte Carlo data is shown in Figure B.1b. The curve in each figure is the expectation from $\Upsilon(2S)\rightarrow\pi^0\pi^0\Upsilon(1S)\rightarrow\gamma\gamma\gamma\gamma e^+e^-$ events where the energies of the electrons are smeared by a pure Gaussian detector resolution. Also included is the Doppler broadening of the electron energies due to the non-zero momentum of the $\Upsilon(1S)$ in the lab frame. The distribution of $\Upsilon(1S)$ momenta used is based on the measured mass distribution of the di-pion system discussed in Chapter 4. The curves are

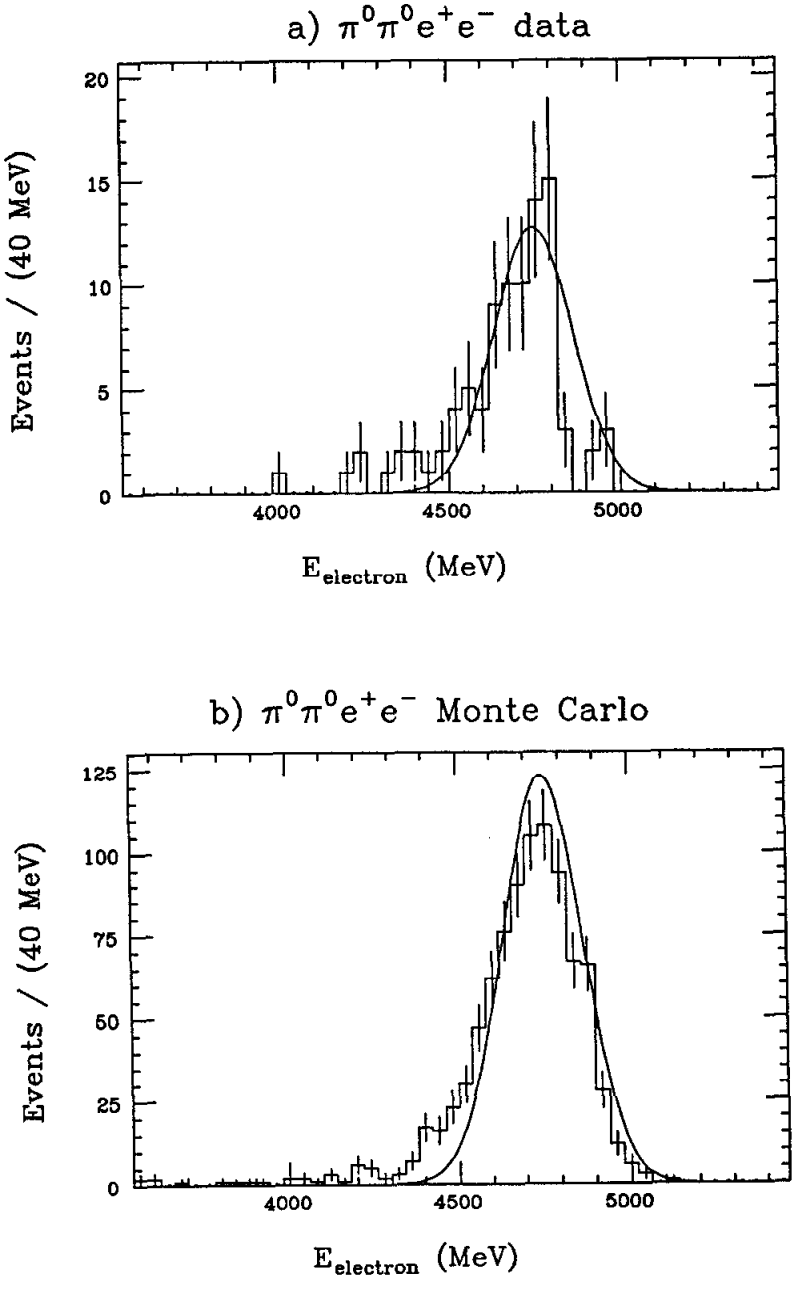

Fig. B.1 Observed electron energies observed in $\pi^0\pi^0e^+e^-$ events passing all cuts including a 2–C fit. a) data events and b) Monte Carlo events. The curves indicate the expectation from a pure Gaussian energy resolution folded with the Doppler broadening due to the velocity of the $\Upsilon(1S)$. The histograms and the curves are normalized to the same number of events.

normalized to the number of events in each histogram.

We see that in both the data and the Monte Carlo, there are a significant number of electrons with energy outside the expectation for purely Gaussian errors. A kinematic fit using the electron events as measured and a Gaussian error of $\frac{\sigma_E}{E} = \frac{2.6\%}{E^{\frac{1}{4}}}$ on the electron energies rejects about 25% of the final candidate events when we make a confidence level cut of 5%.* After applying the standard selection and the 2–C kinematic fit, the amount of background is small, and we do not gain anything by requiring a good 4–C fit. For the selection procedure we therefore require only a 2–C fit for $\pi^0\pi^0e^+e^-$ candidates with a fit confidence level greater than 5%.

We plot in Figure B.2 the confidence level distribution for the $\pi^0\pi^0e^+e^-$ events passing the kinematic fit. Figure B.2a is the data and Figure B.2b is the Monte Carlo. Figures B.3a,b are the corresponding plots for the muon channel. The differences between the data and Monte Carlo give rise to a systematic error from the fitting procedure. This error is estimated by averaging changes in the ratio of data events to Monte Carlo events as the fit confidence level cut is varied from 1% to 10%. This systematic error is included in the study of systematic errors on the efficiency listed in Chapter 4.

---

* We note that low energy photons suffer also from non-Gaussian tails, but because the absolute deviations of the energies of the photons are small compared to that of the electrons, the tails on the photon energies do not affect the fit appreciably.

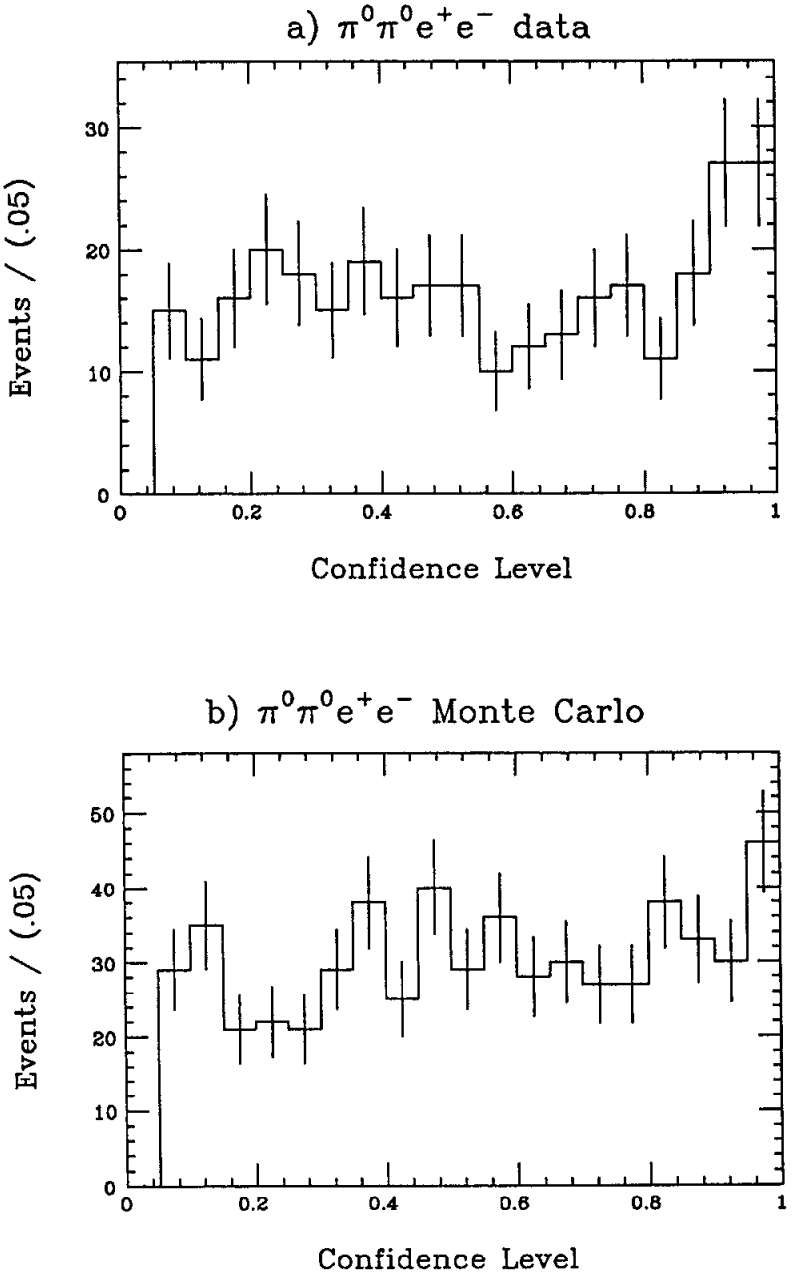

Fig. B.2 Confidence level distributions for $\pi^0\pi^0e^+e^-$ events passing the kinematic fit. a) data events and b) Monte Carlo events.

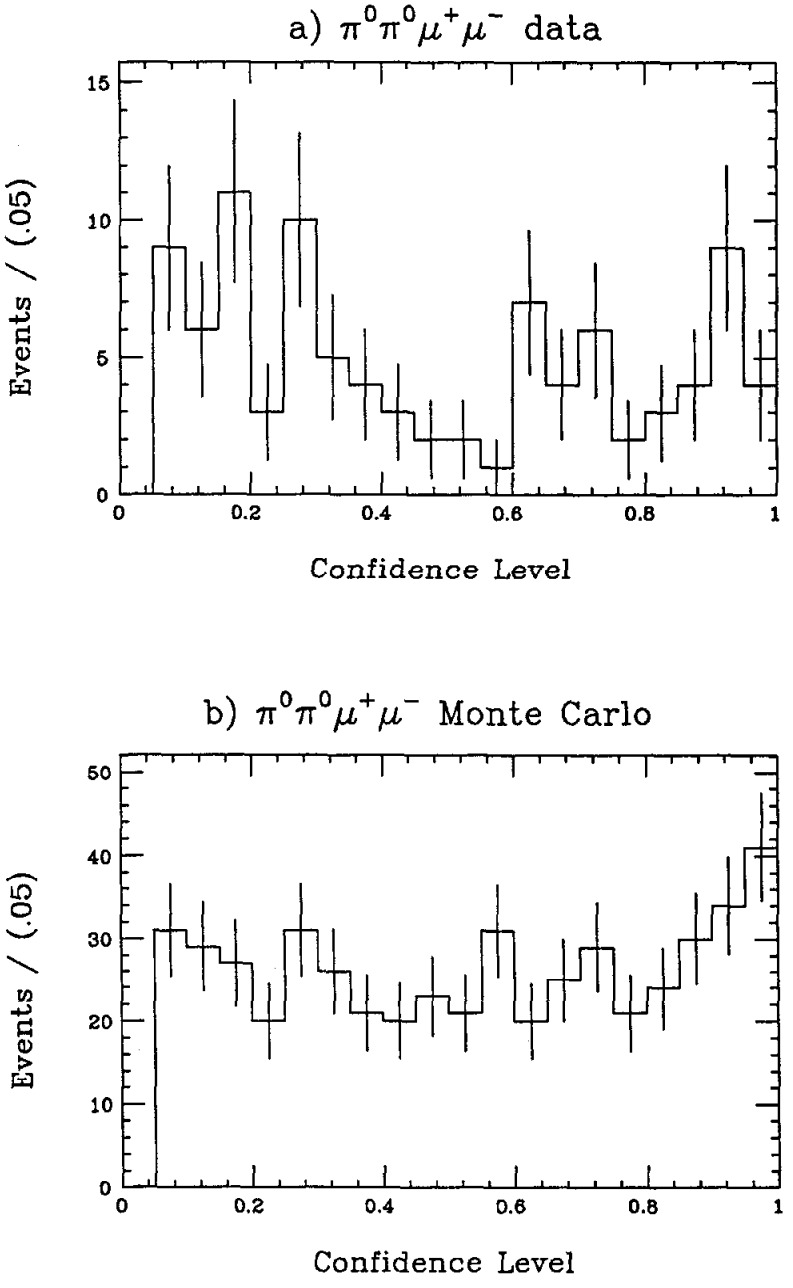

Fig. B.3 Confidence level distributions for $\pi^0\pi^0\mu^+\mu^-$ events passing the kinematic fit. a) data events and b) Monte Carlo events.

References

1) A. G. Frodesen, O. Skjeggestad, and H. Tøfte, *Probability and Statistics in Particle Physics* (Universitetsforlaget, Bergen, Norway, 1979)

Appendix C

Reference Frames and Spin Dependence

We examine here the properties of the angular distribution of the pions in the decay $\Upsilon(2S) \rightarrow \pi\pi\Upsilon(1S)$. Previous measurements of both $\psi' \rightarrow \pi^+\pi^-\psi$[1] and $\Upsilon(2S) \rightarrow \pi\pi\Upsilon(1S)$[2,3] have indicated that the $\pi\pi$ system and the ψ (and $\Upsilon(1S)$) are emitted in a relative S–wave. Because of this observation, a partial wave analysis in orbital and spin angular momentum has been carried out by Cahn[4] for $\psi' \rightarrow \pi\pi\psi$ which is equally valid for $\Upsilon(2S) \rightarrow \pi\pi\Upsilon(1S)$. In the Cahn analysis, the directions of the pions in the $\pi\pi$ center of mass are measured relative to a z–axis coinciding with the beam axis. This reference frame is shown in Figure 4.15 and will be referred to as frame $S^{\|}$. Previous measurements of $\Upsilon(2S) \rightarrow \pi^+\pi^-\Upsilon(1S)$ have been presented with the pion directions measured in a coordinate system in the $\pi^+\pi^-$ center of mass where the z–axis is anti-parallel to the $\Upsilon(1S)$ momentum vector.[2,3] This is the helicity frame and will be referred to as S^{hel}. We will show that for the case where the $\pi\pi$ system is emitted isotropically, the $\cos\theta_\pi$ distribution in S^{hel} is flat, regardless of the spin of the $\pi\pi$ system.* Note that the angular distribution of the pions calculated by Cahn in the $S^{\|}$ frame has been found to depend on the spin of the $\pi\pi$ system, even for an S–wave decay of the $\Upsilon(2S)$.

We write $I(\theta_\pi^{\|}, \phi_\pi^{\|}, \theta_{\pi\pi}, \phi_{\pi\pi})$ as the full angular distribution describing the de-

* We cannot draw any conclusions about the distribution of ϕ_π in S^{hel} within the formalism presented here.

cay $\Upsilon(2S)\to X\Upsilon(1S)\to\pi\pi\Upsilon(1S)$ in the $S^{\|}$ frame. For the case where the X and the $\Upsilon(1S)$ are produced in a relative S–wave, by definition there is no angular dependence on $\theta_{\pi\pi}$ or $\phi_{\pi\pi}$. The distribution of $\theta_\pi^{\|}$ and $\phi_\pi^{\|}$ depends on the spin of X, as shown by Cahn. We express this angular distribution as a sum of spherical harmonics:

$$I(\theta_\pi^{\|},\phi_\pi^{\|},\theta_{\pi\pi},\phi_{\pi\pi}) \equiv I(\theta_\pi^{\|},\phi_\pi^{\|}) = \sum_{L,M} a_{L,M} Y_L^M(\theta_\pi^{\|},\phi_\pi^{\|})$$

This is always possible since the spherical harmonics are a complete set of functions.

To calculate the corresponding angular distribution in the helicity frame, we rotate the origin of coordinates so that the new z–axis is anti-parallel to the flight direction of the $\Upsilon(1S)$. This direction is the same as the $\pi\pi$ momentum vector in the laboratory frame which we denote by $(\theta_{\pi\pi},\phi_{\pi\pi})$. We represent this rotation as:

$$S^{hel} = \mathcal{R}(\phi_{\pi\pi},\theta_{\pi\pi},-\phi_{\pi\pi})S^{\|}$$

which is a rotation about the normal to the original z–axis and the $\pi\pi$ direction. We now apply this rotation:

$$\begin{aligned} I'(\theta_\pi^{hel},\phi_\pi^{hel},\theta_{\pi\pi},\phi_{\pi\pi}) &= \mathcal{R}(\phi_{\pi\pi},\theta_{\pi\pi},-\phi_{\pi\pi})I(\theta_\pi^{\|},\phi_\pi^{\|}) \\ &= \sum_{L,M} a_{L,M}\mathcal{R}(\phi_{\pi\pi},\theta_{\pi\pi},-\phi_{\pi\pi})Y_L^M(\theta_\pi^{\|},\phi_\pi^{\|}) \qquad [C.1] \end{aligned}$$

Rotations of the spherical harmonics may be expressed in terms of the D functions:[5]

$$\mathcal{R}(\phi_{\pi\pi},\theta_{\pi\pi},-\phi_{\pi\pi})Y_L^M(\theta_\pi^{\|},\phi_\pi^{\|}) = \sum_{M'} D^L_{M',M}(\phi_{\pi\pi},\theta_{\pi\pi},-\phi_{\pi\pi})Y_L^{M'}(\theta_\pi^{hel},\phi_\pi^{hel}) \quad [C.2]$$

Substituting [C.2] into [C.1] we have:

$$I'(\theta_\pi^{hel},\phi_\pi^{hel},\theta_{\pi\pi},\phi_{\pi\pi}) = \sum_{L,M} a_{L,M}\Big\{\sum_{M'} D^L_{M',M}(\phi_{\pi\pi},\theta_{\pi\pi},-\phi_{\pi\pi})Y_L^{M'}(\theta_\pi^{hel},\phi_\pi^{hel})\Big\} \qquad [C.3]$$

To calculate the angular distributions as a function of θ_π^{hel} and ϕ_π^{hel} only, we integrate over $\theta_{\pi\pi}$ and $\phi_{\pi\pi}$. Because we have S–wave decay, the only contribution to the integral over $d\Omega_{\pi\pi}$ is the D function itself.

$$I'(\theta_\pi^{hel},\phi_\pi^{hel}) = \sum_{L,M,M'} a_{L,M} Y_L^{M'}(\theta_\pi^{hel},\phi_\pi^{hel}) \int D^L_{M',M}(\phi_{\pi\pi},\theta_{\pi\pi},-\phi_{\pi\pi}) d\Omega_{\pi\pi}$$

note that:

$$\begin{aligned} D^L_{M',M}(\phi_{\pi\pi},\theta_{\pi\pi},-\phi_{\pi\pi}) &= e^{-iM'\phi_{\pi\pi}}\ d^L_{M',M}(\theta_{\pi\pi})\ e^{iM\phi_{\pi\pi}} \\ &= e^{-i(M'-M)\phi_{\pi\pi}}\ d^L_{M',M}(\theta_{\pi\pi}) \end{aligned}$$

Because of the oscillating exponentials of the D functions, only terms with $M' = M$ are non-vanishing after the integration over $\phi_{\pi\pi}$. Therefore:

$$I'(\theta_\pi^{hel},\phi_\pi^{hel}) = 2\pi \sum_{L,M} a_{L,M} Y_L^M(\theta_\pi^{hel},\phi_\pi^{hel}) \int d^L_{M,M}(\theta_{\pi\pi}) d(cos\theta_{\pi\pi})$$

To calculate $I'(\theta_\pi^{hel})$ we integrate over ϕ_π^{hel}. We may rewrite the spherical harmonics since $Y_L^M\ (\theta_\pi^{hel},\phi_\pi^{hel}) = P_L^M(\theta_\pi^{hel}) e^{iM\phi_\pi^{hel}}$ where $P_L^M(\theta_\pi^{hel})$ are the associated Legendre functions. Only terms with M=0 will have a non-vanishing integral. After the ϕ_π^{hel} integration we have:

$$I'(\theta_\pi^{hel}) = (2\pi)^2 \sum_L a_{L,0} Y_L^0(\theta_\pi^{hel}) \int d^L_{0,0}(\theta_{\pi\pi}) d(cos\theta_{\pi\pi})$$

Note that:

$$d^L_{0,0}(\theta_{\pi\pi}) = \sqrt{\frac{4\pi}{2L+1}} Y_L^0(\theta_{\pi\pi})$$

and since $Y_0^0 \equiv$ constant:

$$\begin{aligned} \int d^L_{0,0}(\theta_{\pi\pi}) d(cos\theta_{\pi\pi}) &\propto \int Y_L^0(\theta_{\pi\pi}) d(cos\theta_{\pi\pi}) \\ &\propto \int Y_L^0(\theta_{\pi\pi}) Y_0^0(\theta_{\pi\pi}) d(cos\theta_{\pi\pi}) \\ &\propto \delta_{L,0} \end{aligned}$$

by the orthogonality of the spherical harmonics. The sum over L reduces to one term and we find:

$$I'(\theta_\pi^{hel}) \propto a_{0,0} Y_0^0(\theta_\pi^{hel}) \equiv \text{constant}$$

We find that for the decay of the $\Upsilon(2S)$ where the $\pi\pi$ system and the $\Upsilon(1S)$ are emitted isotropically, the angular distribution in $\cos\theta_\pi^{hel}$ is flat, regardless of the spin of the $\pi\pi$ system.

References

1) G. Abrams, Properties of the New Particles $\psi(3095)$ and $\psi'(3684)$, Proc. of the 1975 Int. Symp. on Lepton and Photon Interaction at High Energies, Ed. W.T. Kirk, (Stanford University, Stanford, 1975).

2) D. Besson *et al.*, *Phys. Rev.* **D30** (1984) 1433.

3) V. Fonseca *et al.*, *Nucl. Phys.* **B242** (1984) 31.

4) R. Cahn, *Phys. Rev.* **D12** (1975) 3559.

5) M. Rose, *Elementary Theory of Angular Momentum* (Wiley, New York, 1957).